LA-8030-T
Thesis

A LAMPF Neutrino Experiment to Test Muon Number Conservation

University of California
LOS ALAMOS SCIENTIFIC LABORATORY
Post Office Box 1663 Los Alamos, New Mexico 87545

LA-9030-T
Thesis
UC-34a
Issued: September 1979

A LAMPF Neutrino Experiment to Test Muon Number Conservation

Suzanne Eileen Willis*

*Physics Department, Fermi National Accelerator Laboratory, Box 500, Batavia, IL 60510.

TABLE OF CONTENTS

LIST OF TABLES

LIST OF FIGURES

ABSTRACT

A LAMPF NEUTRINO EXPERIMENT TO TEST MUON NUMBER CONSERVATION

Suzanne Eileen Willis

Yale University 1979

The need for a muon number conservation law separate from lepton number conservation is mandated by the absence of neutrinoless muon-electron transitions. The form of the muon number conservation law, however, is not determined by these considerations. A search has been made for electron antineutrinos coming from positive muon decays, which would be allowed by a multiplicative formulation of muon number conservation, but not by an additive formulation.

The LAMPF beam dump was used as a source of positive muons decaying at rest; electron antineutrinos were detected via inverse beta decay in a six-ton water Cerenkov counter. No excess of events above known backgrounds was seen; a limit was placed on the branching ratio for positive muon decay to electron antineutrinos of $R < 6.5\%$.

Electron neutrinos from normal muon decay were detected during a fill of the counter with heavy water, via the inverse beta decay on the deuteron. The cross section for this reaction was measured, averaged over the neutrino energy spectrum; the measured value of $(0.52 \pm 0.18) \times 10^{-40}$ cm^2 is in good agreement with the calculated value of 0.48×10^{-40} cm^2.

INTRODUCTION

The need for a muon number conservation law separate from lepton number conservation has been recognized for many years. The need for this law is mandated by the absence of muon-electron transitions without neutrinos, such as

$$\mu^+ \to e^+\gamma$$
$$\mu^+ \to e^+e^+e^-$$
$$\mu^-Z \to e^-Z \quad ,$$

and also by the observation of the distinct identity of the neutrino from pion decay

$$\pi^+ \to \mu^+\nu_\mu$$

and that from beta decay

$$n \to pe^-\bar{\nu}_e$$

such that

$$\nu_\mu Z \not\to e^-Z' \text{ (Ref. 1)} \quad ,$$

1. Danby et al., Phys. Rev. Lett. 9, 36 (1962).

The exact form of the muon number conservation law is not determined by the above considerations; it was pointed out by Feinberg and Weinberg[2] that muon number could be conserved either additively or multiplicatively. Defining

$$L_\mu = +1 \text{ for } \mu^-, \nu_\mu$$
$$= -1 \text{ for } \mu^+, \bar{\nu}_\mu$$
$$= 0 \text{ for all others} ,$$

the additive formulation requires that $\Sigma(L_\mu)$ = constant, while the multiplicative formulation requires $\Pi(-1)^{L_\mu}$ = constant. Both formulations forbid direct μ-e transitions as detailed above, but they are not identical. The additive law is more restrictive concerning reactions which involve at least two electrons and two muons. Examples of reactions which are allowed by the multiplicative formulation but not by the additive one include

$$\mu^+ e^- \rightarrow \mu^- e^+$$
$$e^- e^- \rightarrow \mu^- \mu^-$$
$$\mu^+ \rightarrow e^+ \bar{\nu}_e \nu_\mu .$$

The third reaction is muon decay with inverted neutrinos; the normal decay, allowed by both formulations, is

$$\mu^+ \rightarrow e^+ \nu_e \bar{\nu}_\mu .$$

---

2. G. Feinberg and S. Weinberg, Phys. Rev. Lett. 6, 381 (1961).

Present limits on the first two reactions are considerably larger than the rate expected from weak interactions.[3] Previous limits on the muon decay to inverted neutrinos come from the Gargamelle collaboration at CERN; defining the branching ratio

$$R \equiv \frac{\mu^+ \to e^+\bar{\nu}_e\nu_\mu}{\mu^+ \to \text{all}} ,$$

the Gargamelle collaboration found $R < 0.25$ (90% C.L.) in 1973,[4] using 52 events. More detailed analysis, also by the Gargamelle collaboration, of a larger sample of 260 events yielded $R = 0.13 \pm 0.15$ in 1978.[5]

The above formulation of multiplicative muon number conservation does not constitute a complete theory; in particular, there is no indication of what to expect for a branching ratio. However, a finite result for R would be evidence of a multiplicative law.

We have performed an experiment at the Los Alamos Meson Physics Facility (LAMPF) to search for both ν_e and $\bar{\nu}_e$ from μ^+ decay via the inverse beta decay reactions

$$\nu_e d \to ppe^-$$

$$\bar{\nu}_e p \to ne^+$$

3. R. Amato et al., Phys. Rev. Lett. 21, 1709 (1968); W.C. Barber et al., Phys. Rev. Lett. 22, 902 (1969).

4. Eichten et al., Phys. Lett. 46B, 281 (1973).

5. Blietschau et al., Nucl. Phys. B133, 205 (1978).

in a six-ton water Cerenkov counter which was filled with either H_2O or D_2O.

Our source of μ^+ was the beam dump for the primary proton beam. LAMPF is an 800-MeV linear accelerator which accelerates both protons and H^- ions. Design intensity for the proton beam is 1 mA at a 6% duty factor. The beam dump was water-cooled copper; protons stopping in it produced both π^+ and π^-. The π^- were captured on nuclei; the π^+ were stopped in the copper and decayed:

$$\pi^+ \rightarrow \mu^+ \nu_\mu \ .$$

The μ^+ also stopped and decayed; this was our source of muons. The μ^- contamination (from π^- decay) has been estimated to be 1/7000;[6] it will therefore not contribute at our expected level of sensitivity, a few percent. Our detector was situated at 90° to the beam direction, behind 6.3 m of steel shielding. The neutrinos emerged isotropically from the beam dump, but high-energy neutrons tended to go forward; we chose 90° to minimize neutron backgrounds. We measured beam-associated backgrounds with smaller amounts of shielding between our detector and the beam dump; the final amount of 6.3 m was chosen as being sufficient to attenuate beam-associated background events so they were small compared to our expected level of sensitivity. The detector was surrounded on all sides by at least 1 m of shielding to reduce backscattered neutrons and cosmic-ray events.

---

6. LAMPF Neutrino Facility Proposal, Los Alamos Scientific Laboratory report LA-4842-MS (1971).

The detector was surrounded by a 4π cosmic-ray anticoincidence shield, consisting of an inner layer of scintillators, a layer of lead, and an outer layer of active counters (scintillators on top, drift chambers on the sides). This anticoincidence shield reduced the cosmic-ray backgrounds in the counter in (20,60) MeV by a factor of 10^3.

The remaining cosmic-ray events could be measured accurately on line and subtracted directly, because of the time structure of the beam. The LAMPF duty factor was 6%, with a 500-μs beam spill and a repetition rate of 120 Hz. The beam spill was long compared to the muon lifetime, so we required events to occur during the spill. This had the immediate effect of reducing the cosmic-ray background to 6% of the total rate, and enabled us to open a gate between spills which was long compared to the length of the spill, so we could accurately measure the cosmic-ray contribution and subtract it. The cosmic-ray events then did not contribute to the subtracted spectrum except in the uncertainty of the subtraction. The level of sensitivity achieved by the experiment then depended on the amount of running time, to reduce the error on the subtraction, and on the intensity of the beam, to increase the signal to noise ratio.

CHAPTER I

THEORY

A. NORMAL LEPTON INTERACTIONS

1. Beta Decay

The Fermi theory of beta decay is the basis for several aspects of this experiment. Neutrinos are detected via the inverse beta decay process on protons, and muon decay is closely related to beta decay. These processes, inverse beta decay and muon decay, will be discussed specifically below. The discussion will begin with the simple theory of beta decay, to lay the groundwork for what follows. This discussion follows Wu and Moskowski.[7]

We assume that the beta decay from an arbitrary nucleus can be represented by[8]

$$Z^A \rightarrow (Z + 1)^A + e^- + \bar{\nu}_e$$

or, in the case of positron decay,

$$Z^A \rightarrow (Z - 1)^A + e^+ + \nu_e \quad .$$

We will assume that the interaction is a point interaction, that is, that all four particles interact at a point, with no intermediaries.

7. Wu and Moskowski, Beta Decay, John Wiley and Sons, 1966.

8. Ibid., pp. 21-24.

This corresponds to an infinite intermediate vector boson mass. This leads to a Hamiltonian of the form

$$H_\beta = g \sum_n \left[\psi_e^*(\vec{r}_n)\psi_{\bar{\nu}_e}^*(\vec{r}_n)Q_n^+ + \psi_e(\vec{r}_n)\psi_{\bar{\nu}_e}(\vec{r}_n)Q_n^-\right] \quad ,$$

where the sum is over all particles in the nucleus. The constant g gives the strength of the interaction. The wave functions $\psi_e^*(\vec{r}_n)$ and $\psi_{\bar{\nu}_e}^*(\vec{r}_n)$ are the created electron and neutrino at the position of the n^{th} nucleon, coupled to the operator Q_n^+ which changes a neutron into a proton but otherwise leaves its wave function unchanged. Then we have the wave functions $\psi_e(\vec{r}_n)$, $\psi_{\bar{\nu}_e}(\vec{r}_n)$ for the annihilated leptons, coupled to Q_n^- which changes a proton to a neutron. The neutrino wave function is just a plane wave; the electron wave function is not, to the extent that it interacts with the Coulomb field of the nucleus and surrounding electrons.

The effects of spin will now be added to this formulation.[9] Results will be discussed in terms of the Hamiltonian density, $\underset{\sim}{H} = \psi_p^\dagger H_\beta \psi_n$, rather than the Hamiltonian itself. The wave functions of each particle will now be two-component spinors. There are four bilinear combinations of the electron and neutrino wave functions:

$$\psi_e^\dagger\psi_\nu, \ \psi_e^\dagger\sigma_x\psi_\nu, \ \psi_e^\dagger\sigma_y\psi_\nu, \ \psi_e^\dagger\sigma_z\psi_\nu \quad ,$$

where $\sigma_{x,y,z}$ are the Pauli spin matrices:

$$\sigma_x = \begin{pmatrix} 0 & 1 \\ 1 & 0 \end{pmatrix} ; \quad \sigma_y = \begin{pmatrix} 0 & -i \\ i & 0 \end{pmatrix} ; \quad \sigma_z = \begin{pmatrix} 1 & 0 \\ 0 & -1 \end{pmatrix} .$$

9. Ibid., pp. 43-51.

The first combination is a scalar, and the other three form an axial vector. The only way to combine these terms to yield a scalar is in the combinations $S \cdot S$ or $A \cdot A$; keeping only terms which are invariant under rotation gives two allowed forms of the interaction:

$$\left(\psi_p^\dagger Q^+ \psi_n \right)\left(\psi_e^\dagger \psi_\nu \right) \quad \text{and} \quad \sum_\mu \left(\psi_p^\dagger Q^+ \sigma_\mu \psi_n \right)\left(\psi_e^\dagger \sigma_\mu \psi_\nu \right) .$$

In the relativistic formulation, the particles obey the Dirac equation:

$$\left(\gamma_\mu p^\mu - m\right)\psi = 0 ,$$

where $\hbar = c = 1$, and γ_μ are the Dirac matrices. A standard representation is

$$\gamma_o = \gamma^o = \begin{pmatrix} I & 0 \\ 0 & -I \end{pmatrix}; \; \gamma^i = \begin{pmatrix} 0 & \sigma_i \\ -\sigma_i & 0 \end{pmatrix} ,$$

and their wave functions are now four-component spinors. Once again invoking rotational invariance, and adding invariance under proper Lorentz transformations and space inversion (parity violation will be discussed shortly) yields five types of interaction, the scalar, tensor, pseudoscalar, vector, and axial vector forms, each with its own coupling constant. These forms are named for the way in which the nucleon part of the equation transforms. Assuming a nonrelativistic treatment of the nucleons yields:

$$\underset{\sim}{H}_S = g_S(\psi_p^\dagger Q^+ \beta \psi_n)(\psi_e^\dagger \beta \psi_\nu)$$

$$\underset{\sim}{H}_T = g_T \sum_\mu (\psi_p^\dagger Q^+ \sigma_\mu \psi_n)(\psi_e^\dagger \beta \sigma_\mu \psi_\nu)$$

$$\underset{\sim}{H}_P = 0 \quad .$$

(This term is zero because it contains a term of the form $\psi_p^\dagger \gamma_5 \psi_n$, which vanishes in the limit of low nucleon velocities.)

$$\underset{\sim}{H}_V = g_V(\psi_p^\dagger Q^+ \psi_n)(\psi_e^\dagger \psi_\nu)$$

$$\underset{\sim}{H}_A = g_A \sum_\mu (\psi_p^\dagger Q^+ \sigma_\mu \psi_n)(\psi_e^\dagger \sigma_\mu \psi_\nu) \quad ,$$

where $\beta = \begin{pmatrix} I & 0 \\ 0 & -I \end{pmatrix}$.

In order to take the parity nonconserving terms into account, it is necessary to introduce a pseudoscalar interaction into the Hamiltonian density, as well as the original scalar interaction:[10]

$$\underset{\sim}{H} = g \Big[\sum_i C_i (\tilde{\psi}_p \hat{O}_i Q^+ \psi_n)(\tilde{\psi}_e \hat{O}_i \psi_\nu)$$

$$+ \sum_i C_i' \, (\psi_p \hat{O}_i Q^+ \psi_n) \, (\psi_e \hat{O}_i \gamma_5 \psi_\nu)$$

$$+ \text{h.c.} \Big] \quad ,$$

where $i = S,T,P,V,A$, $g_i = gC_i$, $\hat{O}_i$ are the particular operators given above, and h.c. means hermitian conjugate. The famous experiment of Wu

10. Ibid., pp. 131-132.

et al.[11] found $C_i = C_i'$ (for the axial vector part of the interaction). This leads directly to the two-component theory of the neutrino,[12] assuming the neutrino is massless; since the neutrinos are completely polarized and exhibit only one helicity state, only two components of the spinor are needed to describe them, rather than four.

2. Muon Decay

We will now consider muon decay, $\mu^+ \rightarrow e^+ \nu_e \bar{\nu}_\mu$.[13] The Hamiltonian density for this decay is analogous to the one for beta decay:

$$g_i(\tilde{\psi}_e \hat{O}_i \psi_\mu)(\tilde{\psi}_{\nu_\mu} \hat{O}_i \psi_{\nu_e}) \quad .$$

If we now use the two-component wave functions for the neutrinos, we have for the neutrino part:

$$\frac{1}{4} g_i \left[\tilde{\psi}_{\nu_\mu}(1 \mp \gamma_5)\hat{O}_i(1 \pm \gamma_5)\psi_{\nu_e}\right] \quad .$$

For the S, T, and P interactions, $\hat{O}_i$ is a sum of terms containing an even number of gamma matrices. Therefore, $\hat{O}_i$ and γ_5 commute and the terms vanish. For the V and A interactions, $\hat{O}_i$ is a sum of terms containing an odd number of gamma matrices, and will anticommute with γ_5; this term therefore becomes

$$\frac{1}{2} g_i \left[\tilde{\psi}_{\nu_\mu} \hat{O}_i(1 \pm \gamma_5)\psi_{\nu_e}\right] \quad .$$

---

11. C. S. Wu, E. Ambler, R. W. Hayward, D. D. Hoppes, and R. F. Hudson, Phys. Rev. 105, 1413 (1957).

12. Wu and Moskowski, op. cit, pp. 138-141.
13. Ibid., pp. 212-213.

The muon decay must therefore be a combination only of V and A interactions. Experiments indicate[14] that the form is V-A.

We will now consider the derivation of the V-A form from chirality invariance.[15] Chirality is defined as the transformation $\psi \rightarrow \gamma_5\psi$. For the neutrino, which is massless, the wave functions are eigenfunctions of chirality (we speak here of the four solutions to the Lirac equation for a particle of a given momentum), two positive, $\gamma_5\psi = \psi$, and two negative, $\gamma_5\psi = -\psi$. For massive particles, the wave functions are not eigenstates of chirality, but can be expanded in terms of these eigenstates. We then make the assumption that the four-fermion interaction should be invariant under chirality transformations on any of the wave functions. In order for this to be true, using the form of the interaction

$$\frac{1}{\sqrt{2}} g_i(\tilde{\psi}_2\hat{O}_i\psi_1)(\tilde{\psi}_4\hat{O}_i\psi_3) \quad ,$$

it is necessary for $\hat{O}_i$ and γ_5 to anticommute. As shown above, the only interactions for which this is true are V and A:

$$\hat{O} = a\gamma_\mu + b\gamma_\mu\gamma_5 \quad .$$

Now, from the condition

$$\hat{O}\gamma_5 = \hat{O}, \ \hat{O} = a\gamma_\mu\gamma_5 + b\gamma_\mu = a\gamma_\mu + b\gamma_\mu\gamma_5 \quad ,$$

14. Ibid., pp. 250-252.

15. Ibid., p. 224.

it follows that a = b;

$$\hat{O} = a\gamma_\mu(1 + \gamma_5) \quad .$$

The interaction then becomes

$$\frac{1}{\sqrt{2}} g \left[\tilde{\psi}_2\gamma_\mu(1 + \gamma_5)\psi_1\right] \left[\tilde{\psi}_4\gamma_\mu(1 + \gamma_5)\psi_3\right] \quad .$$

Writing this explicitly for μ^- decay, and indicating the sum over gamma indices, we have

$$\underset{\sim}{H} = \frac{1}{\sqrt{2}} g\Sigma_\mu \tilde{\psi}_{\nu_\mu}\gamma_\mu(1 + \gamma_5)\psi_\mu\tilde{\psi}_e\gamma_\mu(1 + \gamma_5)\psi_{\nu_e} \quad .$$

We can now calculate the electron energy spectrum,[16] which will be the same as the positron spectrum from μ^+ decay. This will also be the same as the antineutrino spectrum from μ^+ decay because the helicity of the antineutrino (whether it is $\bar{\nu}_e$ or $\bar{\nu}_\mu$) is the same as the helicity of the positron. We have

$$(1 + \gamma_5)\psi_{\nu_e} = 2\psi_{\nu_e}, \quad \tilde{\psi}_{\nu_\mu}\gamma_\mu(1 + \gamma_5) = 2\tilde{\psi}_{\nu_\mu}\gamma_\mu \quad .$$

Then

$$\underset{\sim}{H} = \sqrt{8}g \sum_\mu \tilde{\psi}_{\nu_\mu}\gamma_\mu\psi_\mu\tilde{\psi}_e\gamma_\mu\psi_{\nu_e} \quad .$$

16. Ibid., pp. 362-367.

Using the two-particle wave functions written in two-component form,

$$\psi_\mu = \begin{pmatrix} \chi_\mu \\ 0 \end{pmatrix} \qquad \psi_e = \frac{1}{\sqrt{2}} \begin{pmatrix} \chi_e \\ -\chi_e \end{pmatrix}$$

$$\psi_{\nu_\mu}^{E>0} = \frac{1}{\sqrt{2}} \begin{pmatrix} \chi_{\nu_\mu} \\ -\chi_{\nu_\mu} \end{pmatrix} \qquad \psi_{\nu_e}^{E<0} = \frac{1}{\sqrt{2}} \begin{pmatrix} -\chi_{\nu_e} \\ \chi_{\nu_e} \end{pmatrix}$$

where

$$\chi_{\nu_\mu} = \begin{pmatrix} \cos^1/2\theta_{\nu_\mu} \\ \sin^1/2\theta_{\nu_\mu}\, e^{i\phi_{\nu_\mu}} \end{pmatrix} \qquad \chi_\mu = \begin{pmatrix} \cos^1/2\theta_\mu \\ \sin^1/2\theta_\mu \end{pmatrix}$$

$$\chi_e = \begin{pmatrix} 0 \\ 1 \end{pmatrix} \qquad \chi_{\nu_e} = \begin{pmatrix} \cos^1/2\theta_{\nu_e} \\ \sin^1/2\theta_{\nu_e}\, e^{i\phi_{\nu_e}} \end{pmatrix} ,$$

where the electron moves along the Z axis and the muon spin direction is in the X-Z plane, we have for the matrix element

$$H_{fi} = -4g\left(\cos \tfrac{1}{2}\theta_{\nu_\mu} \right)\left(\cos \tfrac{1}{2}\theta_\mu \sin \tfrac{1}{2}\theta_{\nu_e} e^{i\phi_{\nu_e}} - \sin \tfrac{1}{2}\theta_\mu \cos \tfrac{1}{2}\theta_{\nu_e} \right)$$

and

$$|H_{fi}|^2 = 4g^2\left(1 + \cos \theta_{\nu_\mu} \right)\left(1 - \cos \theta_\mu \cos \theta_{\nu_e} \right)$$

after averaging over ϕ_{ν_e}.

We can then use this to calculate the transition probability

$$P = \frac{2\pi}{\hbar}|H_{fi}|^2 \frac{dN_f}{dE} = \frac{2\pi}{\hbar} \int |H_{fi}|^2 dN_f \delta(E_f - E_i) \quad .$$

We have

$$dN_f = \frac{E_e^2 dE_e d\Omega_e}{(2\pi\hbar c)^3} \frac{E_{\nu_\mu}^2 dE_{\nu_\mu} d\Omega_{\nu_\mu}}{(2\pi\hbar c)^3} ,$$

which gives

$$P = \frac{2\pi}{\hbar} \frac{E_e dE_e^2 d\Omega_e}{(2\pi\hbar c)^6} \int 2\pi E_{\nu_\mu}^2 dE_{\nu_\mu} d\left(\cos\theta_{\nu_\mu}\right)$$

$$\times \; |H_{fi}|^2 \delta\left(E_e + E_{\nu_\mu} + E_{\bar{\nu}_e} - 2E_{max}\right) \; ,$$

where E_{max} is the maximum energy of any one particle, $\frac{1}{2} m_\mu c^2$. Evaluation of this expression yields

$$N(E_e,\Omega_e)dE_e d\Omega_e = P$$

$$= \frac{g^2}{2\pi^4\hbar^7 c^6} E_{max} E_e^2 \left[(3E_{max} - 2E_e) + \cos\theta_\mu (E_{max} - 2E_e)\right] dE_e d\Omega_e \; .$$

Integrating over angles finally yields the desired spectrum shape:

$$N(E_e)dE_e = \frac{g^2}{3\pi^3\hbar^7 c^6} E_{max} E_e^2 (3E_{max} - 2E_e) dE_e \; ,$$

or, changing variables to $\varepsilon = \frac{E_e}{E_{max}}$,

$$N(\varepsilon)d\varepsilon = \frac{g^2 (E_{max})^5}{3\pi^3\hbar^7 c^6} \varepsilon^2 (3 - 2\varepsilon) d\varepsilon \; .$$

We can normalize this spectrum to $\int_0^1 N(\varepsilon)d\varepsilon = 1$; this yields

$$N(\varepsilon)d\varepsilon = 2\varepsilon^2 (3 - 2\varepsilon) d\varepsilon \; .$$

As mentioned above, this gives the e^+ spectrum from μ^+ decay, since there is no dependence on spin, and also the antineutrino spectrum.

In general, without taking into account specific helicities, the energy spectrum of the particles emitted in muon decay is given by

$$N(\varepsilon)d\varepsilon = 4\varepsilon^2 \left[3(1 - \varepsilon) + \frac{2}{3}\rho(4\varepsilon - 3)\right] d\varepsilon \text{ (Ref. 17)} ,$$

where ρ is the Michel parameter, which contains all the spin dependence and which can vary between 0 and 1. Assuming the positron and neutrinos are all helicity eigenstates, which is true if the positron mass is neglected, then the positron and antineutrino will have the same energy spectrum, corresponding to $\rho = \frac{3}{4}$, which is that derived above. The neutrino will have a spectrum corresponding to $\rho = 0$, since N must vanish at $\varepsilon = 1$ in order to conserve spin. The neutrino spectrum is therefore

$$N(\varepsilon)d\varepsilon = 12\varepsilon^2(1 - \varepsilon) .$$

---

17. Ibid., p. 214.

3. Inverse Beta Decay

We now discuss the reaction $\bar{\nu}_e p \rightarrow ne^+$.[18] The transition probability for this reaction is given by

$$W = \frac{2\pi}{\hbar} |H|^2 \frac{dN}{dE} \quad .$$

The cross section is given by the transition rate divided by the incoming neutrino flux:

$$d\sigma = \frac{W}{c} = \frac{2\pi}{c\hbar} |H|^2 \frac{dN}{dE} \quad .$$

Taking the coupling constant out of $|H|^2$, and defining $|H|^2 = g^2|M|^2$, we have

$$d\sigma = \frac{2\pi}{c\hbar} g^2 |M|^2 \frac{dN}{dE} \quad .$$

Now,

$$\frac{dN}{dE} = \frac{p_e^2 dp_e}{(2\pi\hbar)^3} \frac{d\Omega_e}{dE_e} = \frac{m^2 c}{(2\pi\hbar)^3} \varepsilon\sqrt{\varepsilon^2 - 1}\, d\Omega_e \quad ,$$

where $\varepsilon = E/mc^2$, and the mass is the mass of the electron. The recoil of the neutron is neglected here. Integrating over angles yields

---

18. Ibid., pp. 207-210.

$$\sigma = \frac{g^2 m^2}{\pi \hbar^4} |M|^2 \varepsilon \sqrt{\varepsilon^2 - 1} \quad .$$

The matrix element $|M|^2$ contains the transitions between initial and final states, summed over the spins.[19] For $E_\nu \sim m_e c^2$ (i.e., $\varepsilon \sim 1$), $|M|^2 \sim 5$.[20]

It has, however, been pointed out by O'Connell[21] that there are energy-dependent weak magnetism terms in $|M|^2$, which were neglected by Wu and Moskowski, which become important at energies of interest for this experiment. He finds for σ (where now $\hbar = c = 1$)

$$\sigma = \frac{G^2}{\pi} p_e E_e \left[1 + 3F_A^2 + \frac{20}{3}\left(\frac{E_\nu \mu_V}{2m_p}\right)^2 - 16F_A\left(\frac{E_\nu \mu_V}{2m_p}\right)\right] \quad .$$

Here, μ_V is the nucleon vector magnetic moment, F_A is the axial vector coupling constant, and $G = 10^{-5}/m_p^2$. We can now take this, multiplied by the antineutrino energy spectrum given above (for the antineutrino from muon decay), and integrate over the energy to get an average cross section. This yields

$$\langle \sigma_{\bar{\nu}_e p} \rangle = 1.69 \times 10^{-40} \text{ cm}^2 \quad .$$

---

19. Ibid., p. 48.

20. Ibid., p. 208.

21. J. S. O'Connell, Los Alamos Scientific Laboratory report LA-5175-MS, March 1973.

O'Connell also calculates the cross section for neutrinos on deuterium:[22]

$$\nu_e d \rightarrow ppe^- \quad .$$

He considers first the $^3S_1 \rightarrow {}^1S_0$ transition, and later adds corrections for higher nucleon partial waves. Using effective range theory for the nuclear wave functions, and integrating numerically over the solid angle and the neutrino energy spectrum, he finds for an average cross section

$$\langle\sigma_{\nu_e d}\rangle = 0.44 \times 10^{-40} \text{ cm}^2 \quad .$$

He then adds corrections for higher nucleon partial waves, and finds

$$\langle\sigma_{\nu_e d}\rangle = 0.48 \times 10^{-40} \text{ cm}^2 \quad .$$

Similar calculations have been done on ^{12}C (Ref. 23) and ^{16}O (Ref. 24) with the following results:

$$\langle\sigma_{\nu_e {}^{12}C}\rangle = 0.146 \times 10^{-40} \text{ cm}^2$$

$$\langle\sigma_{\nu_e {}^{16}O}\rangle = 0.052 \times 10^{-40} \text{ cm}^2 \quad .$$

---

22. Ibid.

23. J. S. O'Connell, T. W. Donnelly, and J. D. Walecka, Phys. Rev. C6, 719 (1972).

24. T. W. Donnelly, Phys. Lett. 43B, 93 (1973).

An estimate has also been made of the reaction[25]

$$\nu_e + {}^{27}\mathrm{Al} \rightarrow e^- + {}^{27}\mathrm{Si}_{g.s.} \quad ,$$

with the result

$$\langle \sigma_{\nu_e} {}^{27}\mathrm{Al} \rangle = 0.23 \times 10^{-40} \ \mathrm{cm}^2 \quad .$$

B. GAUGE THEORIES[26]

1. An Example:

Quantum Electrodynamics as a U(1) Abelian Gauge Theory

Current theories of weak interactions are based on gauge theories. These theories use the symmetry structure of certain groups, such as SU(2) or U(1), to model symmetries of a Lagrangian. The Weinberg-Salam model, which has so far successfully modelled the weak and electromagnetic interactions, is a gauge theory whose group is SU(2) × U(1). We will start our discussion of gauge theories by looking at quantum electrodynamics, which can be described as a gauge theory whose group is U(1). The Weinberg-Salam model contains QED as a subgroup, so this discussion will serve to introduce gauge theories in general and the Weinberg-Salam model in particular.

We begin by reviewing the Lagrangian formalism within the context of gauge theories. Notation will be as follows:

---

25. LAMPF Proposal 20, in LAMPF Neutrino Facility Proposal, op. cit.

26. R. W. Brown, lecture notes, summer 1978.

$\hbar = c = 1$

sum over repeated indices

$x^{\mu} = (t,\vec{x}), x_{\mu} = (t, -\vec{x})$

$$g_{\mu\nu} = g^{\mu\nu} = \begin{pmatrix} 1 & & & \\ & -1 & & \\ & & -1 & \\ & & & -1 \end{pmatrix}$$

$$g_{\mu}{}^{\nu} = g_{\mu\alpha}g^{\alpha\nu} = \begin{pmatrix} 1 & & & \\ & 1 & & \\ & & 1 & \\ & & & 1 \end{pmatrix}$$

$$\partial_{\mu} = \frac{\partial}{\partial x^{\mu}} = \left(\frac{\partial}{\partial t}, \vec{\nabla} \right) \qquad \partial^{\mu} = \frac{\partial}{\partial x_{\mu}} = \left(\frac{\partial}{\partial t}, -\vec{\nabla} \right) .$$

We have, from the invariance of the functional integral of the Lagrangian density $\underset{\sim}{L}$, the Euler-Lagrange equations of motion:

$$\frac{\partial \underset{\sim}{L}}{\partial \phi} - \partial_{\mu} \frac{\partial \underset{\sim}{L}}{\partial(\partial_{\mu}\phi)} = 0 \qquad \underset{\sim}{L} = \underset{\sim}{L}(\phi, \partial_{\mu}\phi) .$$

The free-field equation for a spin $\frac{1}{2}$ particle (the electron), which is the Dirac equation, is then

$$(i\not{\partial} - m)\psi = 0 ,$$

where

$$\not{\partial} = \partial^{\mu}\gamma_{\mu} .$$

This yields the Lagrangian density

$$\underset{\sim}{L} = \bar{\psi}(i\not{\partial} - m)\psi \quad .$$

We now discuss continuous symmetries of the Lagrangian. If a continuous transformation $\phi \to \phi' = U\phi$ leaves the Lagrangian unchanged, it is referred to as a continuous symmetry. We may then use Noether's Theorem to find conserved quantities:

> If any continuous transformation leaves the Lagrangian invariant, and the equations of motion invariant in form, there exists a corresponding conservation law and a constant of motion.

Now, we need to know how to calculate the conserved currents which correspond to the constants of motion. Let us look at an infinitesimal transformation:

$$\phi(x) \to \phi'(x) = \phi(x) + \lambda\phi(x) \quad ,$$

where $|\lambda| << 1$. Then

$$\frac{d\underset{\sim}{L}}{d\lambda} = 0 = \frac{\partial \underset{\sim}{L}}{\partial \phi}\frac{\partial \phi}{\partial \lambda} + \frac{\partial \underset{\sim}{L}}{\partial(\partial_\mu \phi)}\frac{\partial(\partial_\mu \phi)}{\partial \lambda}$$

$$= \partial_\mu\left[\frac{\partial \underset{\sim}{L}}{\partial(\partial_\mu \phi)}\phi\right] \quad .$$

This is an equation of the form $\partial_\mu J^\mu = 0$; we may therefore treat J^μ as a conserved current. More generally, to include transformations among a set of ϕ_i:

$$\phi_i \to \phi_i' = \phi_i + \lambda T_{ij}\phi_j \quad .$$

Then,

$$J^\mu = \frac{\partial \underset{\sim}{L}}{\partial(\partial_\mu \phi_i)} T_{ij}\phi_j \quad .$$

Now, if the surface terms vanish or cancel (these are the same arguments used in classical electrodynamics), then

$$\int \vec{\nabla} \cdot \vec{J} d^3x = 0$$

or,

$$\int d^3x \, \partial_\mu J^\mu = \frac{d}{dt} Q = 0 \quad ,$$

where $Q = \int d^3x \, J^\circ$, a conserved charge. Since $dQ/dt = 0$, then $[Q,H] = 0$ and there exist simultaneous eigenfunctions of Q and H, leading to conserved quantum numbers. Also, Q is the generator of the transformation, in the following sense: if $\phi \to \phi' = U\phi$ where $U = e^{i\Lambda}$, $U = 1 + i\Lambda$ if Λ is infinitesimal ($i\Lambda \to \lambda$ above); then $\delta\phi = i\Lambda\phi$. The generator G of a transformation is defined by

$$\delta\phi = i\Lambda[G,\phi] \quad ;$$

therefore

$$\phi' = e^{i\Lambda G}\phi e^{-i\Lambda G} \quad .$$

But since

$$Q = i \int d^3x \frac{\partial \tilde{L}}{\partial \dot{\phi}} \phi \quad \text{(since } T_{ij} = i\delta_{ij} \text{ here)}$$

and

$$\frac{\partial \tilde{L}}{\partial \dot{\phi}} = \pi \quad ,$$

where

$$\{\pi,\phi\} = i\delta^3(\vec{x} - \vec{x}') \quad ,$$

(we can choose our commutation relations to be at equal time if $dQ/dt = 0$), we have

$$[Q,\phi] = i \int d^3x \left(\pi\{\phi,\phi\} - \{\pi,\phi\}\phi\right)$$

$$= \phi \ ;$$

therefore $Q = G$.

Now we can discuss global gauge invariance. A phase change for constant θ

$$\phi \to \phi' = e^{i\theta}\phi$$

is a global gauge transformation; if the Lagrangian is invariant under this transformation, it is a global symmetry. Then

$$\phi_i \to e^{i\theta Q}\phi_i e^{-i\theta Q} = e^{iq_i\theta}\phi_i \quad ,$$

where q_i is the eigenvalue of Q corresponding to φ_i. Therefore

$$e^{i\theta Q}\underset{\sim}{L}e^{-i\theta Q} = \underset{\sim}{L}$$

if $\sum_i q_i = 0$ for each term -- this is effectively charge conservation. Since $e^{i\theta}$ is unitary (if we call $U = e^{i\theta}$, then $U^{-1} = U^{\dagger}$) and abelian (the elements of the set commute), it is a representation of the group U(1).

Specifically, in the case of the electron:

$$\underset{\sim}{L} = \bar{\psi}(i\partial\!\!\!/ - m)\psi$$

(as above); then the gauge transformation

$$\psi \to e^{ie\theta}\psi \quad ;$$

since this is a U(1) global symmetry, $J_\mu = \bar{\psi}\gamma_\mu\psi$ is conserved. Then:

$$\underset{\sim}{L} = -\frac{1}{4} F^{\mu\nu}F_{\mu\nu} + \bar{\psi}(i\not{\partial} + e\not{A} - m)\psi$$

$$F_{\mu\nu} = \partial_\mu A_\nu - \partial_\nu A_\mu$$

with the equations of motion

$$\partial_\mu F^{\mu\nu} = eJ^\nu$$

$$(i\not{\partial} + e\not{A} - m)\psi = 0 \quad .$$

These are invariant under

$$\psi \to e^{i\theta(x)}\psi$$

$$A_\mu \to A_\mu + \frac{1}{e}\partial_\mu\theta \quad .$$

These, then, are the equations of quantum electrodynamics, with A_μ the four-vector potential.

2. The Weinberg-Salam Model

We can now discuss the Weinberg-Salam model. The Weinberg-Salam model is an SU(2) × U(1) gauge theory which unifies electromagnetic and weak interacions. The discussion will begin with massless leptons, and with just the electron and its neutrino. The muon and its neutrino will be added later. The free-field Lagrangian density is

$$\underset{\sim}{L} = \bar{\nu} i\not{\partial}\nu + \bar{e} i\not{\partial} e \quad ,$$

where ν and e are the fields of the neutrino and electron. Since the neutrino is observed to be in the negative helicity state exclusively,

$$\nu = \nu_L = \frac{1 - \gamma_5}{2} \nu \quad .$$

But the electron can be in either helicity state:

$$e = \left(\frac{(1 + \gamma_5)}{2} + \frac{(1 - \gamma_5)}{2} \right) e = e_R + e_L \quad .$$

Now,

$$\underset{\sim}{L} = \bar{\nu}_L i\partial\!\!\!/ \nu_L + \bar{e}_L i\partial\!\!\!/ e_L + \bar{e}_R i\partial\!\!\!/ e_R \quad ,$$

since

$$\bar{e}_R i\partial\!\!\!/ e_L = \bar{e}_L i\partial\!\!\!/ e_R = 0 \quad .$$

This demonstrates that the two helicity states do not mix in the massless case.

We put the electron and neutrino into a doublet; this will allow for e-ν interactions via $W^{\pm}$ exchange. This gives a left-handed doublet and a right-handed singlet:

$$L = \begin{pmatrix} \nu_L \\ e_L \end{pmatrix} \; ; \quad R = e_R \quad .$$

We now have the transformation

$$L \to UL = e^{i\vec{\theta}\cdot\vec{\sigma}/2} L \; ; \quad R \to R \quad .$$

This is a local symmetry of SU(2) (because of $\vec{\sigma}$), and yields

$$\underset{\sim}{L} = -\frac{1}{4}\vec{F}_{\mu\nu}\cdot\vec{F}^{\mu\nu} + \bar{L}i\left(\not{\partial} - ig\frac{\vec{\sigma}}{2}\cdot\vec{\not{A}}\right)L + \bar{R}i\not{\partial}R \quad ,$$

where

$$\vec{F}_{\mu\nu} = \partial_\mu\vec{A}_\nu - \partial_\nu\vec{A}_\mu + g\vec{A}_\mu \times \vec{A}_\nu \quad .$$

We examine the interaction term more closely:

$$\frac{1}{2}g\bar{L}\vec{\sigma}\cdot\vec{\not{A}}L = \frac{1}{2}g(\bar{\nu}_L\bar{e}_L)\left[\not{A}^1\begin{pmatrix} e_L \\ \nu_L \end{pmatrix} + i\not{A}^2\begin{pmatrix} -e_L \\ \nu_L \end{pmatrix} + \not{A}^3\begin{pmatrix} \nu_L \\ -e_L \end{pmatrix}\right]$$

$$= \frac{1}{2}g\left[\bar{\nu}_L(\not{A}^1 - i\not{A}^2)e_L + \bar{e}_L(\not{A}^1 + i\not{A}^2)\nu_L + \bar{\nu}_L\not{A}^3\nu_L - \bar{e}_L\not{A}^3e_L\right] \quad .$$

We see that interactions between ν and e are mediated by $\frac{1}{\sqrt{2}}(A^1_\mu + iA^2_\mu) = W_\mu$; then $W^+_\mu = \frac{1}{\sqrt{2}}(A^1_\mu - iA^2_\mu)$. The action of the W field is to create W^+ intermediate vector bosons, and to destroy W^-. In explicit V-A form,

$$\frac{\sqrt{2}}{2}g\bar{\nu}_L\not{W}^+e_L = \frac{1}{\sqrt{2}}g\frac{1}{2}\bar{\nu}\gamma_\mu(1-\gamma_5)eW^{\mu+} \quad ,$$

where we can define

$$g_W = -\frac{1}{\sqrt{2}}g \quad .$$

Note that A^3 cannot represent the photon field, since it mediates $\nu \leftrightarrow \nu$ coupling, and since it interacts only with e_L and not with e_R. We still have a U(1) symmetry to gauge; for this we can define a "weak hypercharge", $Y = N_R + \frac{1}{2} N_L$, where N_R and N_L are the right- and left-handed lepton numbers. In analogy with strong interactions, $Q = T_3 - Y$, where Q is the charge and T_3 is the third component of the weak isospin. T_3 can be found from the doublet and singlet assignments of ν_L, e_L, and e_R. We can now gauge the hypercharge:

$$L \to e^{i\theta/2} L \; ; \quad R \to e^{i\theta} R \quad ,$$

since $Y = \frac{1}{2}$ for L and $Y = 1$ for R. Then

$$\underset{\sim}{L} = -\frac{1}{4} \vec{F}_{\mu\nu} \cdot \vec{F}^{\mu\nu} - \frac{1}{4} B_{\mu\nu} B^{\mu\nu} + \bar{L} i \left(\not{\partial} - ig \frac{\vec{\sigma}}{2} \cdot \vec{\not{A}} - i \frac{1}{2} g' \not{B} \right) L$$

$$+ \bar{R} i (\not{\partial} - i g' \not{B}) R \quad ,$$

where

$$B_{\mu\nu} = \partial_\mu B_\nu - \partial_\nu B_\mu \quad .$$

The interaction term is

$$\frac{1}{2\sqrt{2}} g \left[\bar{\nu} \gamma_\mu (1 - \gamma_5) e W^{\mu +} + \text{h.c.} \right] + \frac{1}{2} \bar{\nu}_L \left[g \not{A}^3 + g' \not{B} \right] \nu_L$$

$$+ \frac{1}{2} \bar{e}_L \left[-g \not{A}^3 + g' \not{B} \right] e_L + g' \bar{e}_R \not{B} e_R \quad .$$

We redefine the fields A_3, $B \to Z$, A:

$$Z_\mu = \frac{1}{\sqrt{g^2 + g'^2}} \left(g A_\mu^3 + g' B_\mu \right)$$

$$A_\mu = \frac{1}{\sqrt{g^2 + g'^2}} \left(-g' A_\mu^3 + g B_\mu \right) ,$$

so the neutral current part of $\underset{\sim}{L}$ is

$$\frac{1}{2} \sqrt{g^2 + g'^2}\, \bar{\nu}_L \not{Z} \nu_L + \frac{1}{\sqrt{g^2 + g'^2}} \left[\frac{g'^2 - g^2}{2} \bar{e}_L \not{Z} e_L + g'^2 \bar{e}_R \not{Z} e_R \right]$$

$$+ \frac{g g'}{\sqrt{g^2 + g'^2}} \left[\bar{e}_L \not{A} e_L + \bar{e}_R \not{A} e_R \right]$$

If we define $e = gg' / (g^2 + g'^2)^{1/2}$, A is the same as the A in quantum electrodynamics (above), and we have recovered the electromagnetic interaction, with no couplings to the neutrinos.

Because the transformation of the fields A_3, $B \to Z$, A preserves the normalization, it can be expressed in terms of an angle:

$$\begin{pmatrix} Z_\mu \\ A_\mu \end{pmatrix} = \begin{pmatrix} \cos\theta_W & \sin\theta_W \\ -\sin\theta_W & \cos\theta_W \end{pmatrix} \begin{pmatrix} A_\mu^3 \\ B_\mu \end{pmatrix} ,$$

where θ_W is the Weinberg angle. In terms of g and g', above:

$$\cos\theta_W = \frac{g}{\sqrt{g^2 + g'^2}} \; ; \quad \sin\theta_W = \frac{g'}{\sqrt{g^2 + g'^2}} \; ; \quad \tan\theta_W = g'/g \; ,$$

and

$$e = g \sin\theta_W \; .$$

Finally, the massless Weinberg-Salam model for e,ν_e can be written

$$\begin{aligned} \mathcal{L}_{e,\nu_e} = & -\frac{1}{4}\,{}^{*}F_{\mu\nu}\cdot{}^{*}F^{\mu\nu} - \frac{1}{4}B_{\mu\nu}B^{\mu\nu} + \bar{\nu}_{eL}i\partial\!\!\!/\nu_{eL} + \bar{e}i\partial\!\!\!/e \\ & + \frac{e}{2\sqrt{2}\sin\theta_W}\left[\bar{\nu}_e\gamma_\mu(1-\gamma_5)eW^{\mu+} + \bar{e}\gamma_\mu(1-\gamma_5)\nu_e W^{\mu}\right] \\ & + e\bar{e}\gamma_\mu eA^\mu + \frac{e}{2\sin 2\theta_W}\left[\bar{\nu}_e\gamma_\mu(1-\gamma_5)\nu_e\right. \\ & \left. + \bar{e}\gamma_\mu(4\sin^2\theta_W - 1 + \gamma_5)e\right] Z \end{aligned}$$

(care should be taken not to confuse the e which is the charge with the e which is the electron field). The muon and its neutrino can be added simply by inserting extra terms of exactly the same form as the terms above involving ν_e and e, but which involve the fields ν_μ and μ instead. Then

$$\mathcal{L}_{tot} = \mathcal{L}_{e,\nu_e} + \bar{\nu}_{\mu L} i\not{\partial} \nu_{\mu L} + \bar{\mu} i \not{\partial} \mu$$

$$+ \frac{e}{2\sqrt{2}\sin\theta_W} \left[\bar{\nu}_\mu \gamma_\mu (1 - \gamma_5) \mu W^{\mu +} + \bar{\mu} \gamma_\mu (1 - \gamma_5) \nu_\mu W^\mu \right] + e \bar{\mu} \gamma_\mu \mu A^\mu$$

$$+ \frac{e}{2 \sin 2\theta_W} \left[\bar{\nu}_\mu \gamma_\mu (1 - \gamma_5) \nu_\mu + \bar{\mu} \gamma_\mu (4\sin^2\theta_W - 1 + \gamma_5) \mu \right] Z \quad .$$

The parameters $\sin\theta_W$ and the fields W^μ and Z are taken to be the same for muons and electrons, in order to preserve μ-e universality.

Masses in the theory arise from spontaneous symmetry breaking. By inserting mass terms in the Lagrangian -- these take the form of interactions between e_L and e_R, since a massive electron is not an eigenstate of helicity -- it is possible to derive masses for the W and Z fields in terms of the Weinberg angle.

The model in this form does not have electron and muon fields mixing in any way, i.e. there is no interaction written down involving both e and μ. This leads to an additive muon conservaton number. However, the additive number does not correspond to any kind of gauge invariance; the only gauge symmetries are charge conservation and right- and left-handed lepton number conservation (helicity conservation). This means that if interactions which violated an additive muon number were observed, as in the decay $\mu \to e\gamma$, such an interaction term could be added. This involves putting e and μ in the same multiplet. There also has been no mention of the tau lepton.[27] It can be added in exactly the

27. M. L. Perl et al., Phys. Lett. 70B, 487 (1977).

same manner as the muon and its neutrino, and this procedure clearly generalizes to any number of leptons, each with its own neutrino. A generalization of this theory which leads to a multiplicatively conserved lepton number will be discussed below.

C. THEORETICAL CONSIDERATIONS OF $\bar{\nu}_e$ FROM μ^+ DECAY

1. Multiplicative Law

The need for a muon number conservation law in addition to a lepton number conservation law was first suggested by the absence of neutrinoless μ-e transitions, such as $\mu \to e\gamma$, $\mu \to 3e$, and $\mu Z \to eZ'$. Current limits on these transitions are as follows:

$$\mu^- \to e^-e^-e^+ < 1.9 \times 10^{-9} \text{ (Ref. 28)}$$

$$\mu \to e\gamma < 1.9 \times 10^{-10} \text{ (Ref. 29)}$$

$$\mu Z \to eZ' < 4 \times 10^{-10} \text{ (Ref. 30)} \ .$$

These processes are allowed by an additive lepton number conservation law -- one which assigns lepton number as indicated in Table I and then demands that the total number of leptons be conserved. An additive law of muon number conservation can be formulated in a corresponding way, with quantum number assignments as in Table II. This does not replace lepton number conservation, but supplements it. This conservation law requires the existence of two neutrinos, one with nonzero muon number.

---

28. S. M. Korenchenko et al., Soviet Physics JETP 43, 1 (1976).

29. J. D. Bowman et al., Phys. Rev. Lett. 42, 556 (1979).

30. A. Badertscher et al., Phys. Rev. Lett. 39, 1385 (1977).

TABLE I

LEPTON NUMBER ASSIGNMENT

Particle	Lepton Number
e^-, μ^-, ν	+1
$e^+, \mu^+, \bar{\nu}$	-1
all others	0

TABLE II

MUON NUMBER ASSIGNMENT

Particle	Muon Number
μ^-, ν_μ	+1
$\mu^+, \bar{\nu}_\mu$	-1
all others	0

An alternative formulation of the additive law would be to have electron and muon number conserved separately; this automatically conserves total lepton number, which is the sum of electron and muon numbers.

Because all the unobserved reactions listed above involve odd numbers of muons and electrons, it is possible to forbid them with a multiplicative conservation law as well.[31] This law involves a muon "parity", assigned again as in Table II, but which is conserved in the following manner:

31. G. Feinberg and S. Weinberg, Phys. Rev. Lett. 6, 381 (1961).

$$\Pi(-1)^{L_\mu} = \text{constant}$$

(this discussion concerns itself only with the muon and electron; generalizations which include the tau will be considered later.) This law allows all reactions allowed by the additive law, forbids the reactions listed above, but allows reactions involving even numbers of muons and electrons which are forbidden by the additive law, such as

$$\mu^+ \to e^+\bar{\nu}_e\nu_\mu, \quad \mu^+e^- \to \mu^-e^+, \quad \text{and} \quad e^-e^- \to \mu^-\mu^- \ .$$

A multiplicative conservation law can be a consequence of μ-e universality. If the universality derives from a permutation symmetry of two primitive leptons e′ and μ′, which can make transitions e′ ↔ μ′, the observed particles will not be e′ and μ′ but $e = (e' + \mu')/\sqrt{2}$ and $\mu = (\mu' - e')/\sqrt{2}$. The transition e′ → μ′ then corresponds to e → e and μ → −μ, which leads to a muon "parity" which is multiplicatively conserved as described above. In the absence of a specific model, no coupling constant for the decays allowed only by the multiplicative law can be assumed. It has been shown by Cabibbo and Gatto[32] that this formulation leads to two neutrinos which obey the same conservation law.

Other forms of lepton conservation laws have also been proposed. One, by Konopinski and Mahmoud[33] assigns L = +1 to e^-, μ^+, ν_e, and $\bar{\nu}_\mu$, and L = −1 to e^+, μ^-, $\bar{\nu}_e$, and ν_μ. This forbids reactions of the form $\mu^+e^- \to \mu^-e^+$ and $\mu^-Z \to e^-Z'$, but allows $\mu^-Z \to e^+(Z - 2)$ and $K^+ \to \pi^-e^+\mu^+$, although these reactions are forbidden dynamically. The rate expected

32. N. Cabibbo and R. Gatto, Phys. Rev. Lett. 5, 114 (1960).

33. Konopinski and Mahmoud, Phys. Rev. 92, 1045 (1953).

in this model for these interactions has been calculated by Primakoff and Rosen[34] who find

$$R\left[\frac{\mu^- Z \to e^+(Z-2)}{\mu^- Z \to \nu_\mu (Z-1)}\right] = R\left[\frac{K^+ \to e^+\mu^+\pi^-}{K^+ \to \mu^+\nu_\mu\pi^\circ}\right] \lesssim 3.2 \times 10^{-14} \ .$$

Present experimental limits for μ^- to e^+ conversion on a nucleus are $R < 1.5 \times 10^{-9}$,[35] and for the kaon decay, $R \leq 1.4 \times 10^{-8}$.[36] Pontecorvo[37] in a general survey considers all the above formulations as well as one where $L = +1$ for e^- and ν_e and $+2$ for μ^- and ν_μ; this is indistinguishable from the additive law if there are only two leptons. It is not obvious how to incorporate the τ here.

A recent paper by Derman[38] extends the permutation symmetry idea above to include the tau and its neutrino, and explores the consequences of this symmetry in terms of the Weinberg-Salam model. This symmetry leads to the existence of Higgs bosons which carry lepton flavor. Derman shows that in order to have an e-μ-τ mass matrix which is completely nondegenerate, one is forced to a unique selection of a vacuum state. This vacuum preserves a two-fold permutation symmetry, which leads to a multiplicatively conserved quantum number, π, where $\pi = \pm 1$. This number is different for e and μ, but the τ must have the same quantum number as either e or μ; the model therefore has important

34. H. Primakoff and S. P. Rosen, Phys. Rev. D5, 1784 (1972).

35. A. Badertscher et al., Phys. Lett. 79B, 371 (1978).

36. E. W. Beier et al., Phys. Rev. Lett. 29, 678 (1972).

37. B. Pontecorvo, Soviet Phys. JETP 26, 984 (1968).

38. Emanuel Derman, Phys. Rev. D19, 317 (1979).

consequences for τ decay modes. The following is a compilation of some of the experimental consequences of Derman's theory, using his assignment $\pi_\tau = \pi_\mu = -\pi_e$. (The other possibility is $\pi_\tau = \pi_e = -\pi_\mu$; this results in the replacement of μ by e in the τ decays.)

$\tau \to \mu\gamma$: branching ratio $\sim 4 \times 10^{-4}$ assuming $M_{Higgs} \sim 5$ GeV. Lower limit: $> 2 \times 10^{-9}$ since at least one Higgs boson must have mass <250 GeV

$\tau \to 3\mu$: branching ratio $\sim 7 \times 10^{-4}$, but could be much smaller if all $\pi = 1$ Higgs bosons are very heavy (unlike $\tau \to \mu\gamma$, $\tau \to 3\mu$ goes through $\pi = +1$ boson exchange only)

$\tau \to \mu ee$: branching ratio $\sim 7 \times 10^{-4}$. Lower limit: $\gtrsim 10^{-10}$. Similar to $\tau \to \mu\gamma$.

$e^+\mu^- \to e^-\mu^+$: amplitude $\sim G_F m_\tau^2/m_{K,L}^2$ where K, L are $\pi = -1$ Higgs bosons. Present upper limit on this is $< 5800\ G_F$.[39]

$\mu^+ \to e^+ \bar{\nu}_e \nu_\mu$: amplitude $\sim G_F m_\tau^2/m_H^2$ where H is a $\pi = -1$ Higgs boson. For $m_H \sim 5$ GeV, amplitude $\sim 0.13\ G_F$, branching ratio ~2%.

Derman extends this model to the quark sector, which has consequences for b quark decay and for the Higgs boson masses. Since the $\pi = +1$ bosons mediate the interactions $\pi^+ \to e^+\nu_e$, $K^o \to \bar{K}^o$, and $K^o \to e^+e^-$, their masses must be large to be consistent with the experimentally observed rates of these processes. This means that these masses must be at least several hundred GeV. No such limit exists, however, on the masses of the $\pi = -1$ bosons, since the interactions they mediate are not subject to very stringent experimental limits. Note that this model is valid for the three-lepton case only. If more heavy

39. R. Amato et al., Phys. Rev. Lett. 21, 1709 (1968).

leptons are discovered, the model would have to be completely reformulated.

2. Neutrino Oscillations and Decay

In the presence of a muon number violating interaction and different ν_e and ν_μ masses, it is possible to have neutrino oscillations and muon neutrino decay (assuming $m_{\nu_\mu} > m_{\nu_e}$). Decay could occur via the reaction $\nu_\mu \rightarrow \nu_e\gamma$, and will be discussed below. Oscillations could occur if the physical neutrinos ν_e and ν_μ are superpositions of two fundamental neutrinos ν_1 and ν_2 with definite masses m_1 and m_2. Then ν_e and ν_μ are not stationary states and do not have definite masses. To be specific about the formulation of the mixing, $\nu_e = \cos\theta\nu_1 + \sin\theta\nu_2$ and $\nu_\mu = -\sin\theta\nu_1 + \cos\theta\nu_2$. The angle θ describes the strength of the mixing; the oscillation length will depend on θ and on $|m_1 - m_2|$. Note that this may superficially resemble the $e' - \mu'$ mixing described at the beginning of this section. The difference is that e' and μ' were assumed to have identical masses, because of universality. This led to a strict separation between the physical e and μ, rather than the mixing one gets with different masses.

The theory of neutrino oscillations will now be formulated in more detail.[40] The state vectors of the electron and muon neutrinos are $|\nu_e\rangle$ and $|\nu_\mu\rangle$; of the fundamental neutrinos $|\nu_1\rangle$ and $|\nu_2\rangle$. Then

$$|\nu_\ell\rangle = \sum_{\sigma=1,2} U_{\ell\sigma}|\nu_\sigma\rangle \qquad \ell = e,\mu \ ,$$

where

40. S. M. Bilenky and B. Pontecorvo, Phys. Reports 41, 225 (1978).

$$U_{\ell\sigma} = \begin{pmatrix} \cos\theta & \sin\theta \\ -\sin\theta & \cos\theta \end{pmatrix} .$$

Since $|\nu_\sigma\rangle$ are the eigenstates of the Hamiltonian,

$$H|\nu_\sigma\rangle = E_\sigma|\nu_\sigma\rangle .$$

A beam of neutrinos created at time $t = 0$ will be pure $|\nu_\ell\rangle$ ($\ell = e,\mu$).

At time t the state vector of the beam will be

$$|\nu_\ell\rangle_t = e^{-iHt}|\nu_\ell\rangle = \sum_{\sigma=1,2} U_{\ell\sigma} e^{-iE_\sigma t}|\nu_\sigma\rangle$$

$$= \sum_{\ell'=e,\mu} a_{\nu_{\ell'},\nu_\ell}(t)|\nu_{\ell'}\rangle$$

where

$$a_{\nu_{\ell'},\nu_\ell}(t) = \sum_{\sigma=1,2} U_{\ell\sigma} e^{-iE_\sigma t} U_{\ell'\sigma} .$$

The transition probability is then

$$W_{\nu_{\ell'},\nu_\ell} = \sum_{\sigma,\sigma'} U_{\ell\sigma}U_{\ell'\sigma}U_{\ell\sigma'}U_{\ell'\sigma'} \cos(E_\sigma - E_{\sigma'})t$$

If $p_\nu >> m_1, m_2$, then

$$E_1 - E_2 \simeq \frac{m_1^2 - m_2^2}{2p_\nu} .$$

Then

$$W_{\nu_\ell, \nu_\ell} = 1 - \frac{1}{2} \sin^2 2\theta \left(1 - \cos \frac{2\pi R}{L}\right)$$

$$W_{\nu_\ell, \nu_{\ell'}} = \frac{1}{2} \sin^2 2\theta \left(1 - \cos \frac{2\pi R}{L}\right) ; \quad \ell \neq \ell' ,$$

which is the probability of finding $\nu_{\ell'}$ at a distance R from a source of ν_ℓ; the oscillation length L is defined as follows:

$$L = \frac{4\pi p_\nu}{|m_1^2 - m_2^2|} .$$

Application to the present experiment requires averaging over the finite detector size and the neutrino energy spectrum; this will be discussed with the results.

The subject of neutrino decay is also discussed by Bilenky and Pontecorvo;[41] they derive for the probability of the decay $\nu_1 \to \nu_2\gamma$ the expression

$$\Gamma(\nu_1 \to \nu_2\gamma) = \frac{9}{16} \frac{G^2\alpha}{128\pi^4} m_1^5 \sin^2\theta \cos^2\theta \, (M_\mu^2/M_w^2)^2 .$$

Using the extreme values $\theta = \frac{1}{4}$, $m_1 = 1$ MeV, evaluation of this expression yields a lifetime in the ν_1 rest frame of $\tau_1 \cong 5 \times 10^{11}$ years. Neutrinos of momentum 20 to 60 MeV/c, as in this experiment, will have $\beta \cong 1$; the time dilation effect in the lab will make the apparent lifetime even longer. From this we conclude that neutrino decay may be neglected here.

41. Ibid., p. 238.

CHAPTER 2

EXPERIMENTAL APPARATUS

A. CERENKOV COUNTER

We begin with a brief discussion of Cerenkov radiation.[42] A charged particle moving with constant velocity through a material can radiate if its velocity is higher than the velocity of light in the medium. The radiation will be emitted at an angle given by

$$\cos \theta_c = c'/v \quad ,$$

where c' is the velocity of light in the medium. It can then be shown that the total energy radiated per unit frequency interval per unit path length by a particle will be

$$\frac{dI(\omega)}{dx} = \frac{e^2\omega}{c^2}\left(1 - \frac{1}{\beta^2\varepsilon}\right) \quad ,$$

where $\beta = v/c$ and ε is the dielectric constant, assumed to be a function of ω. Assuming that ε is constant through the visible and near-ultraviolet regions, which are of interest here, the amount of radiation is directly proportional to ω. Also, since dI/dx is not a function of x, the amount of light emitted will depend on the distance

42. J. D. Jackson, Classical Electrodynamics, John Wiley and Sons, Inc., New York, 1962, pp. 494-499.

traveled. If the size of the detector is large compared to the range of the particle, the total amount of light will be proportional to the energy of the particle, assuming that β stays constant. In our case, we wish to measure electron energies of 20 to 60 MeV; β for electrons will be constant down to energies of the order of 1 MeV, so this is a good assumption.

The Cerenkov counter, illustrated in Fig. 1, was a cube 1.8 m on a side, with cast epoxy walls. Nonmetal construction was chosen to minimize electron-neutrino interactions in the walls, since electron-neutrino cross sections are known to be small on carbon and oxygen (as detailed in the theoretical section). The cubical shape, while it was not ideal hydrostatically, maximized the active water volume inside a box of flat scintillators used as an active cosmic-ray shield.

The Cerenkov counter was fabricated by the Formcrete Company.[43] The walls were made from EPON 828 resin,[44] with curing agent Z[45] and 10% woodflour filler, and were 1.3-cm thick. Each wall was cast independently, then cured at 65°C for 14 hours. Five sides of the counter were then assembled inside an aluminum L-bar frame, illustrated in Fig. 2, with 3-cm diagonal epoxy filling (EPON 872,[46] curing agent Z) completing the cube. The top of the counter was a removable lid bolted down over a rubber gasket; it was otherwise identical to the other sides.

---

43. Formcrete Co., P. O. Box 1153, Manchester, CT 06040.

44. Shell Chemical Co., One Shell Plaza, P. O. Box 2463, Houston, TX 77001.

45. Shell Chemical Co., as above.

46. Shell Chemical Co., as above.

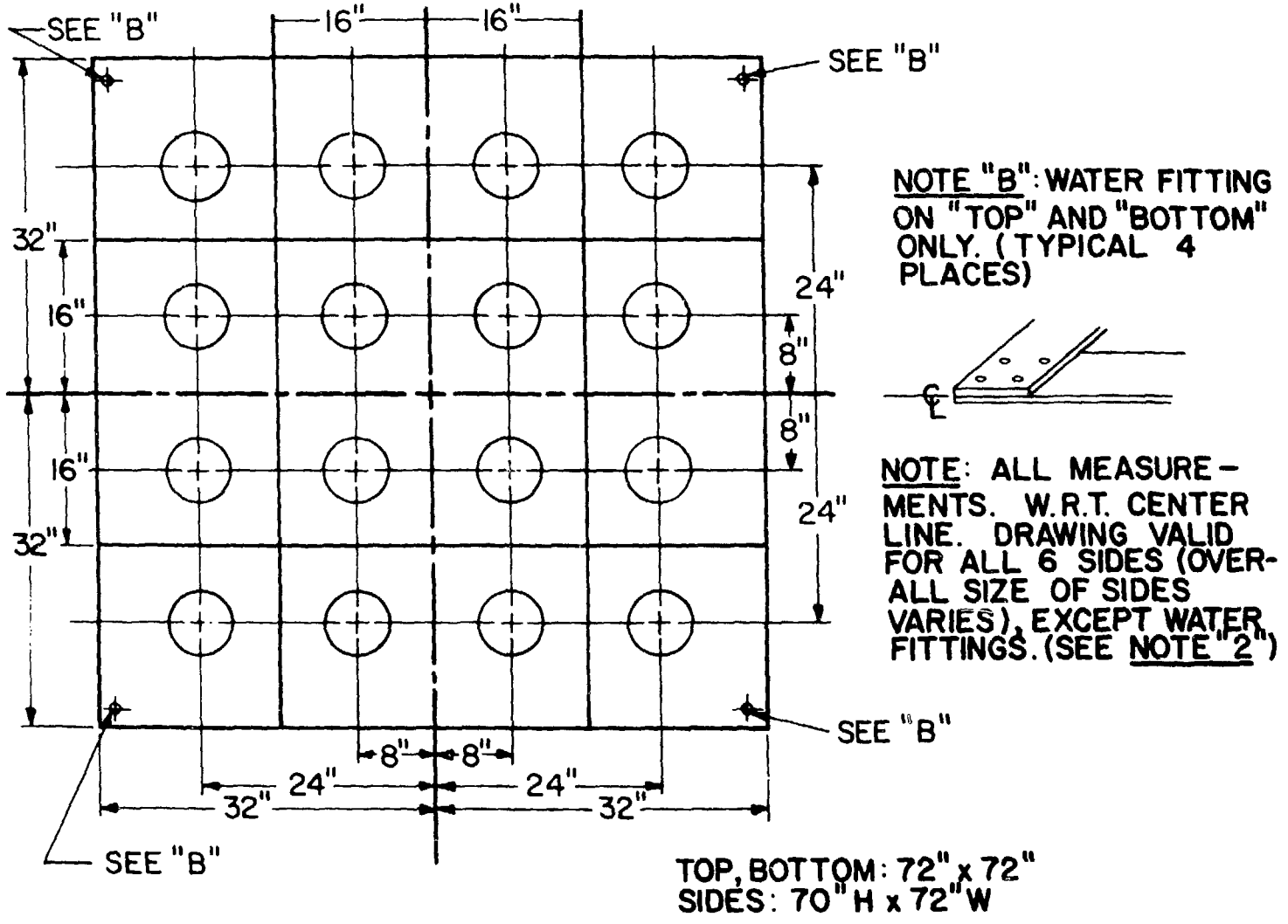

Fig. 1. Cerenkov counter.

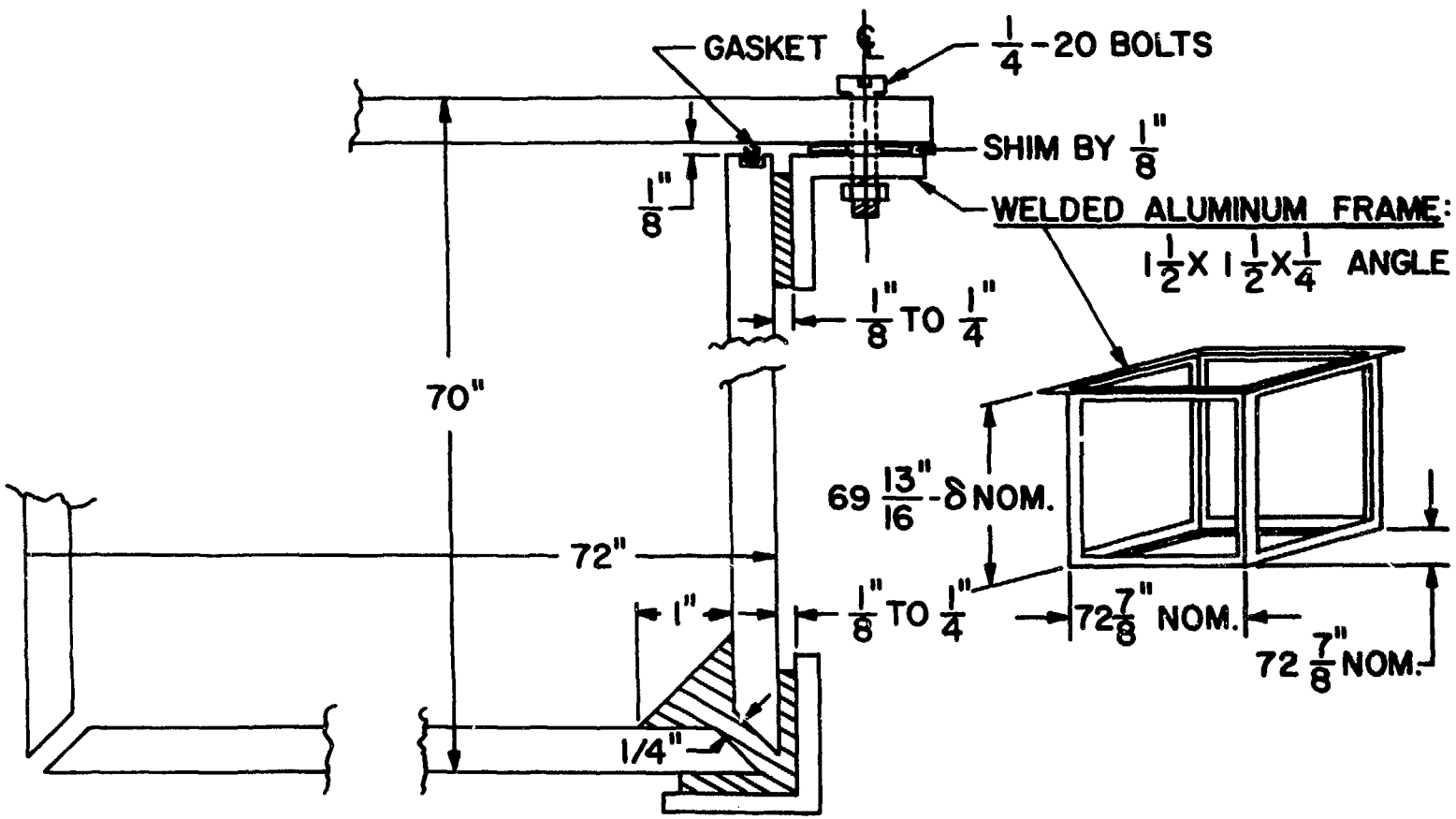

Fig. 2. Counter assembly and aluminum frame.

The epoxy walls themselves did not have sufficient strength to withstand the hydrostatic pressure of the counter. A system of struts, illustrated in Fig. 3, which were perpendicular to the walls of the counter, was used to provide mechanical integrity. The struts were cut from 1.3-cm-thick Benelex,[47] a cellulose laminate, chosen because of its exceptional stiffness (its modulus of elasticity is 1.3×10^6 psi), and also because of the desire to use nonmetallic materials. The struts were slotted at their intersections, bonded to the epoxy walls, and bolted together at the corners. They held the deflection of the counter walls to less than 3 cm.

The portholes for the 96 phototubes were distributed in a square matrix, 16 on each of the 6 sides, in the spaces formed by the Benelex ribs. We did not use transmission windows, in order to minimize light losses; the water seal was formed directly by the 12.5-cm tube faces. The precast epoxy porthole rings, illustrated in Fig. 4, were cast into the epoxy walls. Each porthole ring contained an O-ring groove and threaded inserts for attaching a matching epoxy follower ring. The follower rings are shown in Fig. 5. The phototubes were bonded into the follower rings with RTV 602 silicone rubber.[48] A fiber-optics light guide, its tip bonded to the tube face, was incorporated into the assembly to allow individual testing of the tubes. The light guides went to green LEDs, three guides per LED, which were mounted on the corners of the counter. The phototube assembly is shown in Fig. 6.

47. Masonite Corp., 29 N. Wacker Drive, Chicago, IL 60606.

48. General Electric Silicone Products Department, Waterford, NY 12188.

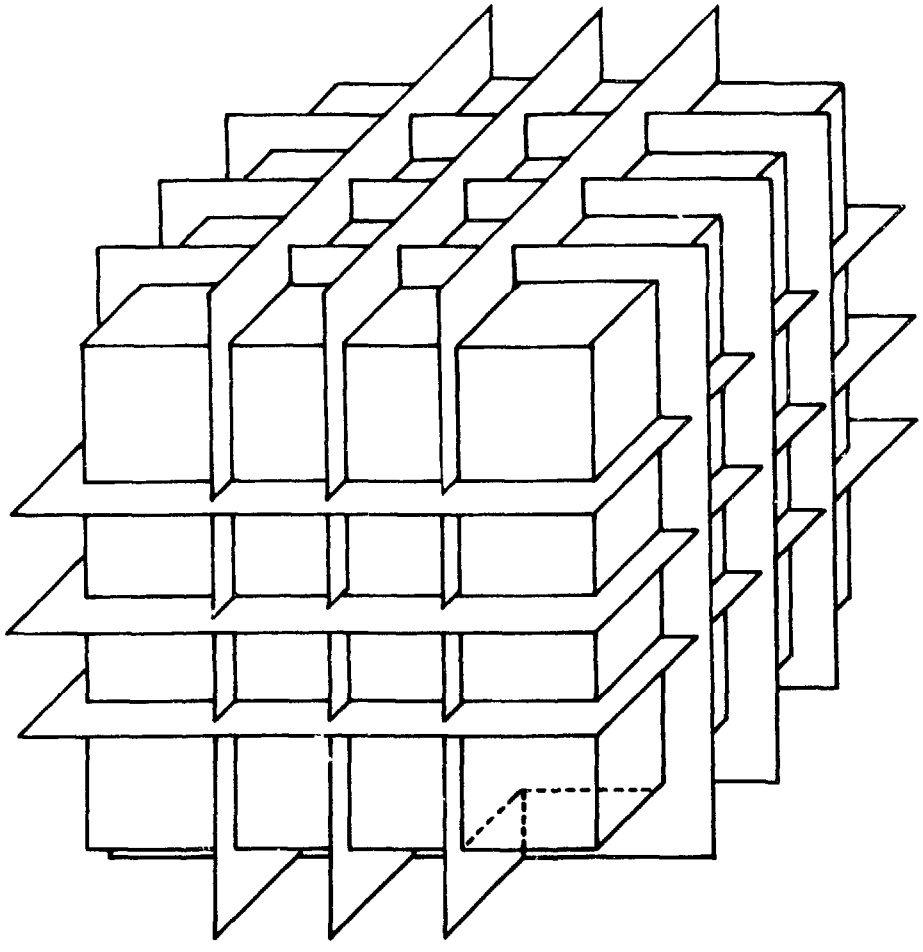

OVERALL: 90"x 90" x 88"
HIGH ($\pm \frac{1}{4}$")

SIDES AND TOP: WIDE AND NARROW STRUTS.

BOTTOM: ALL WIDE STRUTS.

SIDES NOT SHOWN: SAME ORIENTATION AS FACING

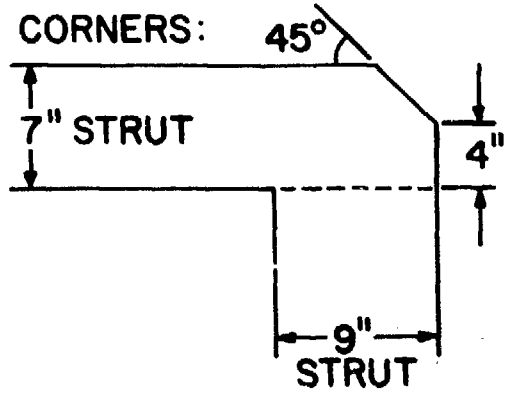

Fig. 3. Orientation of struts.

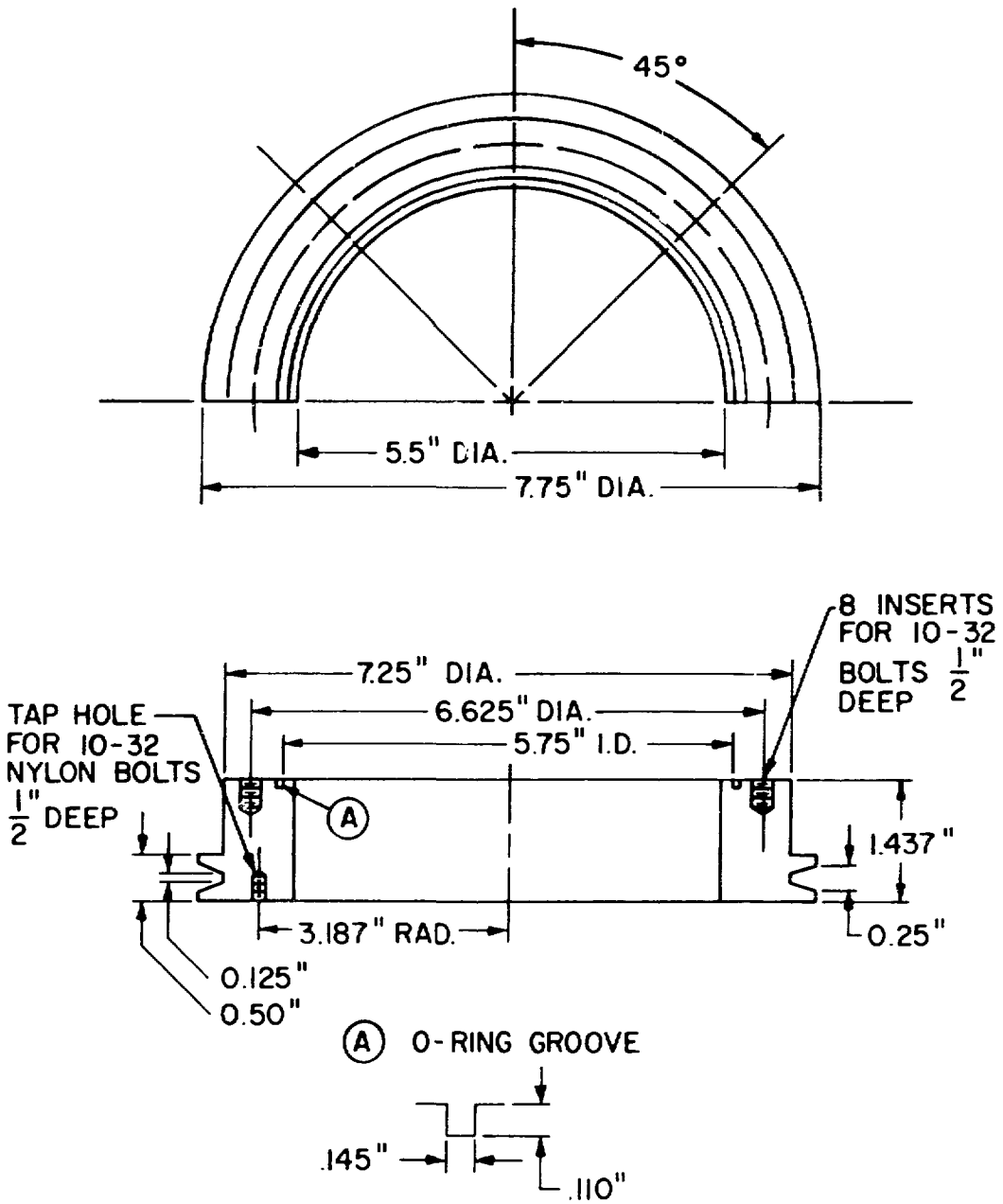

Fig. 4. Porthole ring.

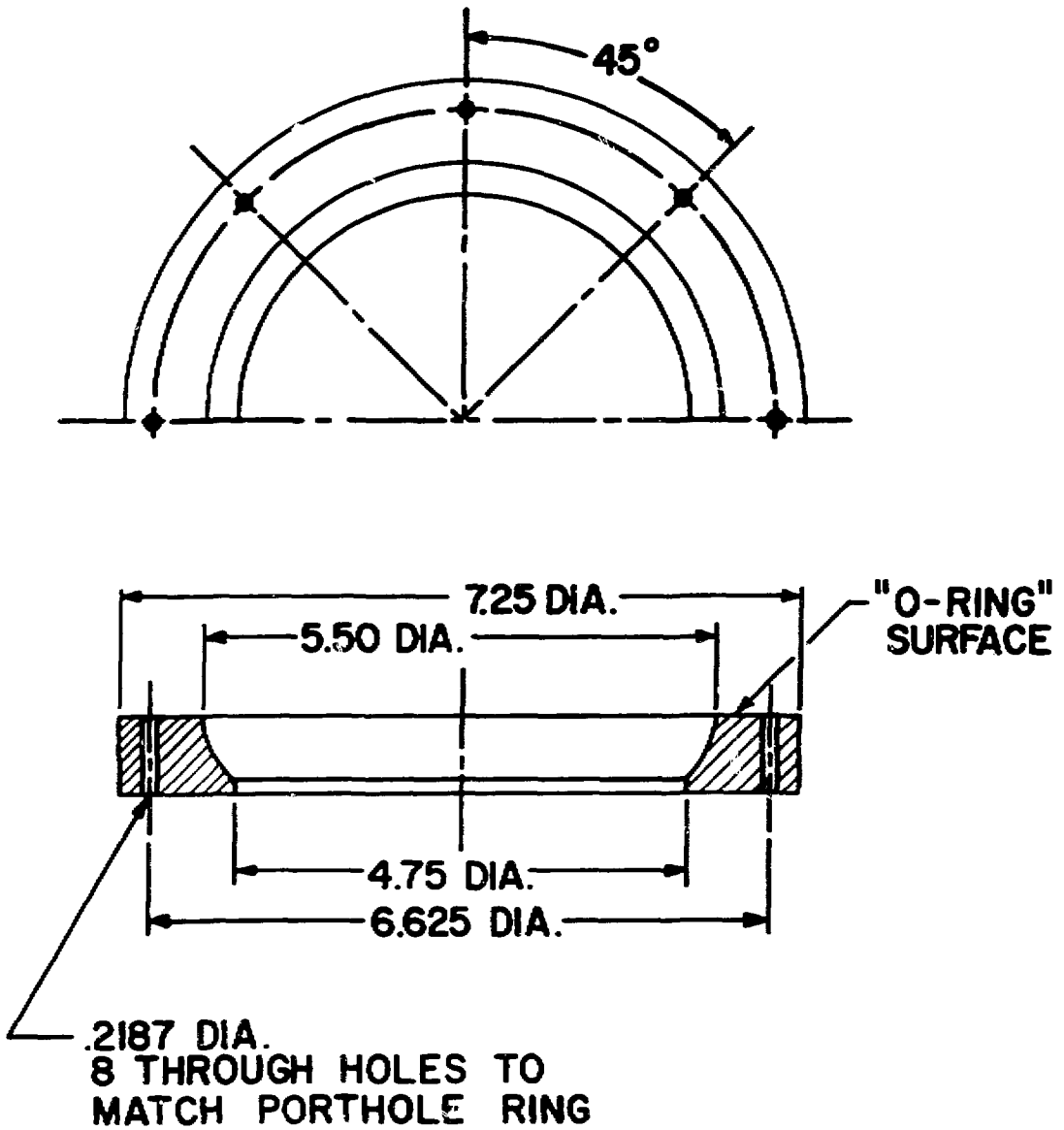

Fig. 5. Follower ring.

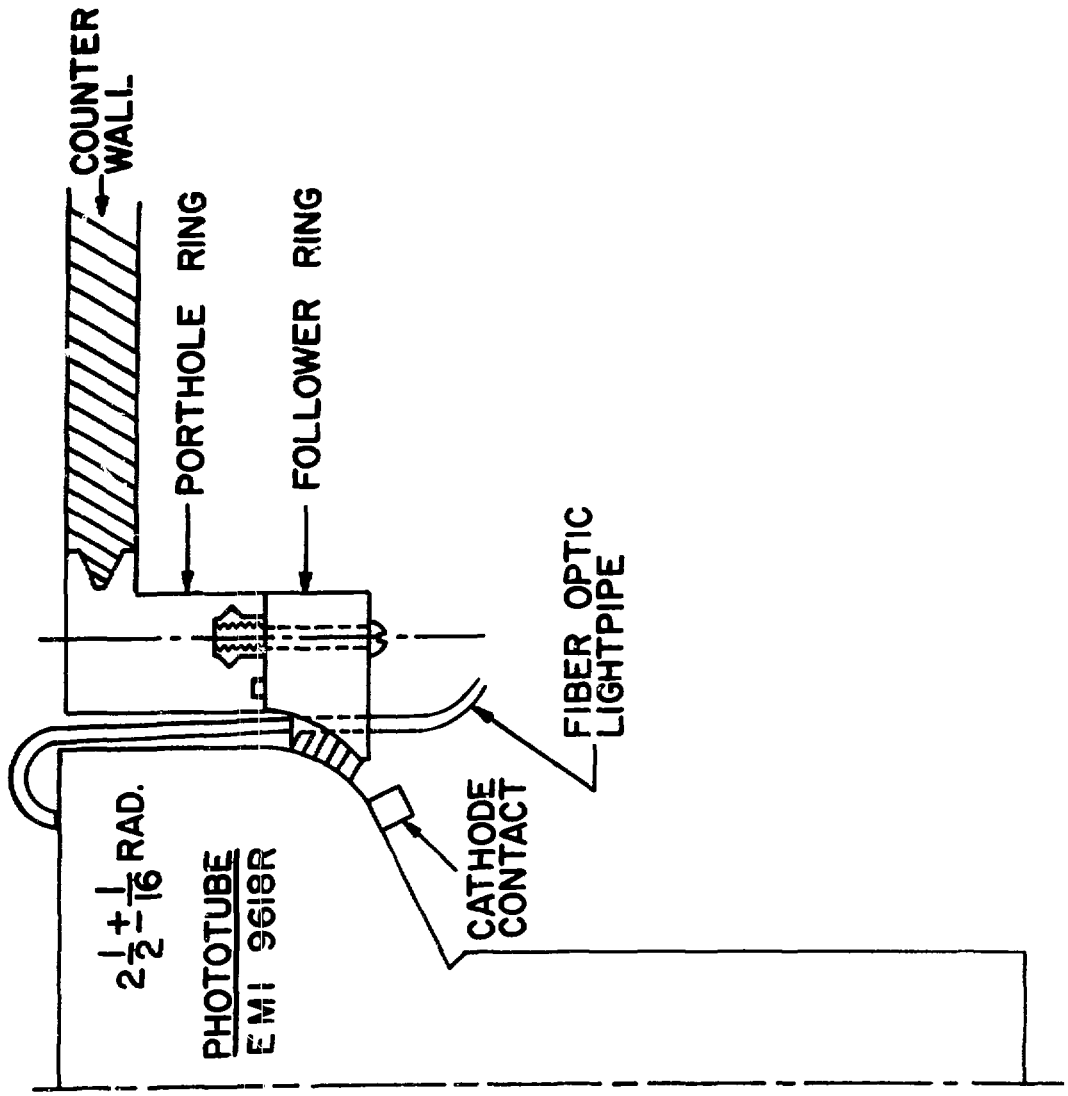

Fig. 6. Phototube assembly.

The counter was lined with a diffuse white reflector made of 0.15-cm-thick Kydex sheets,[49] with holes cut for the phototubes, and attached to the counter walls with nylon screws. Tests were made resulting in the selection of the Kydex, using the same water and wavelength shifter solution as was used in the counter, illuminated by an ultraviolet light, and viewed indirectly by a single phototube. The setup is illustrated in Fig. 7. Note that the phototube was not at the angle of reflection for a smooth surface -- this was because we were interested in measuring diffuse reflection. Table III shows the results from various samples, normalized to boric acid = 100. Boric acid and magnesium oxide are powders, and were judged to be too difficult to use successfully underwater. The Kydex was similar to the teflon in diffuse reflectivity, and was much less expensive. The top and bottom sides of the cube had 2-cm-diam water fittings cast into their corners; their location is indicated in Fig. 1. Each of the 16 porthole rings on the top had a 0.3-cm inside diameter Tygon tube[50] attached to prevent the formation of air bubbles under the phototubes. Tygon tubes also connected all the counter fittings to plastic manifolds with PVC valves (see Fig. 8), located outside the scintillator shield. These manifolds allowed for filling, emptying, and circulating while the counter was inaccessible behind the cosmic-ray anticoincidence shield. The opening to the air allowed for changes in the water level due to leaks or thermal expansion or contraction, and also for air intake and outgo while the counter was being emptied or filled.

---

49. Rohm and Haas Co., Johnson and Thomas St., Philadelphia, PA 19105.

50. Norton Plastics and Synthetics Division, Akron, OH 44383.

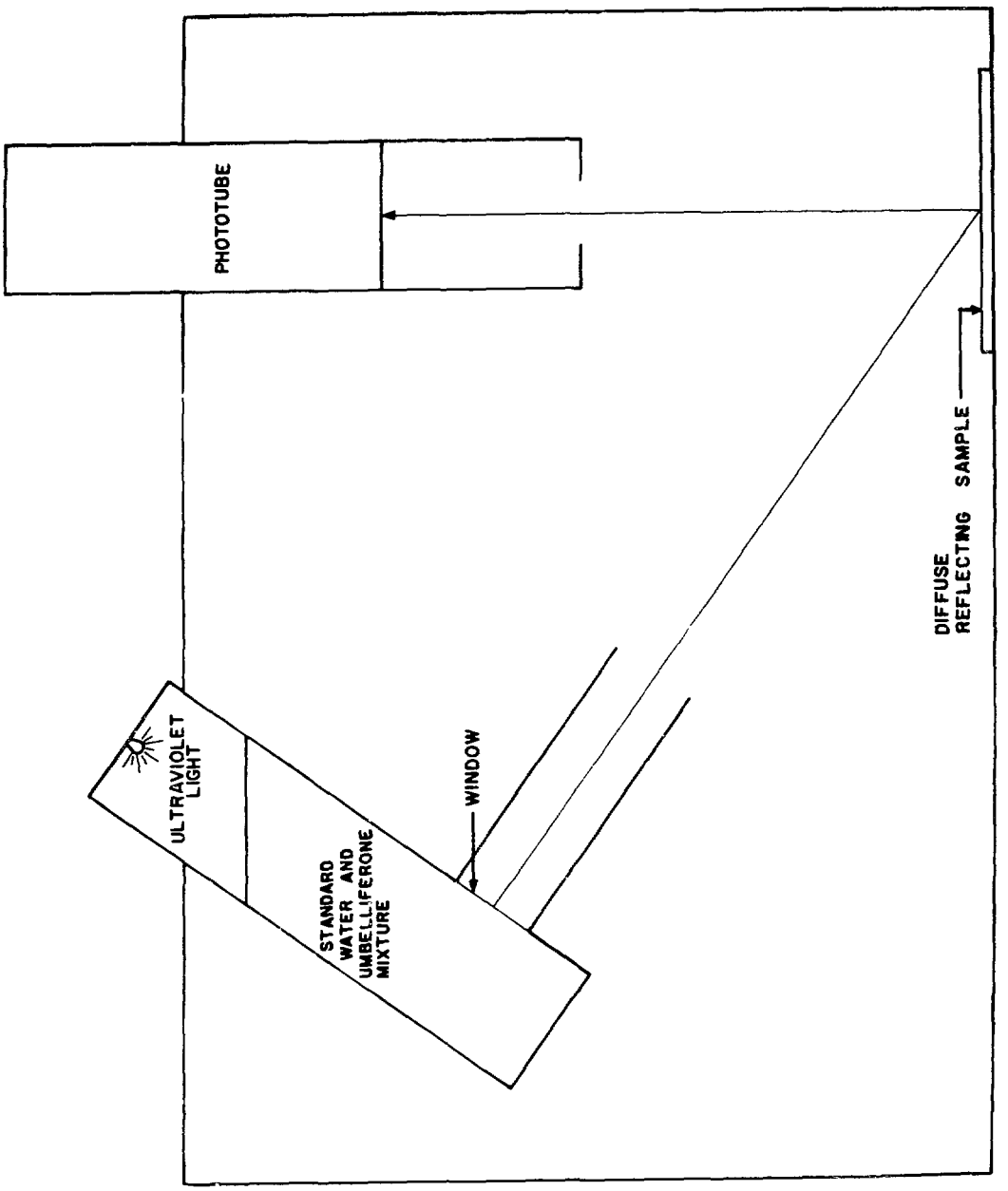

Fig. 7. Reflector test setup.

TABLE III

DIFFUSE REFLECTIVITY OF VARIOUS SAMPLES

Material	Reflectivity
Boric acid	100
Magnesium oxide	92
Teflon[51]	84
Kydex	82
ABS[52]	75
Crumpled aluminum foil	77
Black sample	<3

We always kept the upper manifold above the top of the counter, and kept a visible water level in it so we could be sure the counter was full.

In order to provide a light seal, and to trap any leaking water, the counter was wrapped in a Sears heavy-duty tarp.[53] The tarp had a slot cut in it at the level of the bottom of the counter, and a pipe attached to the slot for drainage in case of a leak. The tarp was tied to the top of the counter and laid as flat as possible, so as not to interfere with the positioning of the scintillators. A sheet of black plastic covered the top and sides of the counter, where the tarp did not reach. The counter was light-tight with these coverings, even before the scintillators were moved in place.

51. E. I. du Pont de Nemours and Company, Inc., 1007 Market St., Wilmington, DE 19898.

52. Cadillac Plastic, 823 Windsor St., Hartford, CT.

53. Catalog No. 6K75009L, Sears, Roebuck and Company, Sears Tower, Chicago, IL 60684.

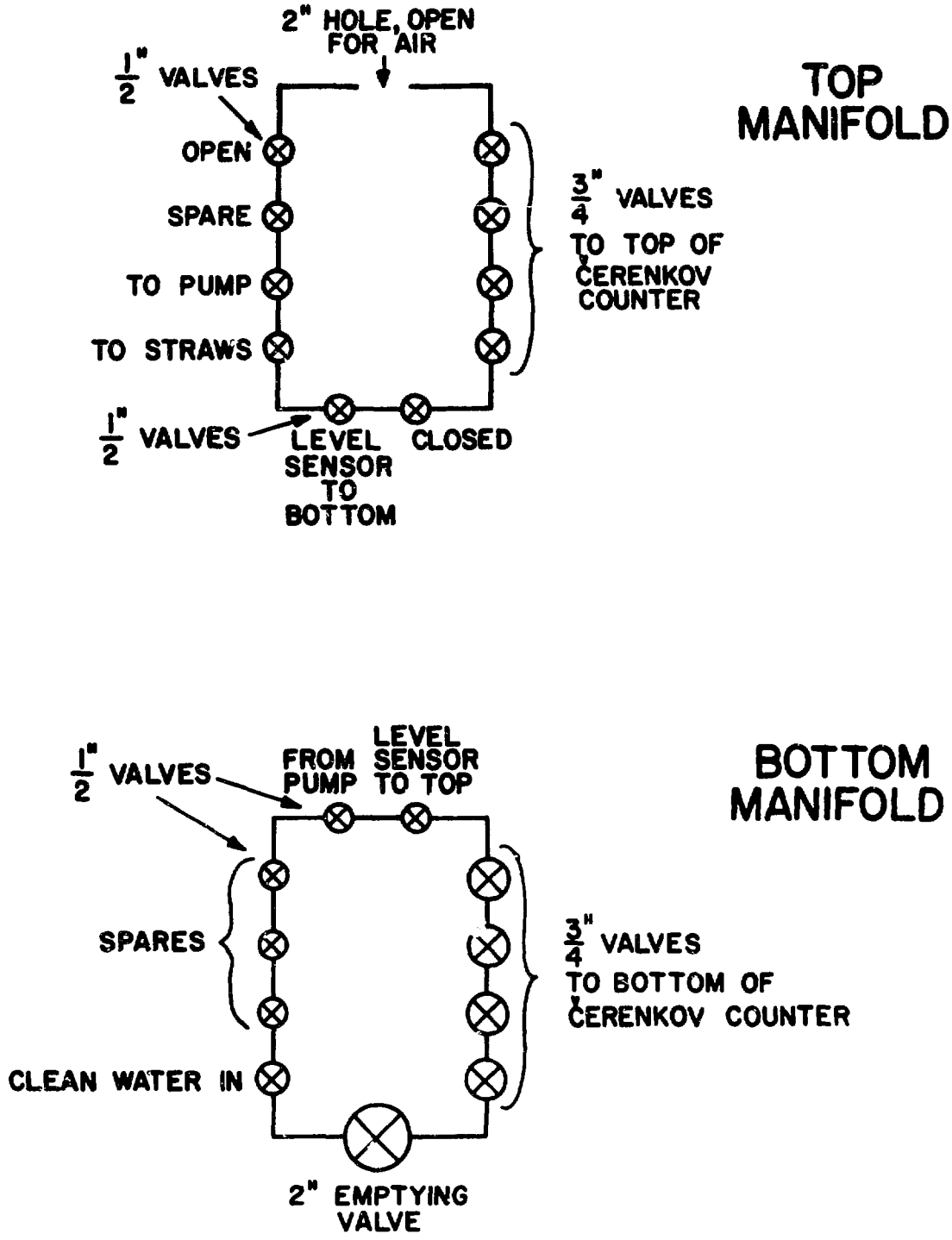

Fig. 8. Water manifolds.

The counter was filled with water, with occasional drainings, over a period of four and a half years, and with heavy water for five months. During this period, various weaknesses in the construction showed up, in the form of cracks and breaks. The main source of problems was the Benelex rib system. Under the hydrostatic load of 200 cm of water (0.2 atm), cracks began to develop in the struts. The first cracks appeared in the narrow struts where they crossed the wide ones, since the struts were notched in these places. Small aluminum L-bars were installed at these crossings, for reinforcement. Then the wide struts began cracking at the crossings, and both types began cracking at the corners. We then installed 1.6-mm-thick aluminum strips along the length of the wide struts, and also across the corners. The counter was in this condition for about one year, with no further strut problems. These splints did add about 100 kg of aluminum and steel to the material inside the anticoincidence shield; the effect of this material on the observed neutrino rates is discussed in the chapter on backgrounds.

Partly as a result of strut failure and partly from casting stresses around the porthole rings, cracks appeared in the epoxy walls themselves. These cracks were repaired from the outside of the counter, using fiberglass tape and epoxy patches. Fortunately, none of these cracks was serious enough to cause a major water leak. Leaks around the phototubes developed as the counter was filled and emptied; these were generally around the screws or O-rings, and were repaired as they developed.

Due to the relatively long path lengths involved in light transmission through the counter, we required a high degree of transparency of the water. Tap water was run through two ion-exchange resins[54] in series, and then through a particulate filter. The principle behind the operation of the ion-exchange resins is that they replace heavy positive ions in the water by H^+, and heavy negative ions by OH^-; these then combine to H_2O. Most impurities in water exist in ionic form. The resistivity was found to be more than 10^7 Ω cm. Measurements of throughgoing cosmic-ray muons indicated that transmission of light from one side of the counter to the other, an average distance of 150 cm, was 55%. This gave an absorption length (1/e) of 250 cm.

In order to maximize the number of photoelectrons emitted by the phototubes, we used a wavelength shifter in the water. We chose 4-methyl-umbelliferone, with an absorption peak at 360 nm and an emission peak at 450 nm.[55] This chemical will not fluouresce unless it is in a solution whose pH is at least 8.0. To achieve this, we used 87.5 mg/ℓ of ammonium phosphate $[(NH_4)_2HPO_4)]$ and 16.7 μℓ/ℓ of 58% ammonia solution ($NH_3 + H_2O$). This amount of additive had no effect on the transparency of the water. Figure 9 is a curve showing the gain of the counter, in arbitrary units, vs the umbelliferone concentration. We used 0.5 mg/ℓ as our standard concentration.

54. Culligan USA, 1 Culligan Parkway, Northbrook, IL 60062.

55. D. H. Leaback and P. G. Walker, Biochemical Jour. 78, 151 (1961); N. A. Porter, Nuovo Cimento 5, 526 (1957).

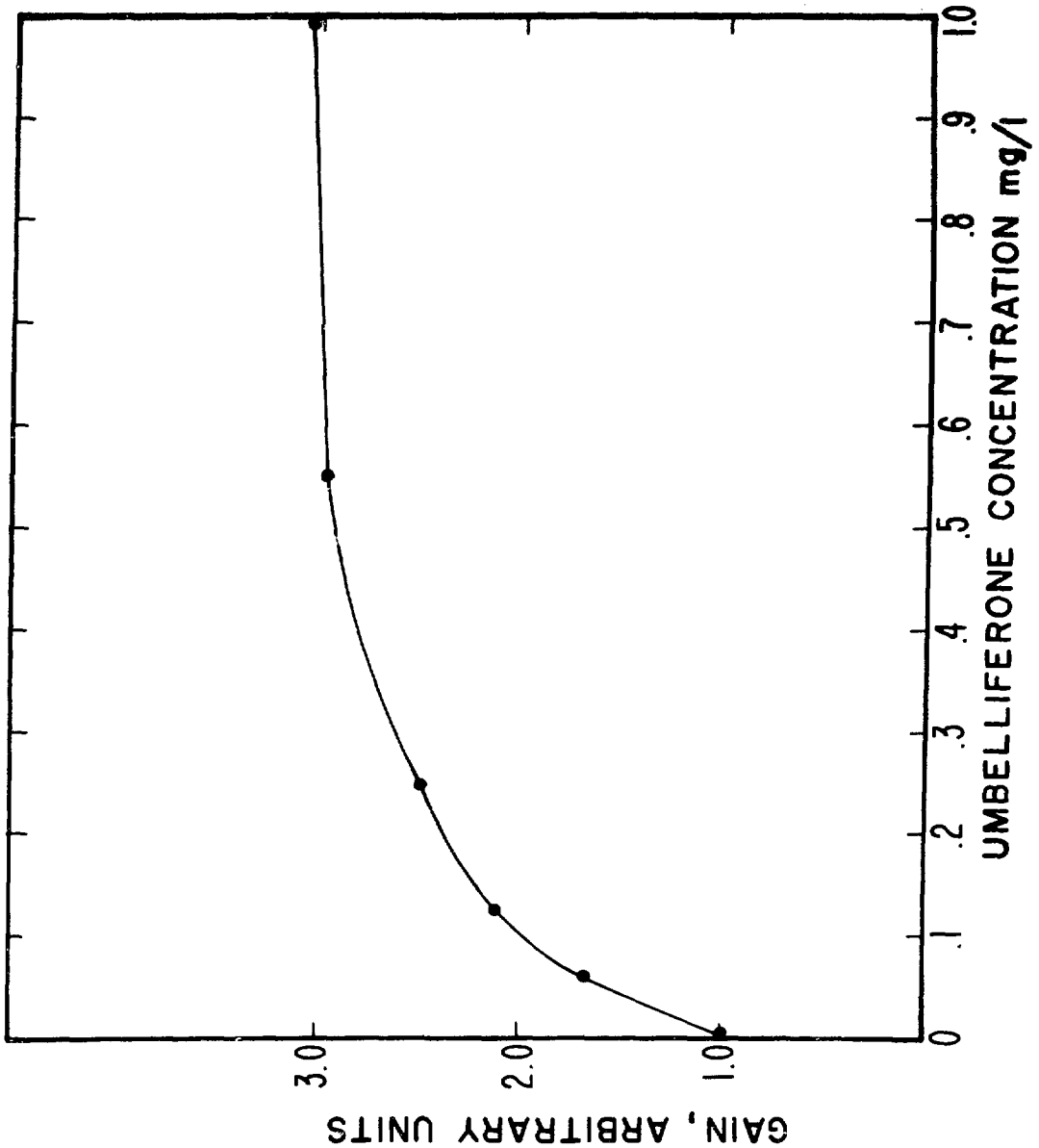

Fig. 9. Umbelliferone concentration curve.

During the months of June through September 1978, we ran the counter filled with D_2O, rather than H_2O. The heavy water was borrowed from Savannah River,[56] and we wanted to minimize the amount lost in transportation, storage, and use, so as to minimize the cost of replacing it. Because of the Cerenkov counter's long history of repairs, we decided we needed a passive recovery system in the case of any leak, and also an alarm system so positive action could be taken to reduce water loss in the event of a spill. A tank large enough to hold all the heavy water was installed in the hill south of the neutrino house, and a pipe installed connecting it to the outlet of the tarp enclosing the counter. Two water-sensitive detectors were placed in the pipe and connected to two alarms; in the presence of water, the detectors would close a circuit and set off the alarms. A level sensor was placed in the overflow bottle and set to close a circuit if the water level dropped more than 5 cm below its nominal level; this circuit was hooked up to one of the two alarms. The alarm with both the water-sensitive detector and the level sensor was placed in the electronics trailer; it sounded an audible alarm and also broadcast a tone on the frequency of a pocket pager, which we carried when we were not in the trailer. The second alarm was in the accelerator control room; it set off an audible alarm, and the accelerator operators had instructions to page a second pocket pager, which we also carried around, and also to announce over the public address system if the alarm had gone off. The 5-cm emptying hose from the bottom manifold was also connected to the outside tank, so we had the option of emptying the

---

56. E. I. du Pont de Nemours and Co., Savannah River Plant, Aiken, SC 29801.

counter if a leak occurred. Fortunately, no leaks did occur, and the alarm system never gave a false alarm. We purified the heavy water through a set of ion-exchange resins,[57] a carbon filter, and a particulate filter, as we were filling the counter. We used the same concentrations of umbelliferone, ammonium phosphate, and ammonia as we used in light water, and filtered the heavy water again on emptying to remove the chemicals we had added.

The phototubes we used on the Cerenkov counter were 12.5-cm EMI 9618R tubes.[58] The base circuit is shown in Fig. 10. The focus was adjusted individually for each tube; for the best focussing the rise time of the anode signal was 30 ns and the fall time 70 ns. The gain for high voltages around 1500 V was such that one photoelectron corresponded to a 4-mV pulse height into 50 Ω. We measured both the gain of each phototube and the relative quantum efficiency of its photocathode. To do this, we used two different light sources: an alpha source, ^{241}Am, mounted on a plastic scintillator, and a light-emitting diode. Both light sources were mounted in a mechanical device ensuring a well-defined position with respect to the phototube under measurement. The high voltage of each tube was adjusted to yield a given pulse height for the alpha source. The LED was then adjusted to give the same pulse height. Assuming that the width of the LED peak was essentially due to photostatistics, one could then find the average number of photoelectrons at the alpha peak:

57. Catalog No. COMB-012-04, Millipore Corp., Bedford, MA 07130.

58. EMI Gencom, 80 Express St., Plainview, NY 11803.

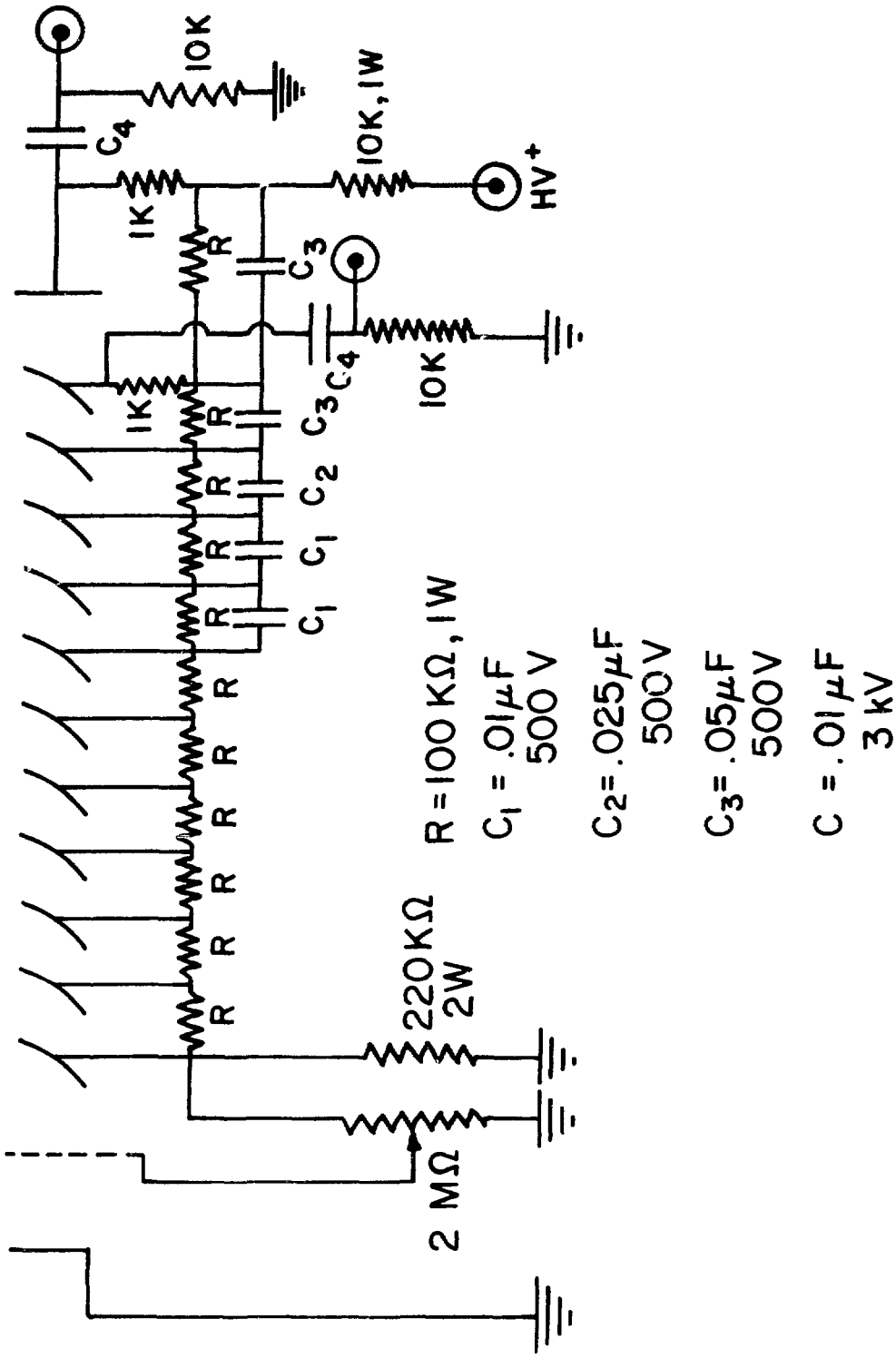

Fig. 10. Circuit diagram, EMI 9618R phototube base.

$$N_{pe} = 1/\sigma^2 \quad .$$

where σ = FWHM/2.3. Once this number is known, it was possible to calibrate the gain of the Cerenkov counter in photoelectrons/MeV. Table IV shows this gain for the 16 top tubes, the 16 bottom tubes, and the 96 tubes, as a function of reflector and wavelength shifter. The top/bottom ratio measured the isotropy of the light (these measurements were done with throughgoing vertical cosmic rays) and was increased, as expected, by adding the reflector and the wavelength shifter. The total number of 5.3 photoelectrons per MeV for the final setup gave a satisfactory resolution. Around 30 MeV the photostatistics were comparable to the edge effects and radiation losses. The Monte Carlo spectrum in Fig. 37 (see p.118) includes a resolution of 12%, as well as edge effects and radiation losses, which was found to be the best fit to the measured muon decay spectrum.

TABLE IV

GAIN OF THE CERENKOV COUNTER AS A FUNCTION OF REFLECTOR AND WAVELENGTH SHIFTER

Conditions		Photoelectrons/MeV		
Reflector	Shifter	Top	Bottom	Total
No	No	<0.1	0.6	1.1
Yes	No	0.3	0.7	1.8
Yes	Yes	1.1	1.5	5.3

B. SCINTILLATORS

The Cerenkov counter was surrounded on all six sides by a cosmic-ray anticoincidence shield, consisting of both active and passive elements. The innermost layer consisted of scintillators, overlapped so that particles could not get between them. The scintillators themselves were sheets of Pilot Y, manufactured by Nuclear Enterprises.[59] Each sheet was 2.5-cm thick, 60-cm wide, and 260-cm long. There were trapezoidal light pipes on each end, also 2.5-cm thick. Half of the scintillators had their light pipes mounted at a 90° angle to the scintillator; the other half were flat. A 12.5-cm-square, 1.3-cm-thick plastic plate was glued to the end of each lightpipe, and a 5-in.-diam phototube mounted on each plate. Figure 11 shows the scintillator sheets, lightpipes, and 90° bend prisms. Half of the bent scintillators had the longer 90° bend piece indicated.

The side scintillators were mounted on steel support stands which held them in position and also held the lead which was mounted outside them. The bottom scintillators sat on the table directly under the Cerenkov counter, and the top scintillators sat on the support struts on top of the counter. Figures 12 and 13 show the horizontal (bent; east and west sides) and vertical (flat; north and south sides) scintillators, their stands, and a partial view of the lead mounted behind them. Figure 14 is a top view showing how the stands fit together. The top lead did not rest on the top scintillators, but was placed in a framework which was supported at its corners by the side stands. There was a second layer of scintillators on the top, which was identical to the first layer, and which rested directly on the top lead.

59. Nuclear Enterprises, 935 Terminal Way, San Carlos, CA 94070.

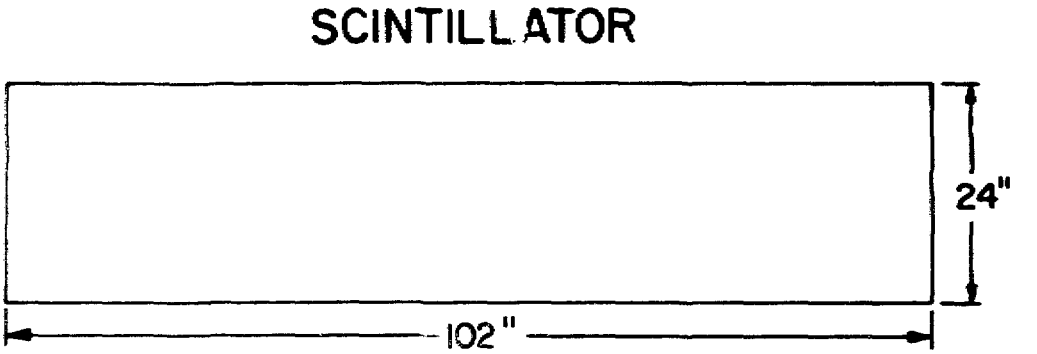

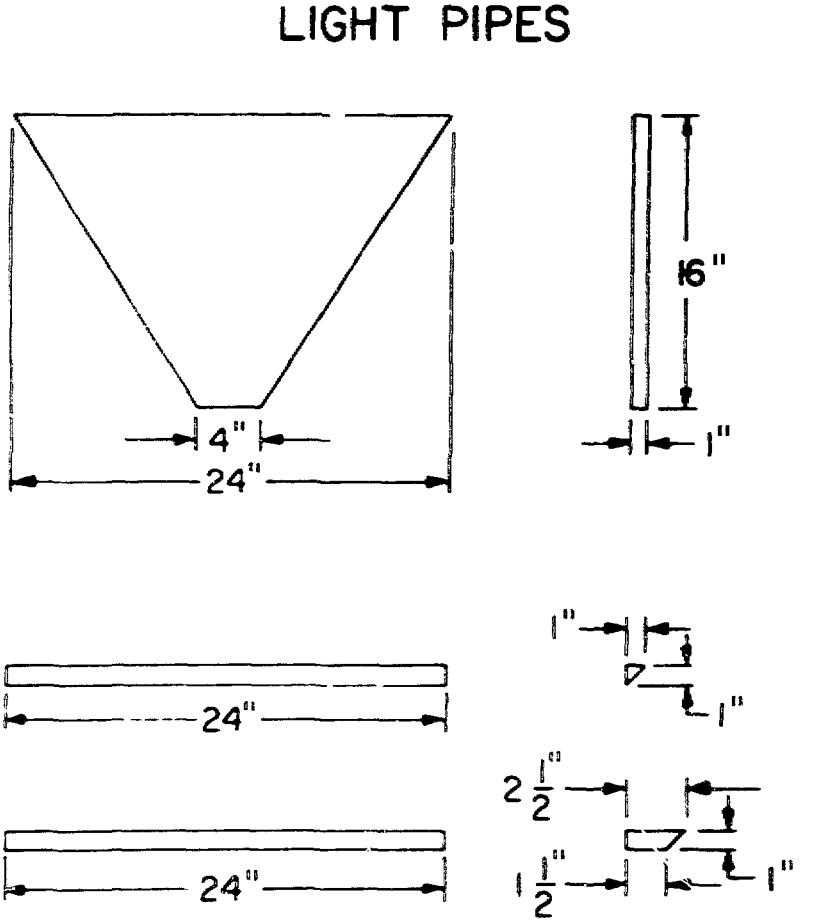

Fig. 11. Scintillator, light pipe, and 90° bend prisms.

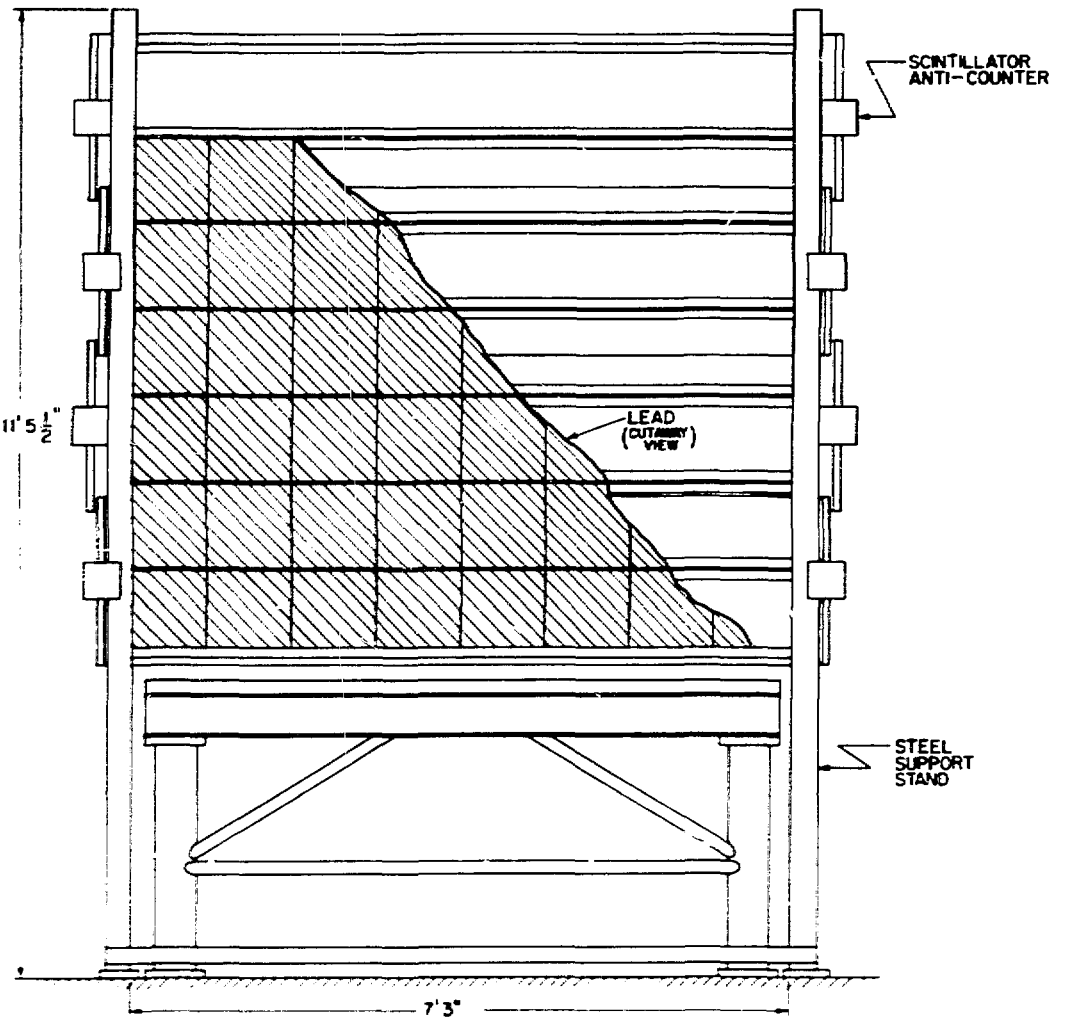

Fig. 12. Side scintillators, horizontal.

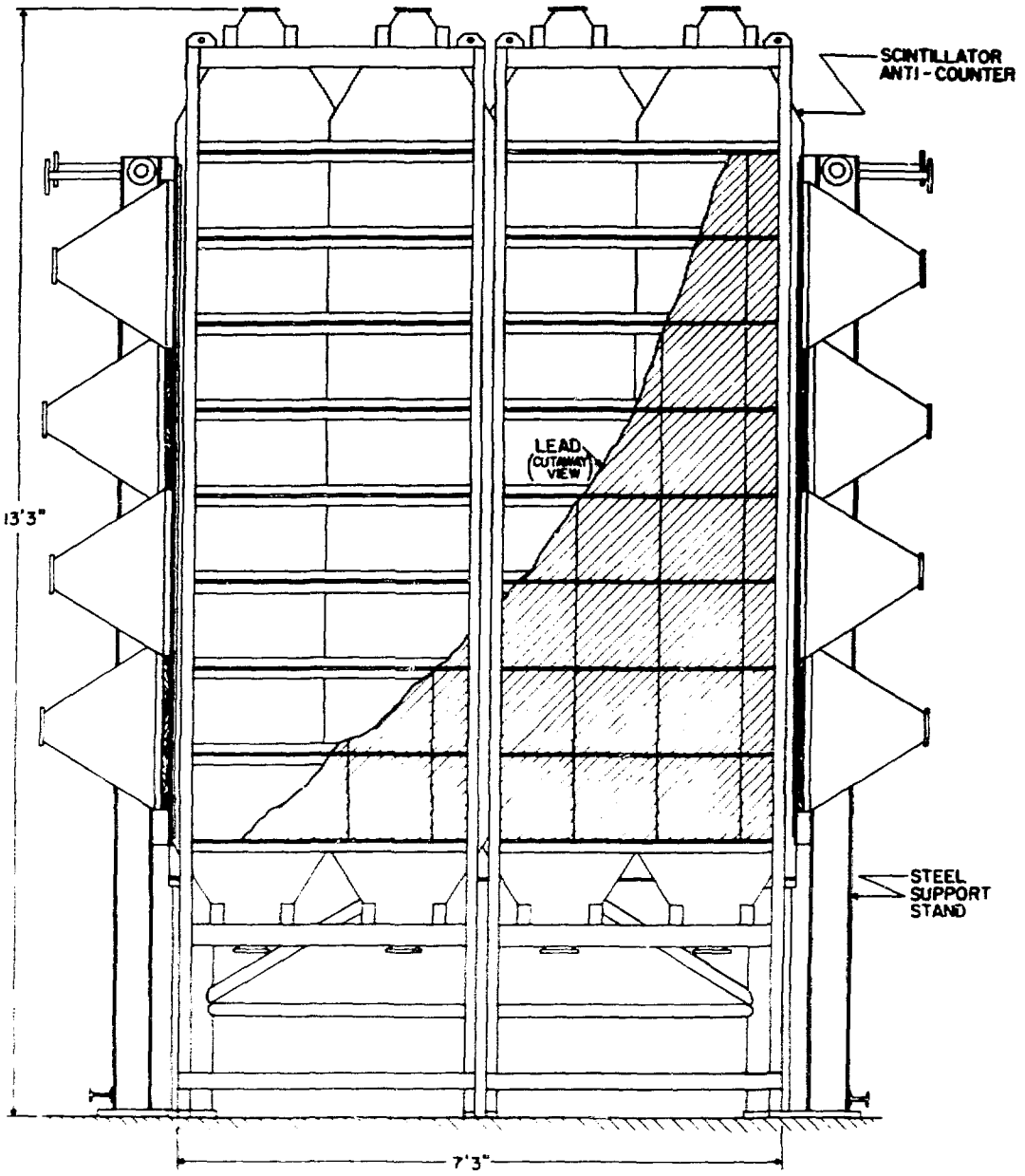

Fig. 13. Side scintillators, vertical.

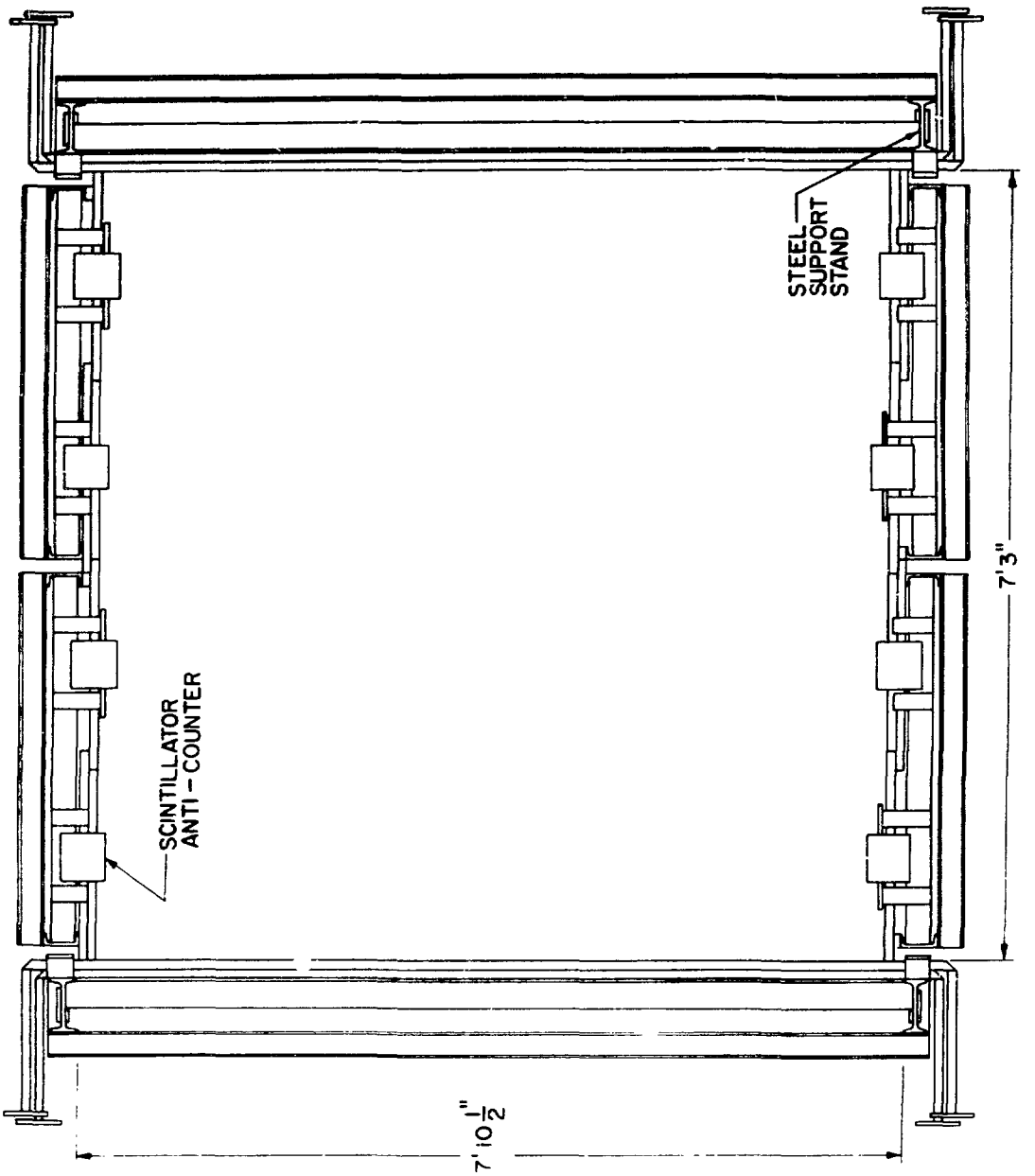

Fig. 14. Top view, scintillator stands.

Figure 15 shows the top scintillators and their position relative to the side scintillators. Table V lists each side of scintillators with its designation.

The phototubes used on the scintillators were RCA 4525, 12.5-cm tubes.[60] These tubes had only ten stages, and the signals needed amplification; an amplifier was therefore built into each base.[61] Figure 16 is a diagram of the base. The rest of the electronics for the scintillators is described in the electronics section. Each tube had an LED mounted on the lightpipe near it, which allowed for testing of all the tubes.

TABLE V

NOMENCLATURE OF SCINTILLATORS

A_1	Inner layer of top scintillators
A_2	North side
A_3	West side
A_4	South side
A_5	East side
A_6	Bottom
A_7	Second layer of top scintillators

60. Radio Corp. of America, Electro-Optics and Devices, New Holland Ave., Lancaster, PA 17604

61. Amplifier design by J. Studebaker, Los Alamos Scientific Laboratory report LA-5749-MS (1974).

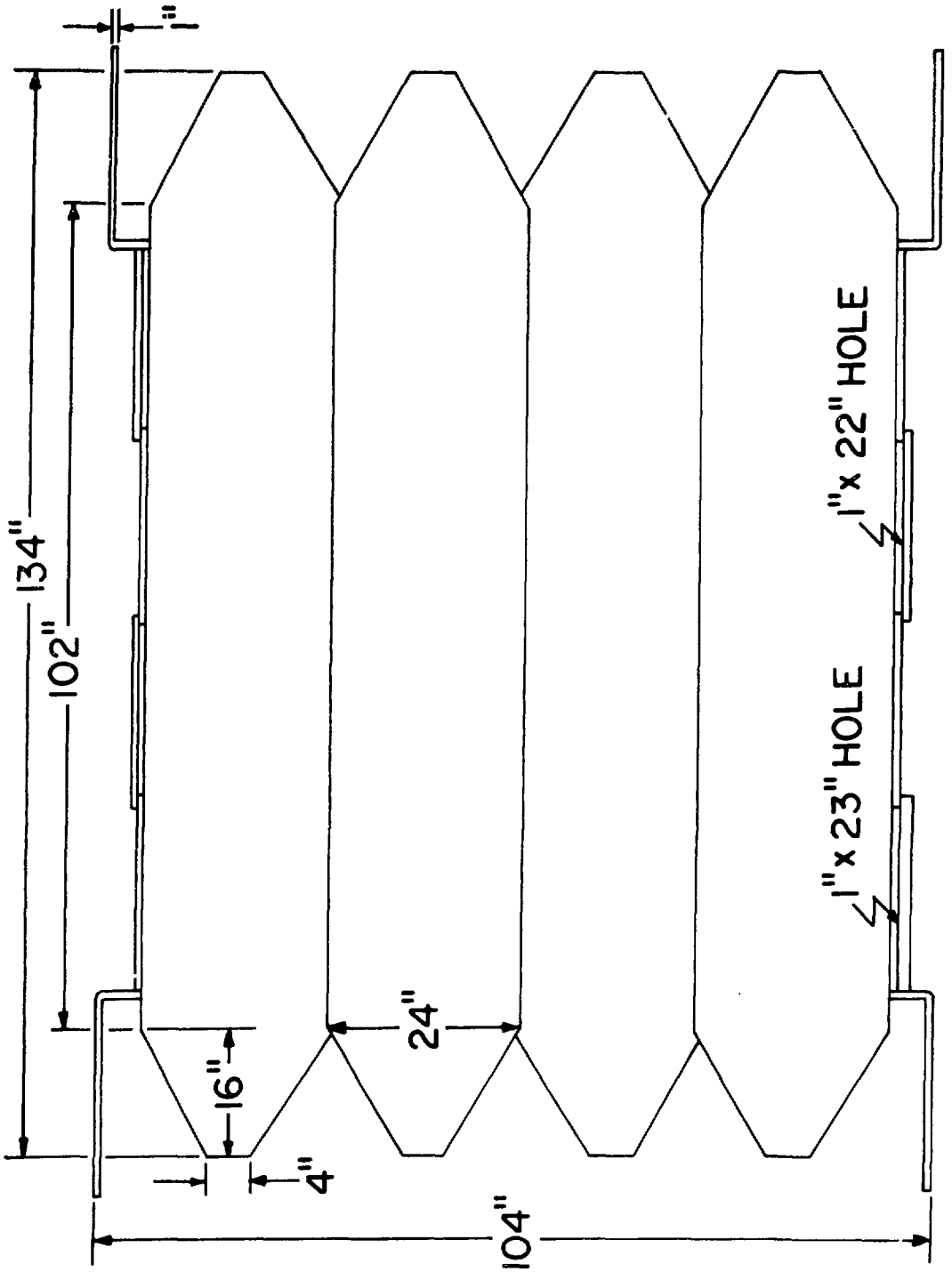

Fig. 15. Top scintillators.

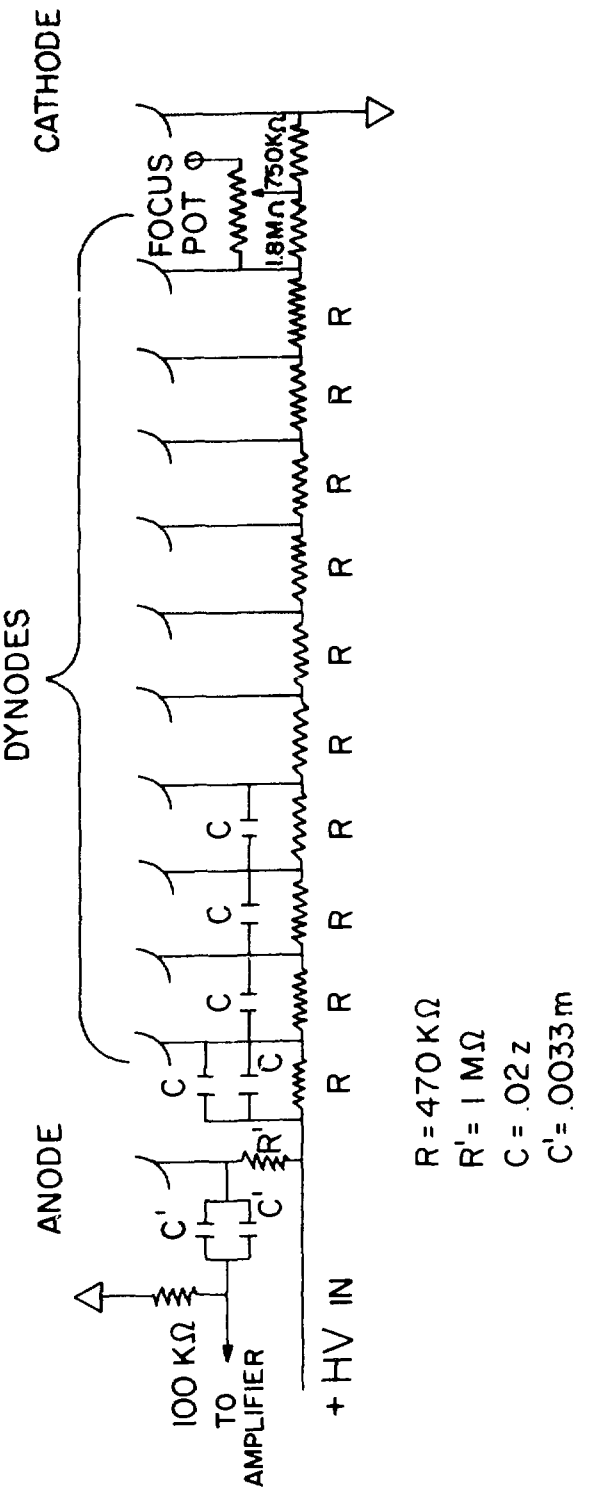

Fig. 16. Circuit diagram, RCA 4525 phototube base.

C. DRIFT CHAMBERS

The drift chambers were approximately 240-cm square, with two of the chambers slightly larger in one dimension. The larger ones were on the south and north sides, and the smaller ones on the east and west. The wire spacing in all chambers was 10 cm; the larger chambers had 25 wires, the smaller 24. The wires were 3.9-mil molybdenum with 6% gold bond. There were also field shaping wires between the sense wires. We ran with +4800 V on the sense wires and -1000 V on the field wires. The gas mixture was 80% methane and 20% argon, and we kept an output pressure of 6 mm of oil. Drift times were on the order of 1 μs; we were not sensitive to their exact magnitude.

The chambers were mounted on the north, east, and west sides directly outside the lead; the south chamber was at an angle, as described in the chapter on backgrounds. They were supported on brackets bolted to the scintillator stands. Figure 17 is an exploded diagram of the entire experimental setup with everything in place.

We measured the efficiency of the drift chambers using some small scintillators as a trigger, and found it to be at least 99%. The singles rates in each chamber, measured in the neutrino house with the beam off, were around 800/s. Unfortunately, we frequently had trouble with radioactive gas from the beam stop getting into the neutrino house. This affected the drift chambers most seriously, with rates as high as 50 K/s in a single chamber. Since we created an 11-μs anticoincidence pulse from the drift chamber output, these high rates led to enormous dead-time problems. We attempted to seal the neutrino house to keep the gas out, as described in the next section; we also made live-time cuts on the data, as described in the section on data analysis.

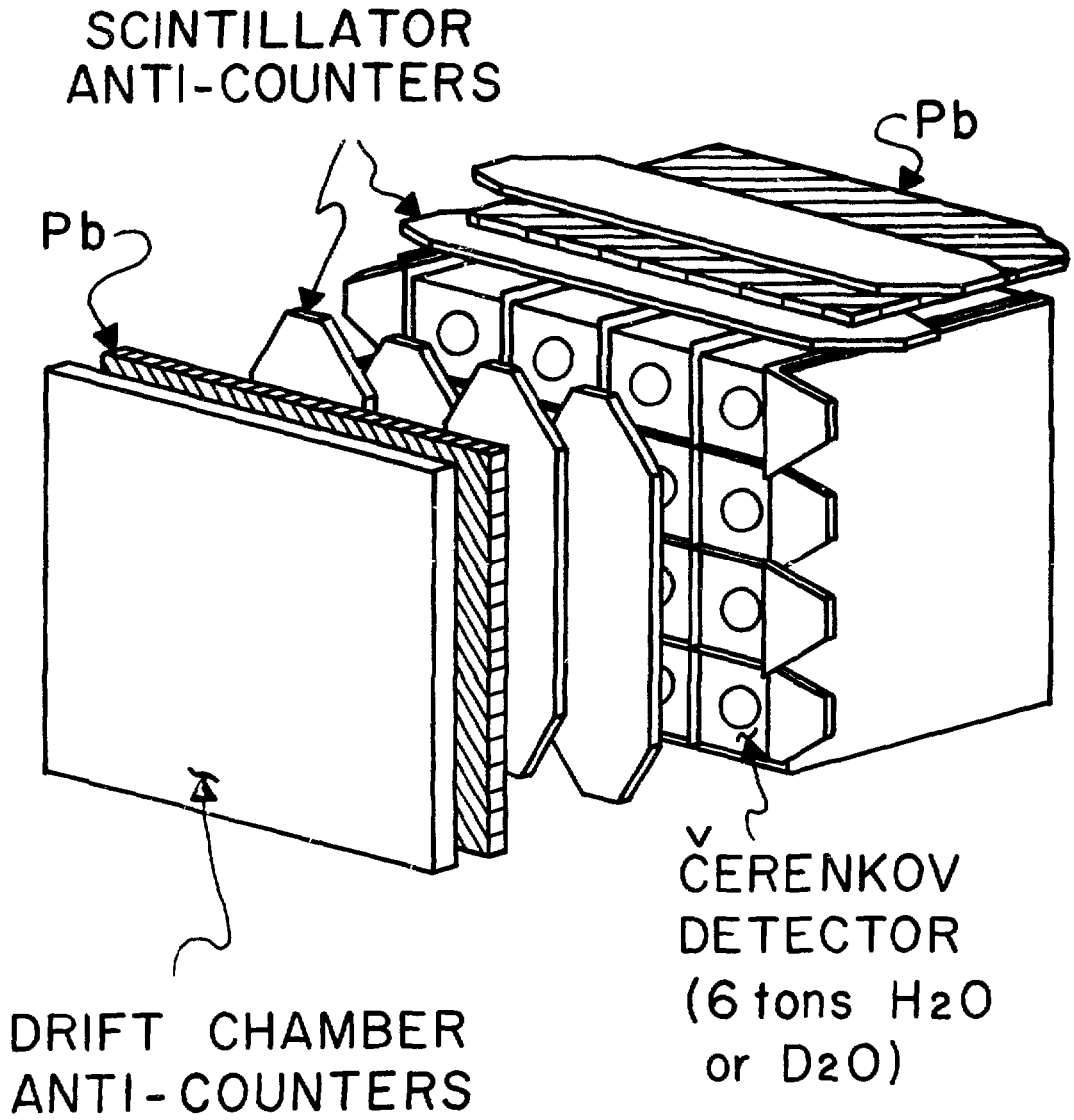

Fig. 17. Exploded view of experimental setup.

CHAPTER 3

THE LAMPF ACCELERATOR AND THE NEUTRINO HOUSE

A. THE LAMPF ACCELERATOR

Figure 18 shows the LAMPF experimental areas, including the neutrino area. LAMPF is an 800-MeV linear proton accelerator, with a design intensity of 1 mA of H^+; H^- ions are also accelerated simultaneously at a much lower intensity. The macroscopic duty factor is 6%; this consists of a 500-μs macropulse at 120 cycles per second. Higher duty cycles are also possible, and are achieved by lengthening the macropulses. The highest duty cycle we ran at was 7.5%, although plans are to go as high as 12%. The switchyard at the end of the accelerator provides beam to the four main beam lines: Line A gets most of the H^+ beam; Lines B and C use H^-; Line D uses part of the H^+ beam, either an entire macropulse (1 in 10, 1 in 12, and 1 in 120 are common) or the first portion ("front porch") of each macropulse. There are four production targets in Line A: a thin target used for irradiation and nuclear-chemistry studies; Target A-1, 3-cm carbon, which provides pion beams for the Low-Energy Pion channel (LEP) and the Energetic Pion Channel and Spectrometer (EPICS); Target A-2, 5-cm carbon, which provides a high-energy pion beam for the pion and particle physics channel (P^3) and a muon beam for the Stopped Muon Channel (SMC); and Target A-5, 8-cm carbon, which provides a pion beam used for biomedical research. Targets A-1 and A-2 are in the beam continuously (unless there is some problem); the biomedical channel, however, has no beam

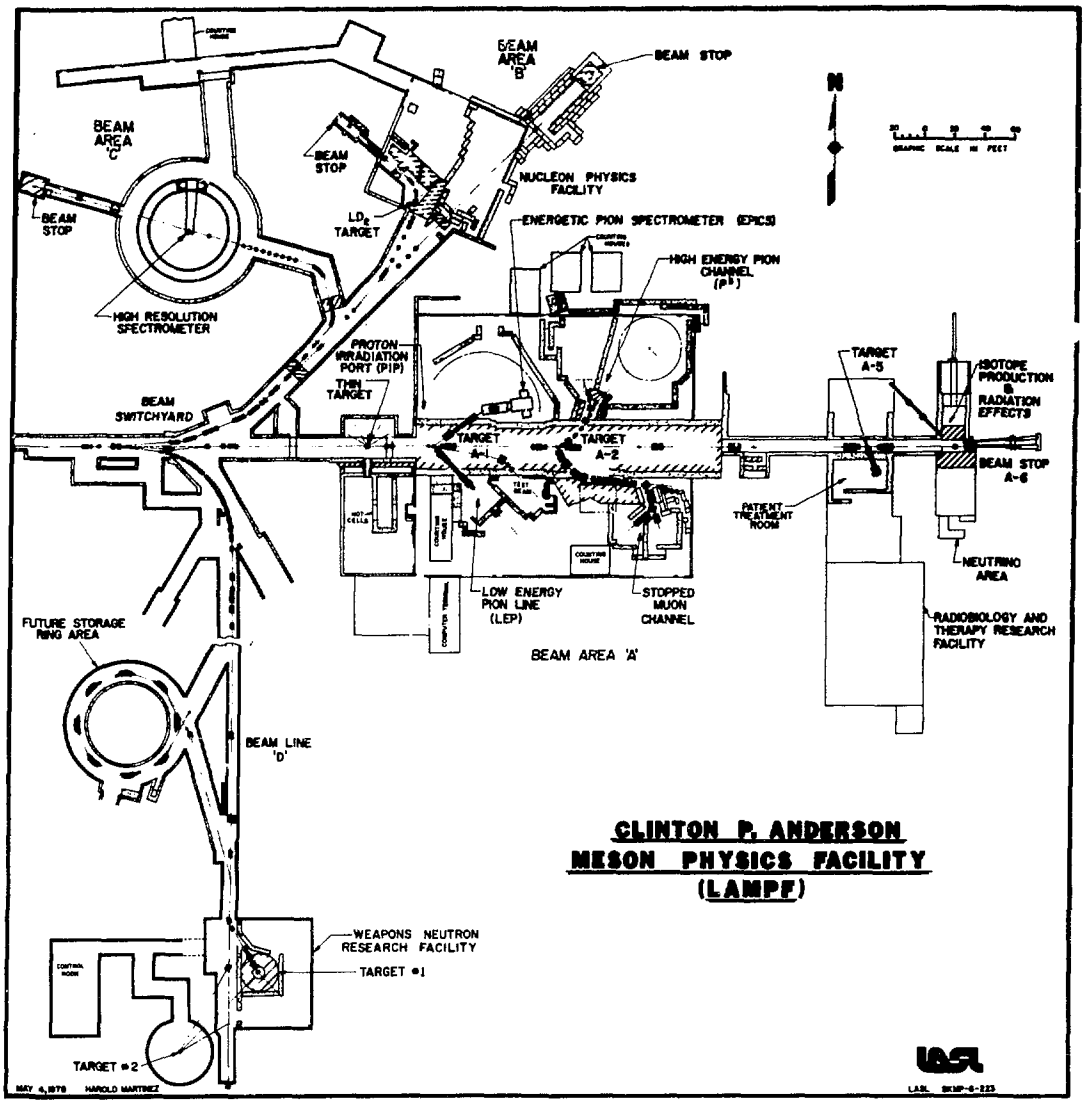

Fig. 18. LAMPF Experimental Area.

plug, and the target must therefore be removed from the beam when access to the channel is desired. This target was out of the beam about half the time during all the time that we were taking data.

The beam stop is copper and is water-cooled. It is a cylinder 8 in. in diameter and 50-in. long. The isotope production experiments used targets placed directly in front of the beam stop, and much of our neutrino flux came from these targets rather than from the beam stop itself. The target holders, which were thicker than the targets themselves, were steel; each target plus holder was 4-cm thick. There were usually four of these targets in place.

The beam position and intensity are monitored by a series of wire profile monitors[62] and toroidal current monitors.[63] The profile monitors are multiwire counters placed in the beam; the secondary emission is monitored to give a profile of the beam. The toroids function as current transformers, the proton beam acting as a single-turn primary winding. They provide both analog and digital outputs of the beam intensity. We used the analog output as part of our triggering system, so we took data only when the beam was on. The digital output is proportional to the beam intensity in each macropulse; we scaled it as a measure of the total beam incident on the beam stop. A calibration pulse is provided continuously for calibrating the number of pulses per coulomb. This calibration was normally changed only when the beam intensity changed (a history of the beam intensity is contained in the

62. E. W. Hoffman et al., Los Alamos Scientific Laboratory report LA-UR-79747 (1979).

63. Paul J. Tallerico, J. Vac. Sci. Technol., 12, 1200 (1975).

final chapter); we checked the calibration weekly, and also when we had been notified of a change.

B. THE NEUTRINO HOUSE

The neutrino house itself was opposite the beam stop, at 90° to the beam direction. This minimized neutron-induced high energy photon events, since high-energy neutrons produced in the beam stop tended to go forward. There was 6.3 m of steel shielding in the direction of the beam stop (see the secton on backgrounds for the reason for this choice). The last 2.3 m were not installed until after some background measurements had been made. Figure 19 shows the neutrino house and associated shielding, and also the location of our detector. There was, at the reduced shielding levels, a movable plug of shielding next to the beam stop; this plug was removed to yield a different shielding configuration quickly. The data taken with this plug removed proved difficult to interpret because the fluxes were very sensitive to the position of the beam stop (it could be moved about 60 cm along the beam direction). Because of this ambiguity of interpretation, the plug was removed and replaced with solid shielding after the fifth meter of steel had been installed. The east and west sides and the roof of the neutrino house were built of missile silo door counterweights, which were slabs of cast iron 6.1 m by 1 m by 30 cm. The roof consisted of four layers of counterweights. The south wall was concrete with a stack of counterweights behind it. The floor was of concrete blocks.

Because of the problem with radioactive gas mentioned above (in the section on the drift chambers), we attempted to completely seal the house, to keep the gas out (this was not done, however, until March 1979). We then worried about a buildup of methane from the drift

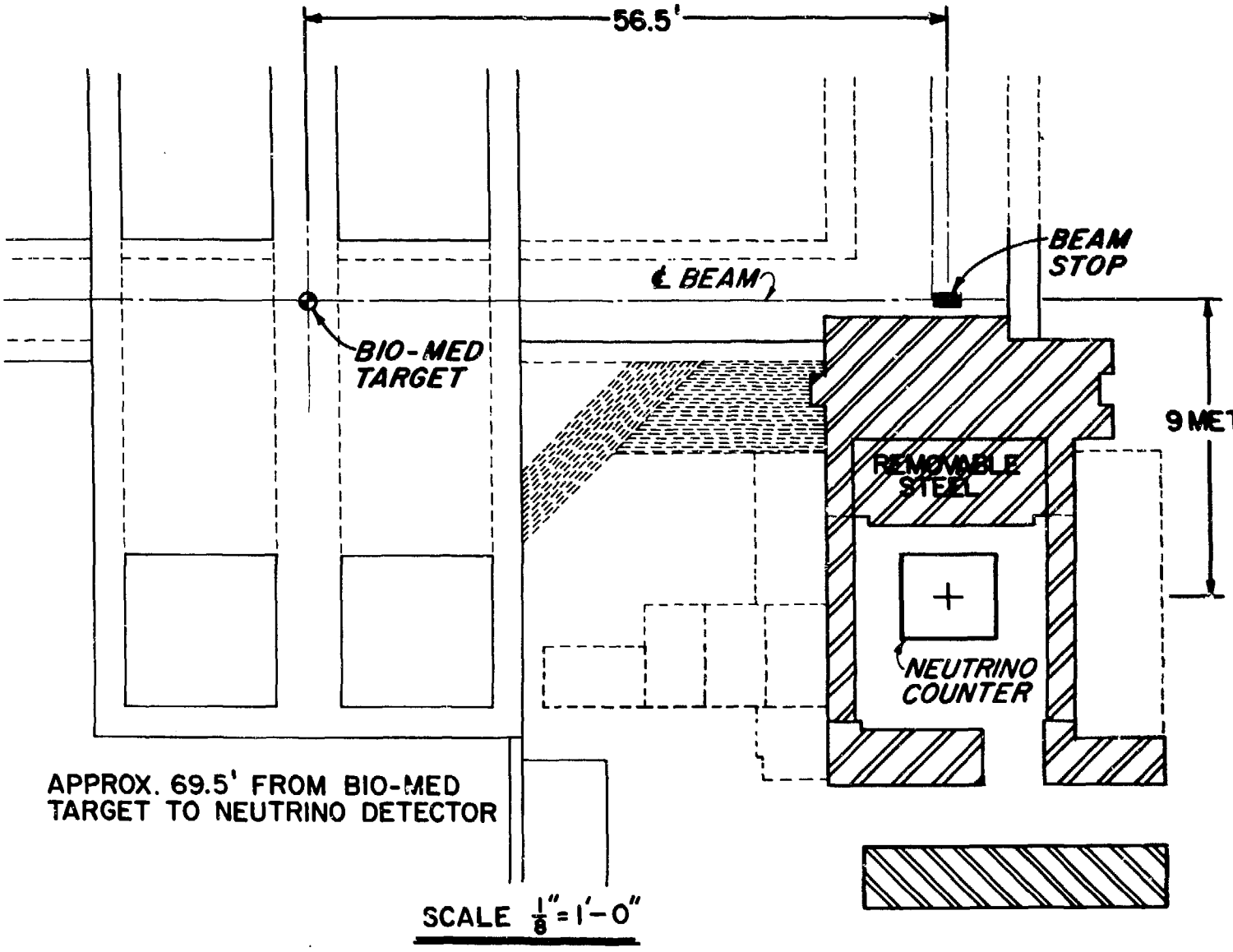

Fig. 19. Neutrino House Area.

chamber exhaust, possibly leading to an explosive mixture. An exhaust system was installed to permit personnel access when necessary. It turned out, however, that the sealing was not tight, and methane buildup was not a problem.

CHAPTER 4

BACKGROUNDS

There were two fundamentally different types of backgrounds for this experiment -- those which were beam--associated, and those which were not. Non-beam-associated backgrounds were the same whether the beam was on or not; they could therefore be measured between beam spills and subtracted. A low signal-to-noise ratio was tolerable with this type of background. Beam-induced backgrounds, on the other hand, could not be subtracted directly and attempts were therefore made to reduce these events to as small a fraction of the expected neutrino signal as possible. The choice of a Cerenkov counter for the detector was made partly to reduce the backgrounds. The counter was not sensitive to recoil protons, as a scintillator or bubble chamber would have been.

A. NON-BEAM-ASSOCIATED BACKGROUNDS

The background events which were not associated with the beam came primarily from cosmic rays, although tube noise also made a small contribution. The cosmic-ray anticoincidence shield was designed for the most efficient rejection of these events. Cosmic-ray-induced events in the energy range of (20,60) MeV were of the following types: charged events, including delayed electrons from muon decay; gammas from muon bremsstrahlung; and gammas from muon decay with electron bremsstrahlung. We chose the energy region (20,60) MeV because this corresponded closely

to the region over which we intended to analyze our data for actual neutrino-induced events. These events occur from 0 to 60 MeV, but the backgrounds were too high at the lower energies for those data to be useful, and the neutrino spectrum fell off there anyway.

Charged events were vetoed primarily by the inner layer of scintillators. The total charged cosmic-ray rate in the (20,60) MeV window was 2.9×10^5/Los Alamos day (6% of a 24-hour day, or 5184 seconds). Of these, 1.0×10^5 were muon decays. Using the entire scintillator system with a 25-μs veto pulse, the residual rate in (20,60) MeV was 2500 ± 40/LAday, a reduction of a factor of 100. Most of these remaining events were true neutrals, rather than charged events missed by the scintillators, charged particles going through holes, or muon decays occuring after the gate. The inefficiency of the scintillator shield was monitored on-line using a coincidence between the bottom layer of scintillators (A_6) and a high-threshold (100-MeV) signal in the Cerenkov counter (C_H). This provided a pure throughgoing muon trigger. An "or" of the other five sides of scintillators (A_1,A_2,A_3,A_4,A_5) was then put in anticoincidence with $A_6 \cdot C_H$. This inefficiency was usually near 2×10^{-4}. The 25-μs length of the veto pulse corresponded to 11.4 muon lifetimes, which gave a reduction in the number of mu-decay electrons of a factor of 10^5. The inefficiency would therefore yield 20 events/LAday, assuming that we were measuring a real inefficiency and not a trigger inefficiency, and the gate would miss one mu-decay event/LAday.

There were also some small holes in the scintillator shield, due to the way the scintillators were stacked (see Fig. 15). The contribution to the neutrals rate in (20,60) MeV was measured by placing two small scintillators over one of the holes, making a coincidence between them, and asking how many of the neutrals came in coincidence with that signal. The result was that 20 events/LAday will come through those four holes on the top. There were similar holes on the sides, but the contribution from those was assumed to be negligible because the rate of near-horizontal cosmic rays is small compared to the vertical.

There were two types of cosmic-ray-induced neutral events which caused background events in the Cerenkov counter -- gammas from muon bremsstrahlung in the roof, and gammas from muon decay in the last section of the roof with electron bremsstrahlung. These two processes were independent and required different solutions; they will therefore be dealt with separately.

If the separation between the roof and the scintillator shield were large enough, a muon and a wide-angle bremsstrahlung gamma could become widely enough separated so the gamma entered the Cerenkov counter but the muon completely missed the scintillators (see Fig. 20). The gamma would then convert in the water and cause a neutral event. The solution to this problem was to effectively bring the roof very close to the counter, which was done by installing lead directly outside the scintillators (see Fig. 13). The desired thickness of lead was measured by first installing 1.8 cm of lead on the sides and then measuring the effect on the neutrals rate of no lead, 1.8 cm of lead, and 3.7 cm of lead on the top. From these measurements, we concluded that the attenuation length of gammas in lead is 10.8 g/cm^2 (±5%), and that the

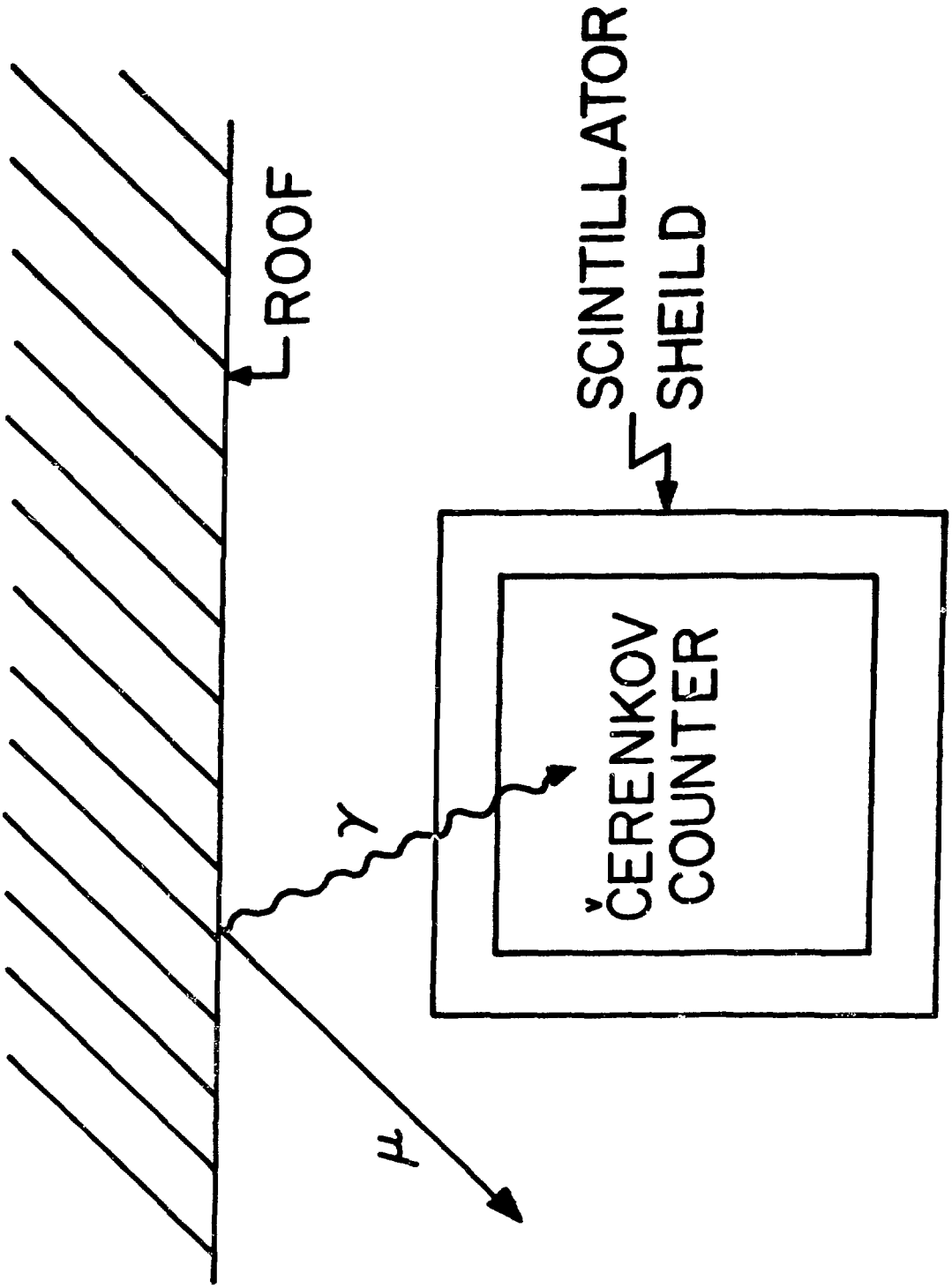

Fig. 20. Muon bremsstrahlung.

3.7 cm of lead reduced the neutrals events coming from muon bremsstrahlung through the top of the counter by a factor of 50. The muon bremsstrahlung rate through the top was 20/LAday with 3.7 cm of lead. Subsequently, another 1.2 cm of lead was installed on the sides of the counter, making a total of 3.0 cm on the sides. The rate of neutrals in (20,60) MeV with this amount of lead was 650 events/LAday.

The other major contribution to the cosmic ray-associated neutral events came from muons which stopped in the lead, decayed, and gave a bremsstrahlung gamma from the decay electron (see Fig. 21). Even if the electron did not escape from the lead to produce a pulse in the scintillators, the gamma could go into the counter and convert, causing a neutral event. Many of these events were eliminated by installing detectors outside the lead, which detected the muon as it entered the lead and thus provided a veto. We used scintillators on the top and drift chambers on the sides (see Fig. 17). We did not use timing or position information from the drift chambers, but simply treated them as if they were scintillators. With a 25-μs veto pulse for the scintillators and 11 μs for the drift chambers, the rate of neutrals in (20,60) MeV was 450 events/LAday. This was less of an effect than we had hoped for, and we decided that most of the residual events could still be of the muon bremsstrahlung type. The Cerenkov counter was quite close to the north, west, and east walls of the neutrino house, but it was not so close to the south wall (see Fig. 19). We decided to try raising the south drift chamber at an angle -- it would still catch muons entering the lead, since they were mostly vertical, but it would also catch more wide-angle muons which might be associated with bremsstrahlung gammas in the counter (see Fig. 22). With the south

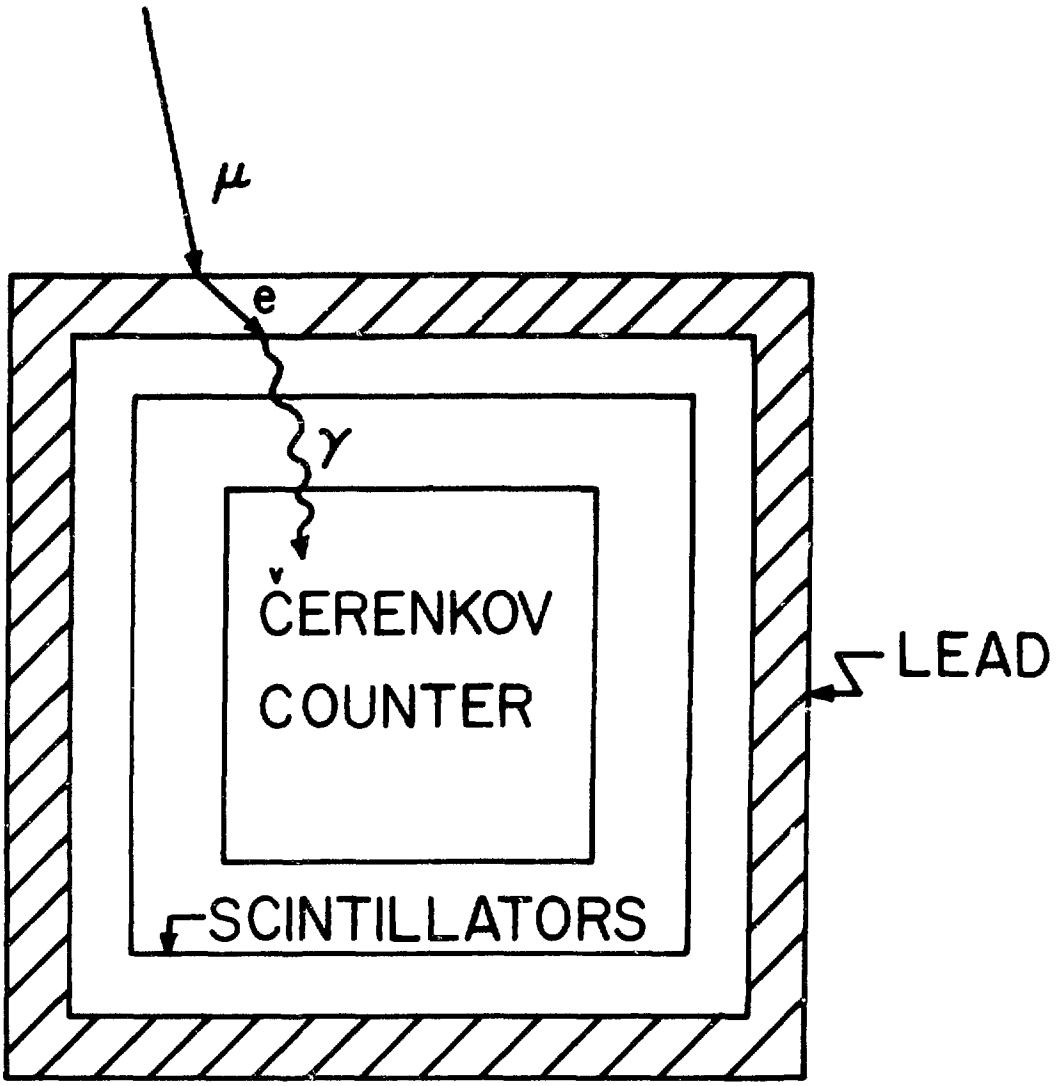

Fig. 21. Muon decay with electron bremsstrahlung.

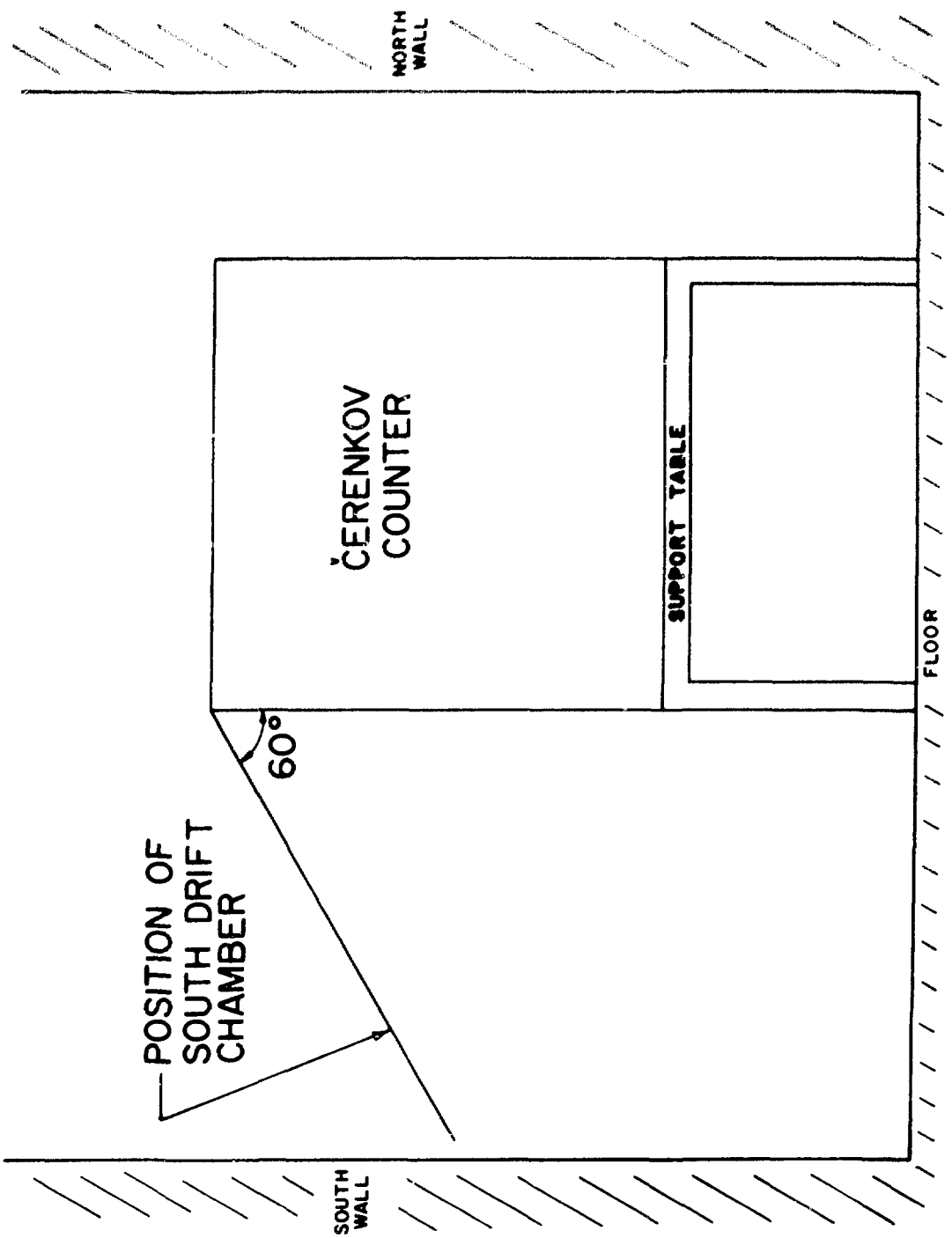

Fig. 22. Position of south drift chamber.

drift chamber in this position, the neutrals rate was 325/LAday, indicating that our guess about wide-angle muons was correct. We left the chamber in this position for all further running. Figure 23 shows the spectrum shape of the cosmic-ray events with no anti, the short anti, the long anti with scintillators only, and the total anti. All rates are per Los Alamos day.

A check was made to see that all of our neutrals events were muon-associated. For a short time, an extra foot of steel was added to the roof of the neutrino house. The ratio of the total cosmic-ray flux in the counter with the thicker roof vs the normal roof was 0.926, whereas the ratio of neutral events was 0.913 ± 0.012. From this we concluded that there was no evidence for a component of the neutrals events with an attenuation in steel different from that of the muons. Cosmic rays do have both electronic and hadronic components as well as the muonic; our roof eliminated the electronic part. The Cerenkov counter was not sensitive to nucleons, except those at very high energy; this was the component that the above test would have shown if it were present, since nucleons would attenuate in the steel much faster than the muons.

Tube noise could also look like a neutral event, since it would not be associated with a signal in the anticoincidence shield. One way to get an idea of whether this was a problem was to reduce the intrinsic gain of the counter, so the tube noise corresponded to a higher energy, and see if the neutrals rate increased. This was done by looking at the counter after it had just been filled, before the wavelength shifter was added. The gain was low by a factor of 2.6 compared to later, when the wavelength shifter had just been added. We looked in (30,60) MeV, and

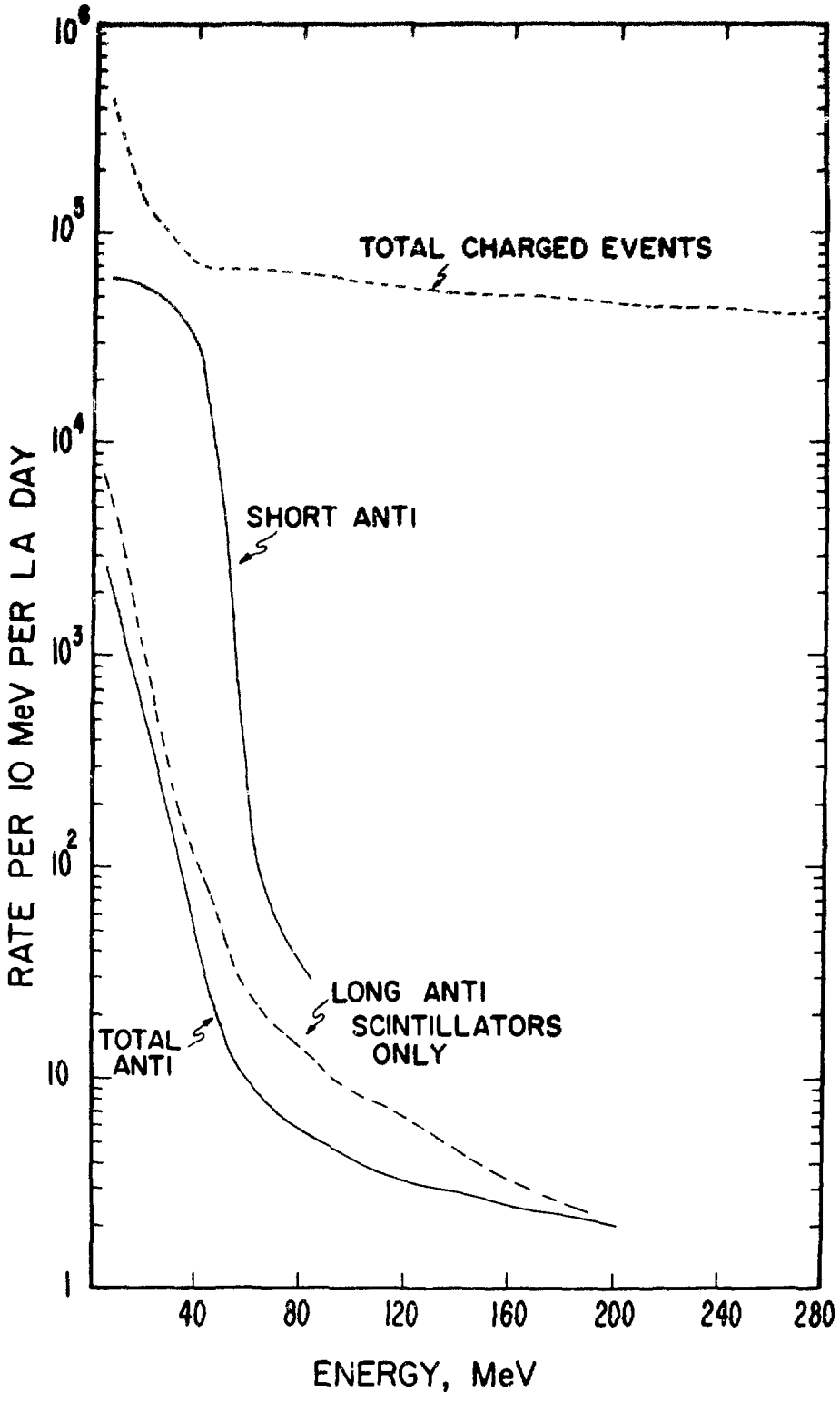

Fig. 23. Spectrum shape of cosmic-ray backgrounds.

found, with no wavelength shifter, that the neutrals rate was 325/LAday. After the wavelength shifter was added and the gain readjusted, the neutrals rate in (30,60) MeV was 100/LAday. We were, therefore, not far from the tube noise and indeed might still have a contribution to it even at the higher gain. Certainly if the gain of the counter dropped because of clouding of the water, for instance, the tube noise contribution would increase.

Backgrounds with the D_2O fill of the counter were measured only with the full anti system in place and operational. They were the same as the H_2O fills, 350 events/LAday in (20,60) MeV. This rate, through all our running, fluctuated by about 25%, which we assumed was due to fluctuations in the primary cosmic-ray flux, changes in tube noise, and minor electronics problems.

B. BEAM-ASSOCIATED BACKGROUNDS

Beam-associated backgrounds in the Cerenkov counter were of several types. In principle, these were more insidious than non-beam-associated backgrounds, since they could not be subtracted on line. Thermal neutrons, which gave capture gamma rays, were numerous but low in energy; they got into the energy region which was interesting for neutrinos only through resolution and pileup effects. They could also contribute to the dead time of the anticoincidence shield. High-energy beam-associated neutral events have also been seen in the counter. These were probably due to neutral pions created by high-energy neutrons; the pion decay would produce two high-energy gammas, which could convert in the counter. These backgrounds were measured by running at a series of different shielding conditions, and the final

shielding configuration was planned to reduce them to a level small compared to our expected sensitivity. The thick (8-cm-graphite) biomedical target just upstream of the beam stop created large amounts of background when it was in the beam. The shielding in that direction was made as thick as possible, but there was still a considerable increase in background compared to when that target was out. There was also undoubtedly an increased electron antineutrino flux due to negative-pion decay in flight downstream of that target, but that should have been a small effect because of the small solid angle. There was also material other than hydrogen inside our scintillator shield; another source of background was from reactions of electron neutrinos from normal muon decay on these other materials, principally carbon and oxygen. Differential shielding measurements were not done on D_2O, but the total beam-associated rate at low energies (where the thermal neutrons predominate) was measured and compared to the H_2O data.

The fall-off of thermal neutron events in the Cerenkov counter was planned to be 10^7 from 0 to 20 MeV. Figures 24 and 25 show this to have been true for both biomed target in and out, although the absolute rate was higher by about a factor of 35 for biomed target in (see Table VI). The assumption here was that all the low-energy events in the subtracted spectrum were thermal neutrons. Figures 26 and 27 show the measured thermal neutron flux, assuming a continued exponential falloff, and the predicted neutrino spectrum for R = 1.0. From this we see that above 25 MeV the thermal neutrons did not contribute.

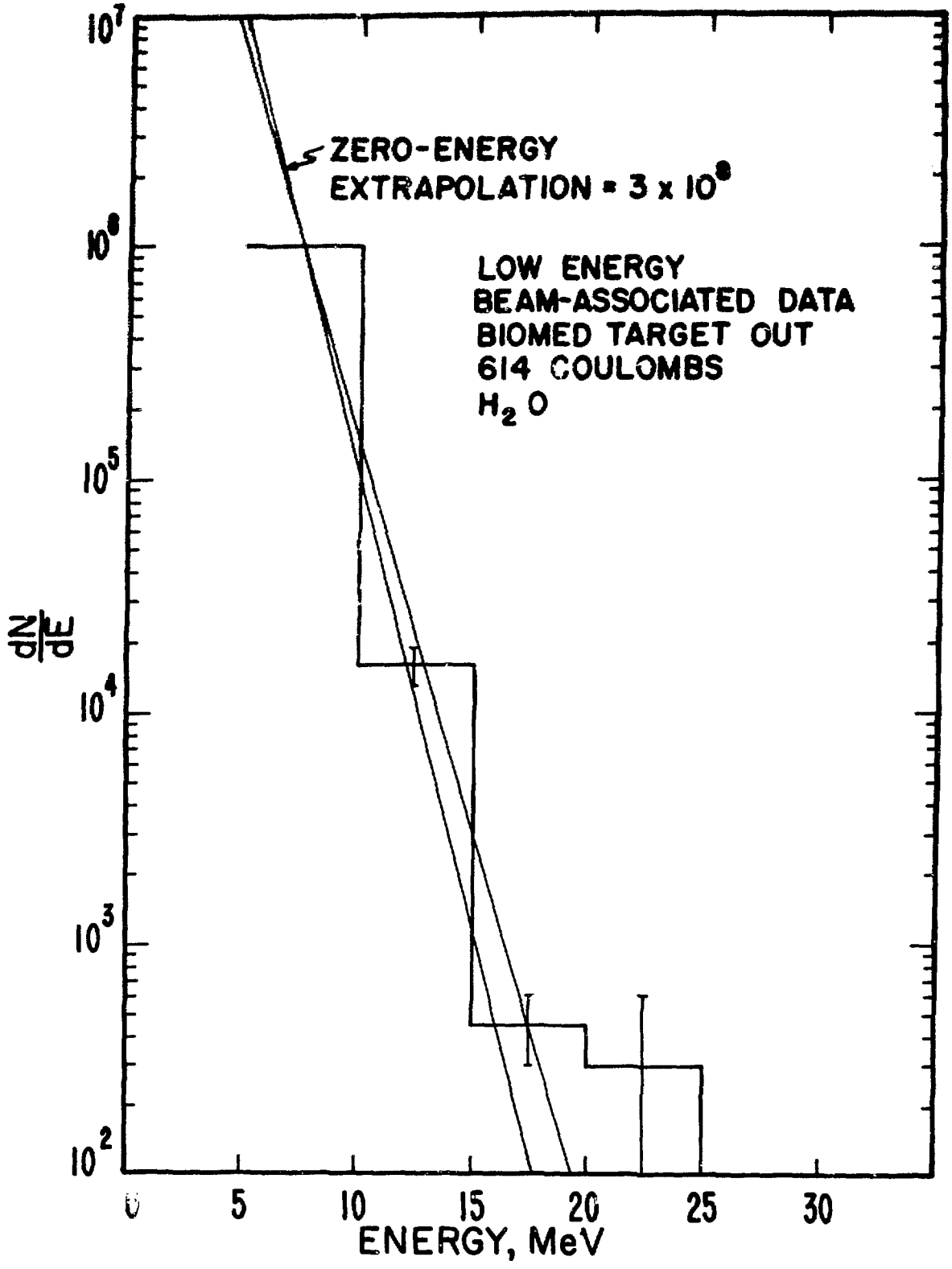

Fig. 24. Thermal neutrons, Biomed target out, H_2O.

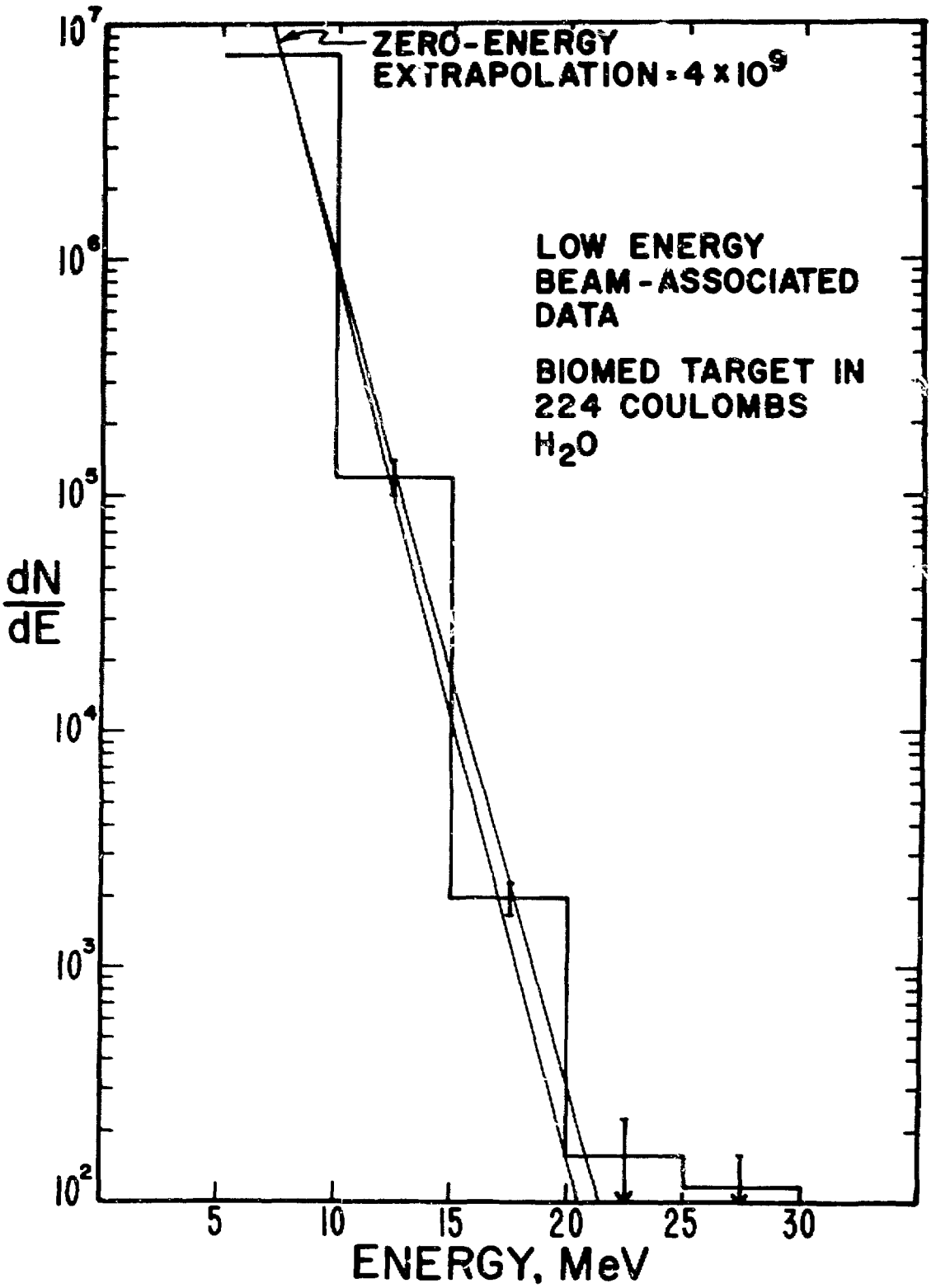

Fig. 25. Thermal neutrons, Biomed target in, H_2O.

Summed data, July 1977-March 1978.

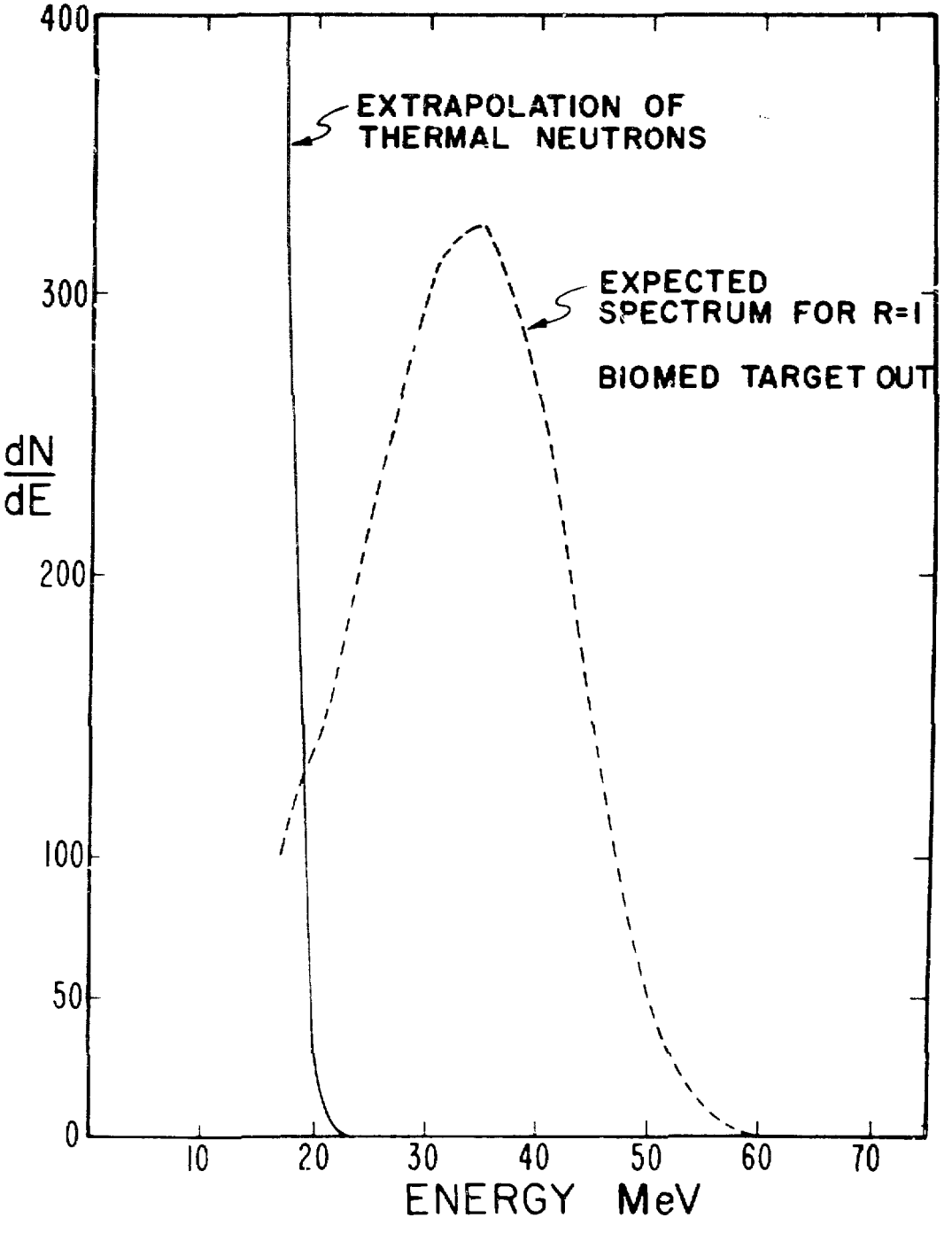

Fig. 26. Thermal neutrons, Biomed target out, H_2O, with calculated neutrino spectrum.

All expected spectra have 10% error.

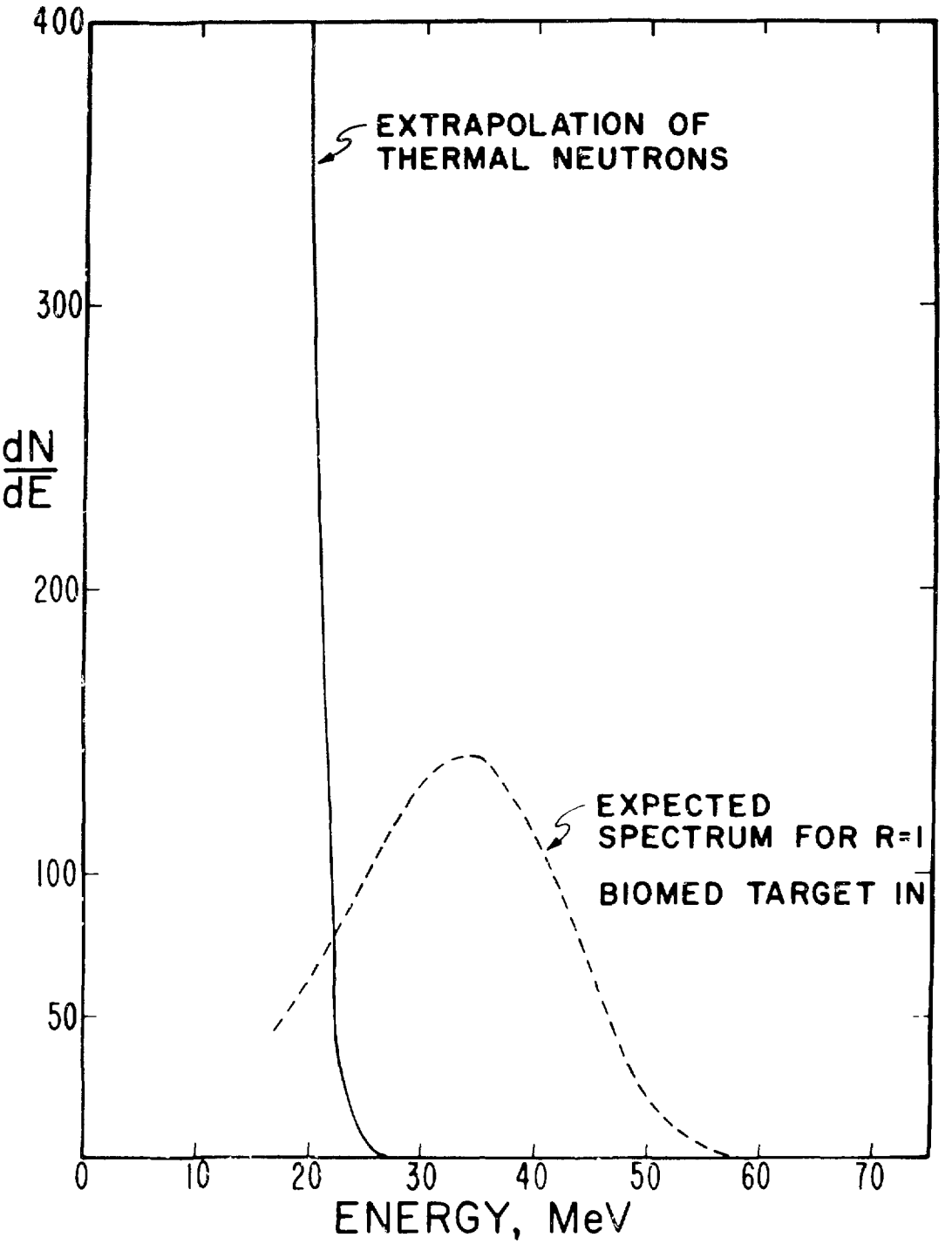

Fig. 27. Thermal neutrons, Biomed target in, H_2O, with calculated neutrino spectrum.

High-energy neutral events fell off much more slowly with energy; it was necessary to attenuate them by installing a sufficient amount of shielding in the direction of the beam stop to reduce the number of events in (20,60) MeV to about one per day at full beam intensity. The last sections of shielding, as indicated in Fig. 19, were not in place when the apparatus was originally installed. This allowed us to make beam-associated background measurements with the low beam intensity then available, at two shielding configurations other than the final one, namely 4 m and 5 m of iron shielding. Figure 28 shows the results of these measurements, plotting neutral events in (20,60) MeV/Coulomb vs shielding. The final shielding was 6.3 m of steel, which corresponded to less than about 2 events per day at 300 μA of beam on the beam stop. This is to be compared to the expected neutrino event rate of about 70 events per day, for R = 1. The shape of the background at 5 m of shielding is shown in Fig. 29. This shape was found to be the same at 4 m and 5 m of shielding, justifying the exponential extrapolation to higher shielding thicknesses. This background, extrapolated to 6.3 m and with the shape shown, was subtracted from the data, as described in the final chapter.

The biomedical target was also a source of neutron backgrounds. Figure 19 shows the relative position of that target to the beam stop and the neutrino detector. The angle between that target and the detector is quite forward, which contributed to the enhancement of the neutrons. The observed backgrounds were significantly higher with the target in than out at energies up to 20 MeV, as shown in Table VI. The target-in data, in fact, show a nonzero background up to 30 MeV.

The state of the biomed target was recorded on-line with each

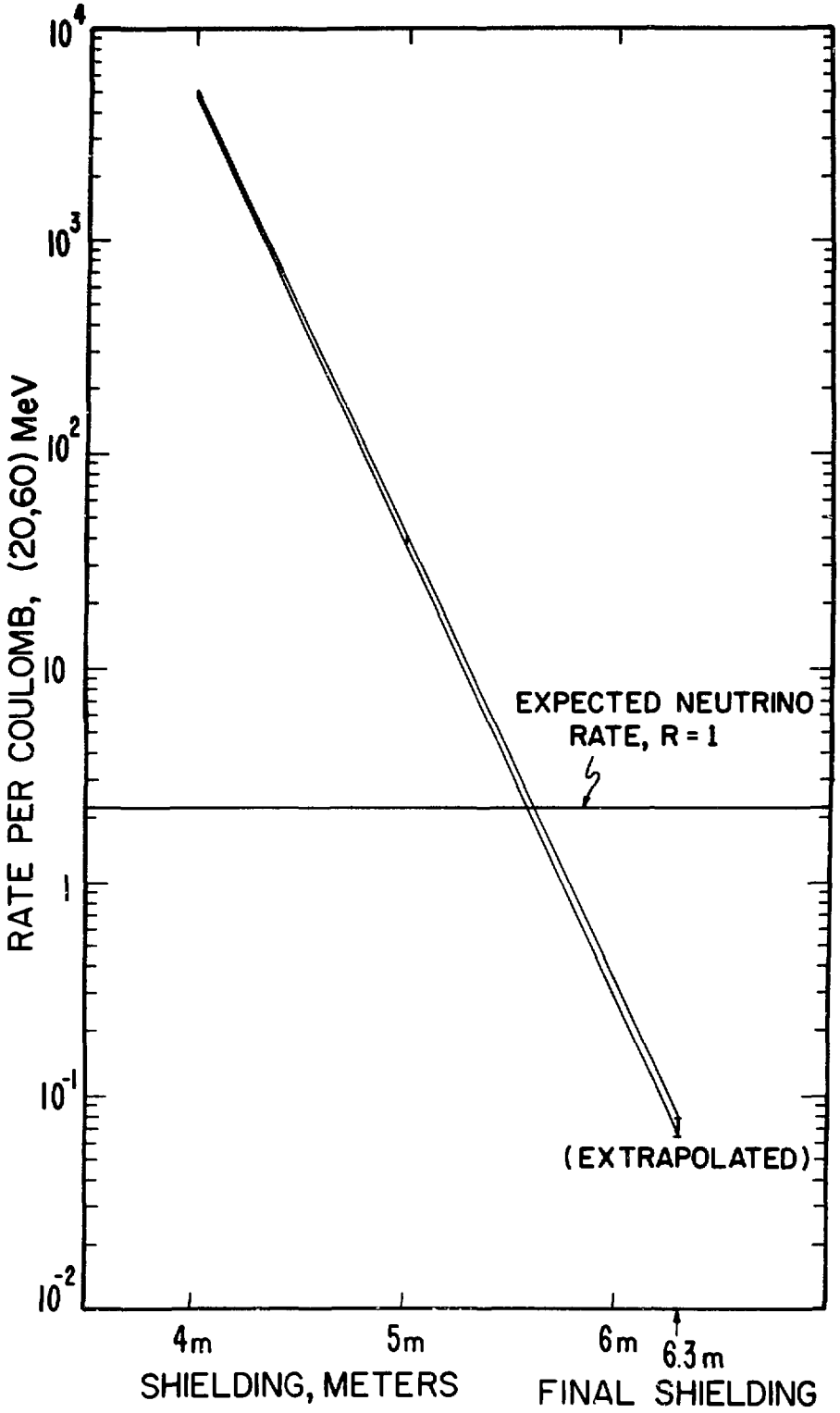

Fig. 28. Beam-associated neutrals rate vs shielding thickness.

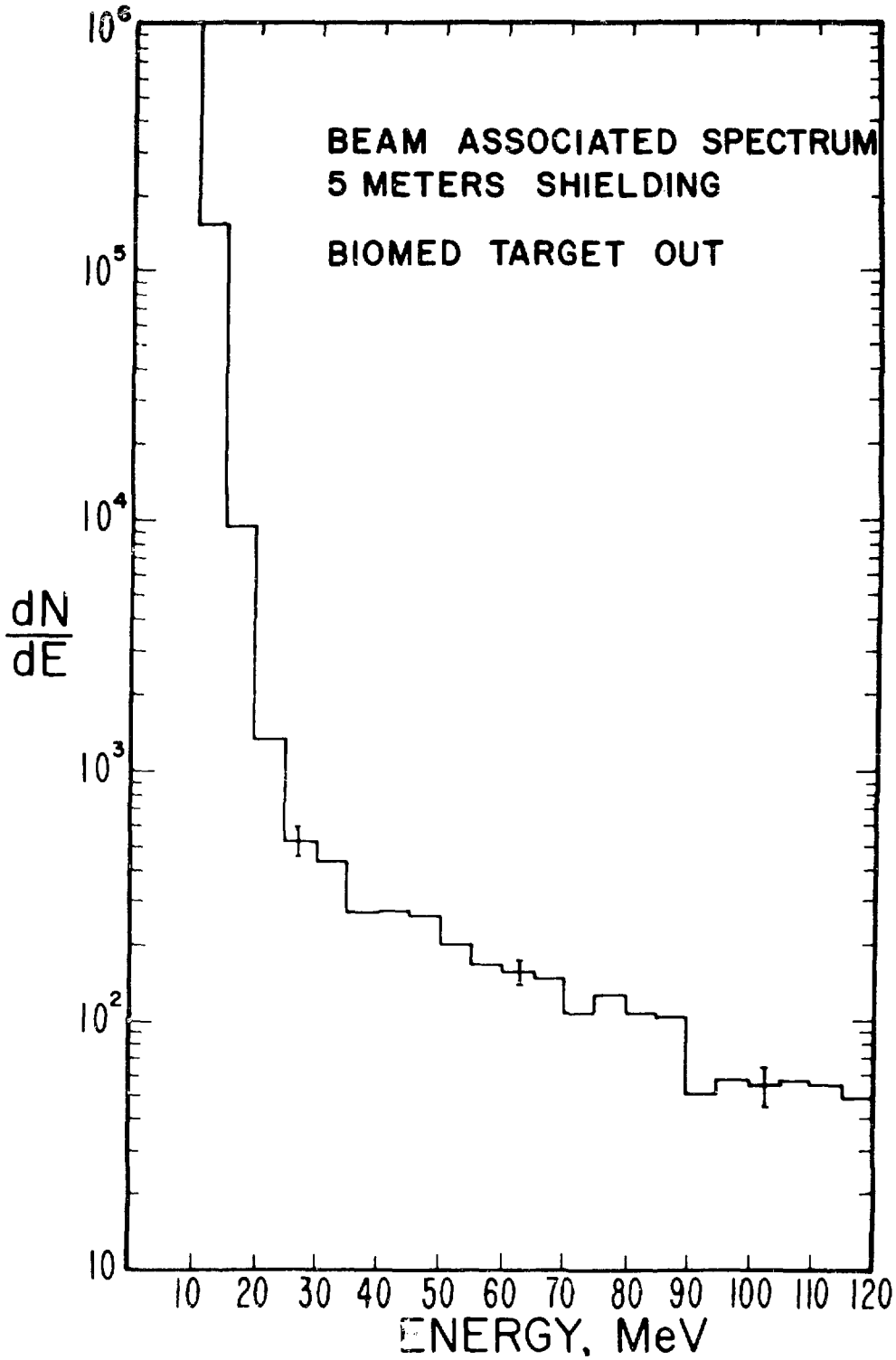

Fig. 29. Spectrum shape, beam-associated neutrals, 5-m shielding, Biomed target out.

TABLE VI

RATIO OF NEUTRON BACKGROUNDS, BIOMED TARGET IN/TARGET OUT, AS A FUNCTION OF ENERGY

Energy, MeV	R, In/Out (Neutrals Only)
0 (extrapolated)	35
5-10	20
10-15	15
15-20	10

event, and the two sets of data were treated completely separately in all analysis.

Cross-sections of electron neutrinos on carbon, oxygen, and aluminum have been calculated for the energy region 0-53 MeV, as discussed in the theoretical section. These cross sections are much suppressed due to nuclear effects and contributed very little to the background. Figure 30 shows the relative cross sections as a function of energy of $\bar{\nu}_e p$, $\nu_e d$, $\nu_e {}^{12}C$, and $\nu_e {}^{16}O$. Assuming 5800 kg of oxygen, 500 kg of carbon, and 100 kg of aluminum, the electron-neutrino reactions would contribute 0.06 events/Coulomb to the observed electron antineutrino signal over all energies.

The cross sections for carbon and oxygen were put through the Monte Carlo calculation mentioned above, to include the effects of radiation losses, resolution, and edge effects. The resulting spectra were then subtracted from the final spectrum, as described in the conclusions. The cross section as a function of energy for aluminum is not known, but the amount of aluminum was relatively small. The energy spectrum was assumed to be the same as that for oxygen.

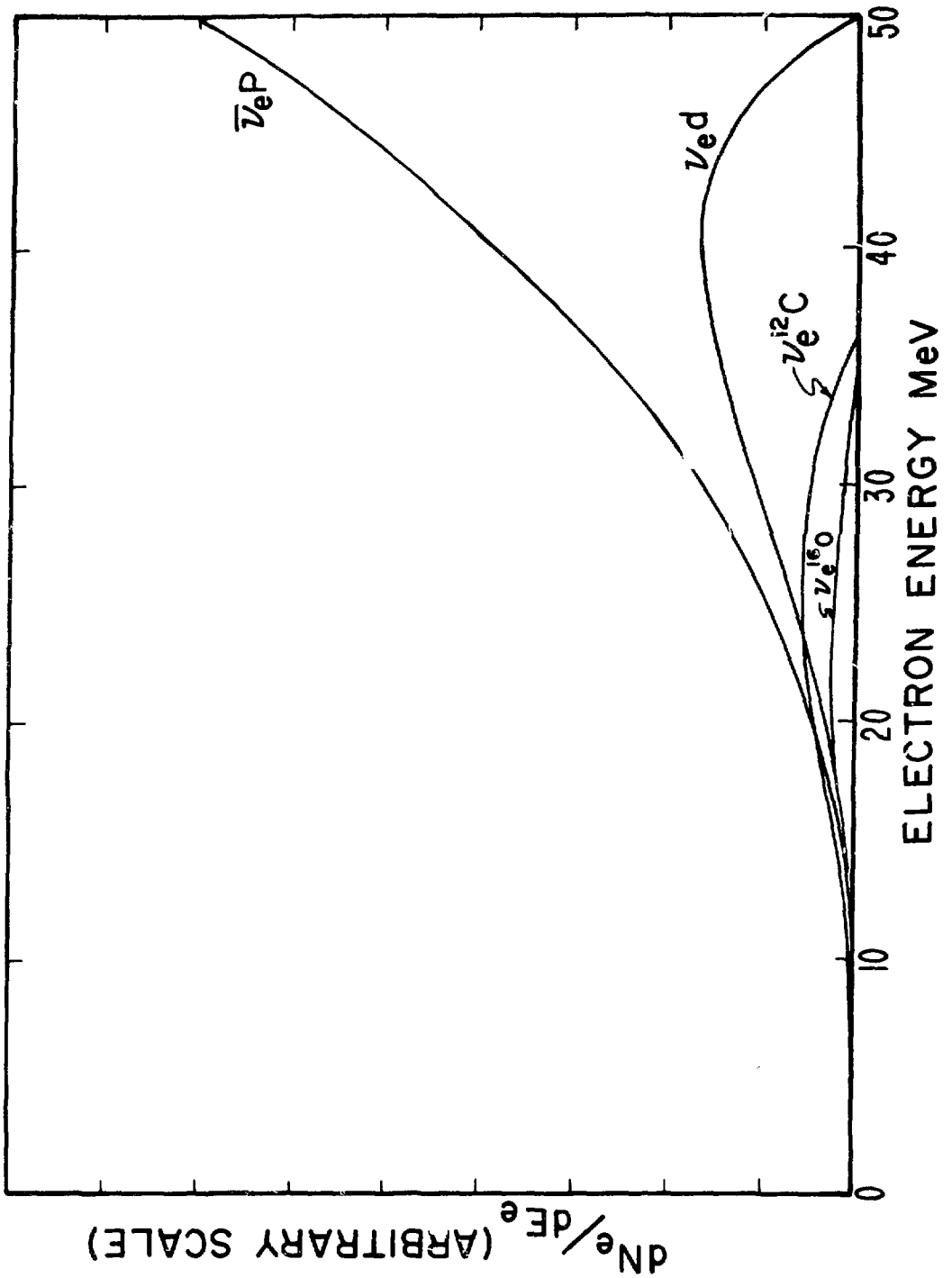

Fig. 30. Relative cross sections of $\bar{\nu}_e p$, $\nu_e d$, $\nu_e{}^{12}C$, and $\nu_e{}^{16}O$ as a function of energy.

Differential shielding measurements were not done during the D_2O fill, but the effect on the thermal neutrons could be seen by looking at the low-energy portion of the subtracted spectrum. Figures 31 and 32 correspond to Figs. 25 and 26 for H_2O; it can be seen that the zero-energy extrapolated rate was lower in D_2O by a factor of 4 for both biomed target conditions, giving a ratio, in/out, of 35, as before. From this we can conclude that, since the thermal neutron capture cross section is lower in D_2O by a factor of 550,[64] not all of the zero-energy extrapolation consisted of thermal neutron captures in water.

---

64. Reactor Handbook, Vol. I, ed. C.R.Tipton, Jr., New York, Interscience (1960). pp.848-850.

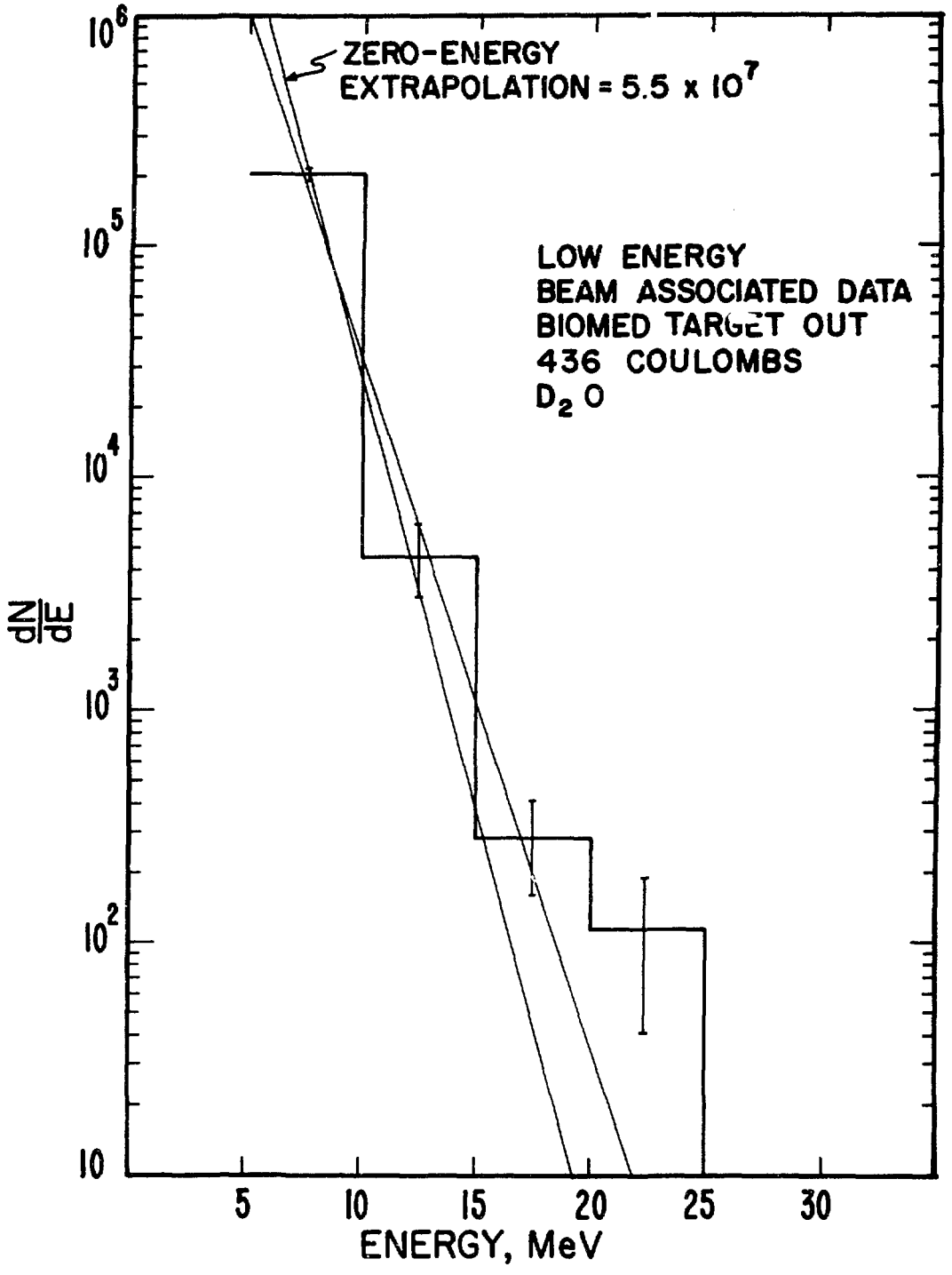

Fig. 31. Thermal neutrons, Biomed target out, D_2O.

Summed data, June-September 1978.

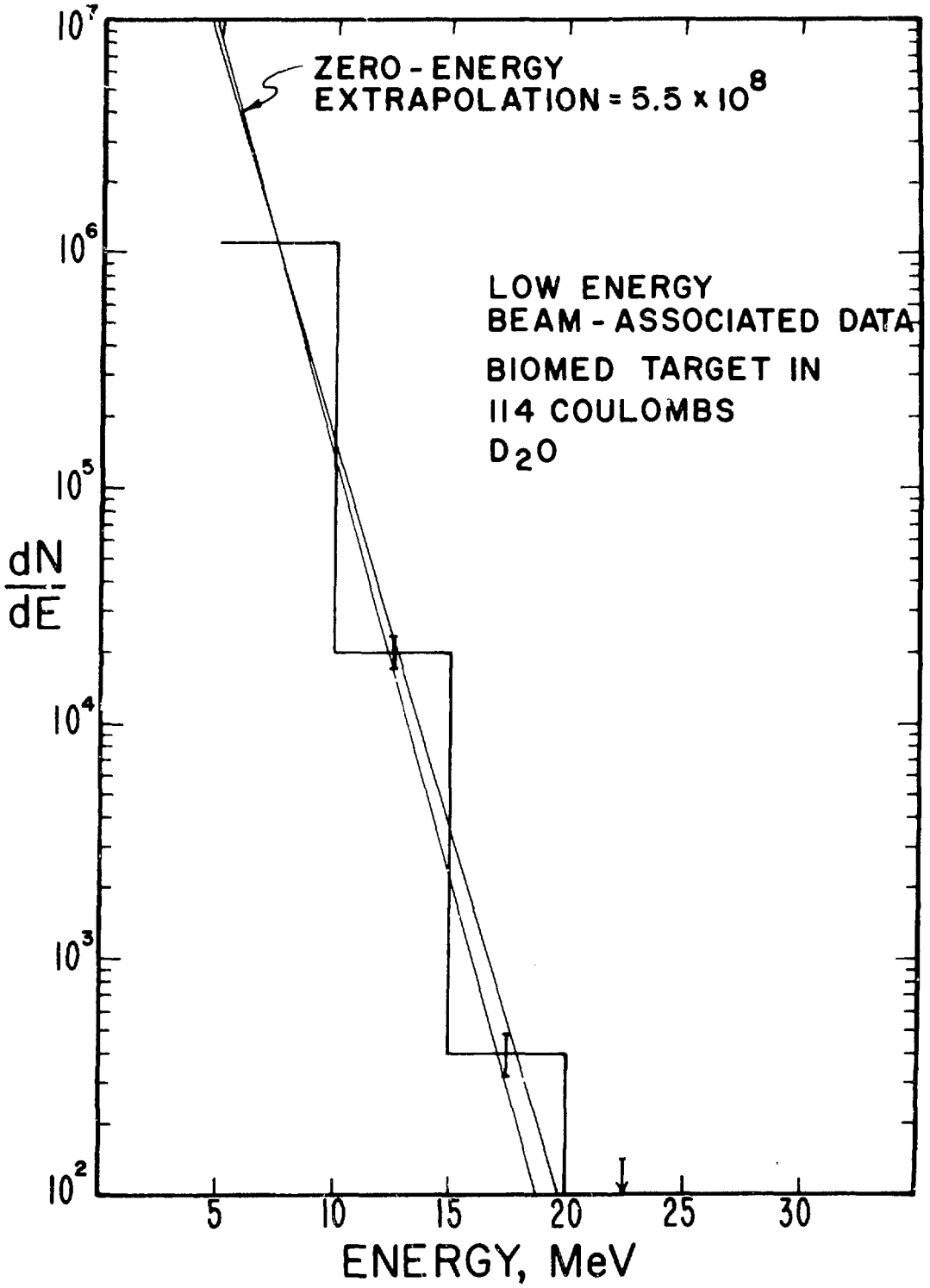

Fig. 32. Thermal neutrons, Biomed target in, D_2O.

Summed data, June-July 1978.

CHAPTER 5

ELECTRONICS

A block diagram of the event definition logic for the experiment appears in Fig. 33. Briefly, the electronics provided event definition and an event trigger to the computer for neutral events (neutrino candidates) and several other types of events, which were used for gain calibration and subtraction checks.

The phototube signals were bussed together in groups of four at the Cerenkov counter, giving us 24 signals in all, which we referred to as "supertubes." The supertube signals went directly to a CAMAC discriminator coincidence register, which was triggered by the event trigger and which gave a 1 for every supertube whose signal was above the discriminator threshold, and a 0 for the signals which were below -- 24 channels in all. This was read in for each event. The gains were set so that half the discriminators were set for a typical muon decay event. The supertube signals also went into six 4-fold linear mixers, the outputs of which were signals for a total side. The six side signals then went directly to six 256-channel CAMAC ADCs, which were read in by the computer for each event; these side signals also went to a voter coincidence (preceded by discriminators), which we typically ran at 2/6, to reduce contributions from tube noise. Finally, the side signals went into a linear mixer and fanout to provide a total signal. This total signal went through a variable attenuator, to allow for fine

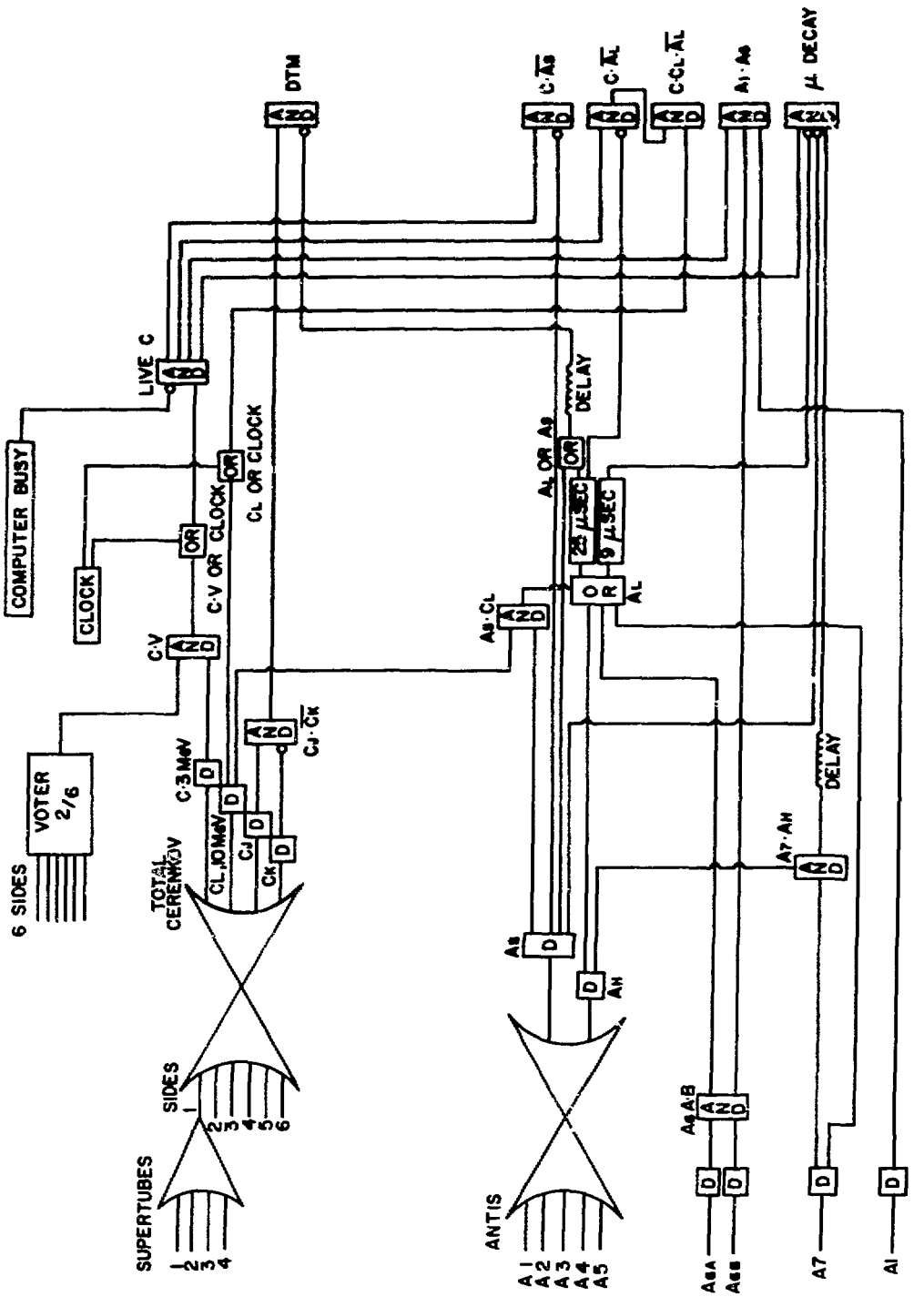

Fig. 33. Electronics block diagram.

adjustments of the gain, and then into two 256-channel CAMAC ADCs, one at 1 MeV/channel, and the other at 5 MeV/channel. These were also read in for each event. The total signal also went through several discriminators for event definition, as follows: C, 3-MeV, low-level threshold; C_L, 10 MeV, the lower threshold for neutrino candidate events; C_M, 30 MeV, originally used as an upper level for stopped muons; C_H, 100-MeV, high-level threshold; and C_J and C_K, around 200 MeV with C_J slightly less than C_K, for dead-time monitor events.

The signals from all eight tubes on a side of scintillators were bussed together at the scintillators, and a total signal for each side was brought into the trailer. The exception to this was the bottom scintillator, A_6, where the four tubes on each end were bussed together, and a coincidence made between the two signals (labeled A_6a and A_6b) to reduce noise. This was necessary because we had used the noisiest tubes on the bottom; very few (about 40/LAday) neutral events came through the bottom and nowhere else, so the efficiency did not need to be high. Scintillators 1-5 went through a linear mixer and then into two discriminators, A_S (short), 300 ns and high rate, and A_H (high), at a somewhat lower rate. The purpose of A_S was to discriminate against prompt charged particles; a high rate could be tolerated here because of its short length. The higher threshold, A_H, was a primary component of A_L (long), which was 25 μs in length and was intended to discriminate against μ-decay electrons. The other components of A_L were $A_6(a \cdot b)$, inserted here because it was not a component of A_H, A_7 (the second layer of top scintillators), and $C_H \cdot A_S$, which was included to catch events missed by an inefficiency in A_H. The length of this gate meant that its rate had to be kept fairly low in order to keep the dead time at an

acceptable level. Typical rates for A_L were 5 K/s giving a dead time from that one source of 12%.

The drift chambers, because of the 10-cm wire spacing, had a time jitter of about 1 μs, making it impossible to put them into the fast electronics in a way corresponding to the scintillator antis. Signals from all the wires in a single chamber were mixed together to give a single signal from each chamber; the four signals were mixed in the trailer. This yielded a gate which went into the CAMAC gated coincidence buffer used for the event latches, and any event (or clock) with that latch set was not analyzed but simply thrown out.

The event definitions started with a $C \cdot V$ coincidence, to incorporate the voter. A computer busy signal was also in this coincidence as an anti; this signal was set by the event latch and terminated by the computer when processing of the event was complete. A random noise generator was used as a clock to measure the live time; for maximum accuracy these clocks needed to look as much like events as possible. They were, therefore, mixed into the gates for $C \cdot V$, C_L, and $C_J \cdot \overline{C_K}$, went through the same event channels as normal events, and were separated only by a latch in the CAMAC register (see below).

The following is a list of all the event types that were used, with a brief description of each:

$A_1 \cdot A_6$: consisted of $A_1 \cdot A_6 \cdot C \cdot V$; throughgoing cosmic rays, used as an energy calibration.

DTM: consisted of $(C_J \cdot \overline{C_K})\overline{(A_L \text{ or } A_S \text{ delayed})}$ these were high-energy charged events with no beam-associated component, but with the same live time as true

neutrals (the reason for including the delayed anti); used to check subtraction. Rate was adjusted by changing width of window.

$C \cdot \overline{A_L}$: consisted of $C \cdot V \cdot \overline{A_L}$; low-energy neutral events, separated from higher-energy events because of high rate.

$C \cdot C_L \cdot \overline{A_L}$: consisted of $C \cdot V \cdot C_L \cdot \overline{A_L}$;best neutrals, these were the neutrino candidates.

$C \cdot C_L \cdot \overline{A_S}$: consisted of $C \cdot V \cdot C_L \cdot \overline{A_S}$, later (after run 933) of $C \cdot V \cdot \overline{A_S}$; mostly muon decays, used for energy calibration and checking effect of overshoot. (The overshoot problem is discussed below, under "Checks and Calibrations.")

μ Decay: consisted of $[(C \cdot V \cdot \overline{C_M} \cdot A_H)$ delayed 2 μs)] $\cdot C \cdot V \cdot \overline{A_S}$; upper level was to avoid overshoot problems, as was delay; used to set gain of counter since energy is the same as for neutrino events. Changed to $[(A_7 \cdot A_H)$ delayed 10 μs] $\cdot C \cdot V \cdot \overline{A_S} \cdot \overline{A_L}$(9 μs) to give triggers throughout volume of counter and to reduce accidentals.

Each event gate went through a prescaler and into a common event mixer and fanout; the normal prescalings were as follows:

$A_1 \cdot A_6$	×100
DTM	×1(to keep its live time the same as the

neutrals)

$C \cdot \overline{A_L}$	×100
$C \cdot C_L \cdot \overline{A_L}$	×1
$C \cdot C_L \cdot \overline{A_S}$	×100
μ Decay	×10 (old definition)
	×1 (new definition)

The sole purpose of the prescaling was to keep the event rate reasonable; with this set, the total event rate was about 6/live second. A separate latch for each event type went to a CAMAC gated coincidence register; this register also received latches for beam on/off, biomed target in, and clock (this is how the clocks were distinguished from true events). The register was gated by the event mixer/fanout and read in for each event and clock. Table VII shows the CAMAC register word, with the definition of each bit.

TABLE VII

CAMAC COINCIDENCE REGISTER WORD

Bit	Definition (Bit = 1 if true)
0	Beam Out
1	Bio In
2	Clock
3	$A_1 \cdot A_6$
4	DTM
5	$C \cdot C_L \cdot \overline{A_L}$
6	$C \cdot \overline{A_L}$
7	$C \cdot (C_L) \cdot \overline{A_S}$
8	Mu Decay
9	Beam In
10-15	not used
16	Event
17	Drift Chamber
18-23	not used

CHAPTER 6

DATA ACQUISITION

A. DATA ACQUISITION

The on-line data acquisition computer was a Data General Supernova.[65] Figure 34 is a simplified flow chart of the data-acquisition program. The event mixer and fanout sent a signal to the enabling gate of the C212 gated coincidence register when an event was received; this then generated a LAM in the CAMAC crate. Upon receipt of the LAM, the computer went into the event handling routine outlined in the figure. If the "clock" bit was set, the event and its ADC readings were accumulated; all non-clock events were written on tape with no further selection. The only exception to this were events where the drift chamber bit was set; all such events and clocks were thrown out without ever being stored.

Beam gates were produced from an analog signal produced by a current monitor just upstream of the A6 beam stop. The length of this signal was 500 μs for a 6% duty factor, and 625 μs for a 7.5% duty factor; the repetition rate was 120 Hz, or 8.3 ms between beam spills. Two gates were generated from this pulse: a 500- or 625-μs prompt gate, and a 3- or 3.75-ms delayed pulse, which was used to measure the cosmic-ray background. The time structure of these pulses is shown in

65. Data General Corporation, 15 Turnpike Rd., Westboro, MA 01581.

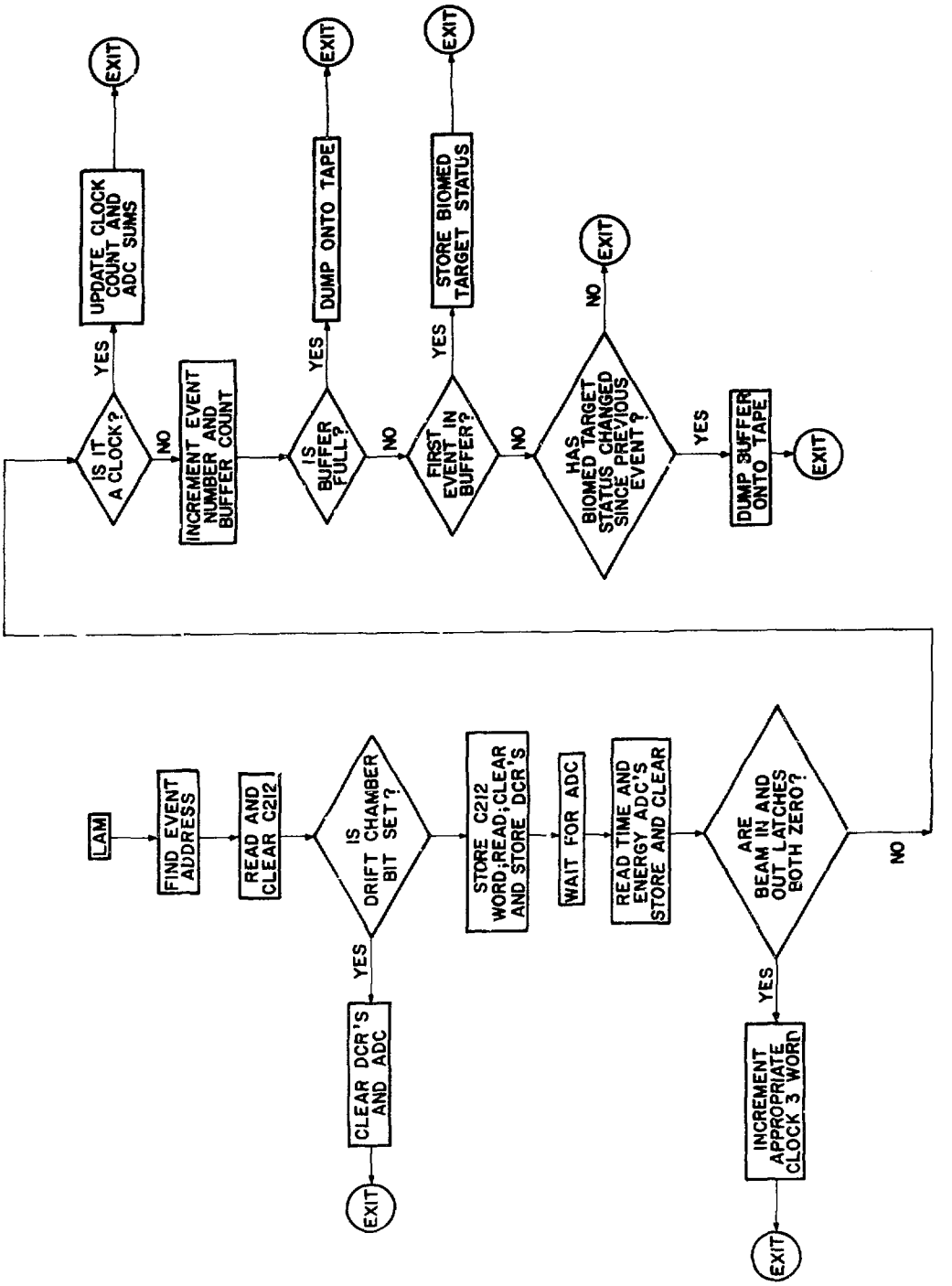

Fig. 34. Flow chart, data-acquisition program.

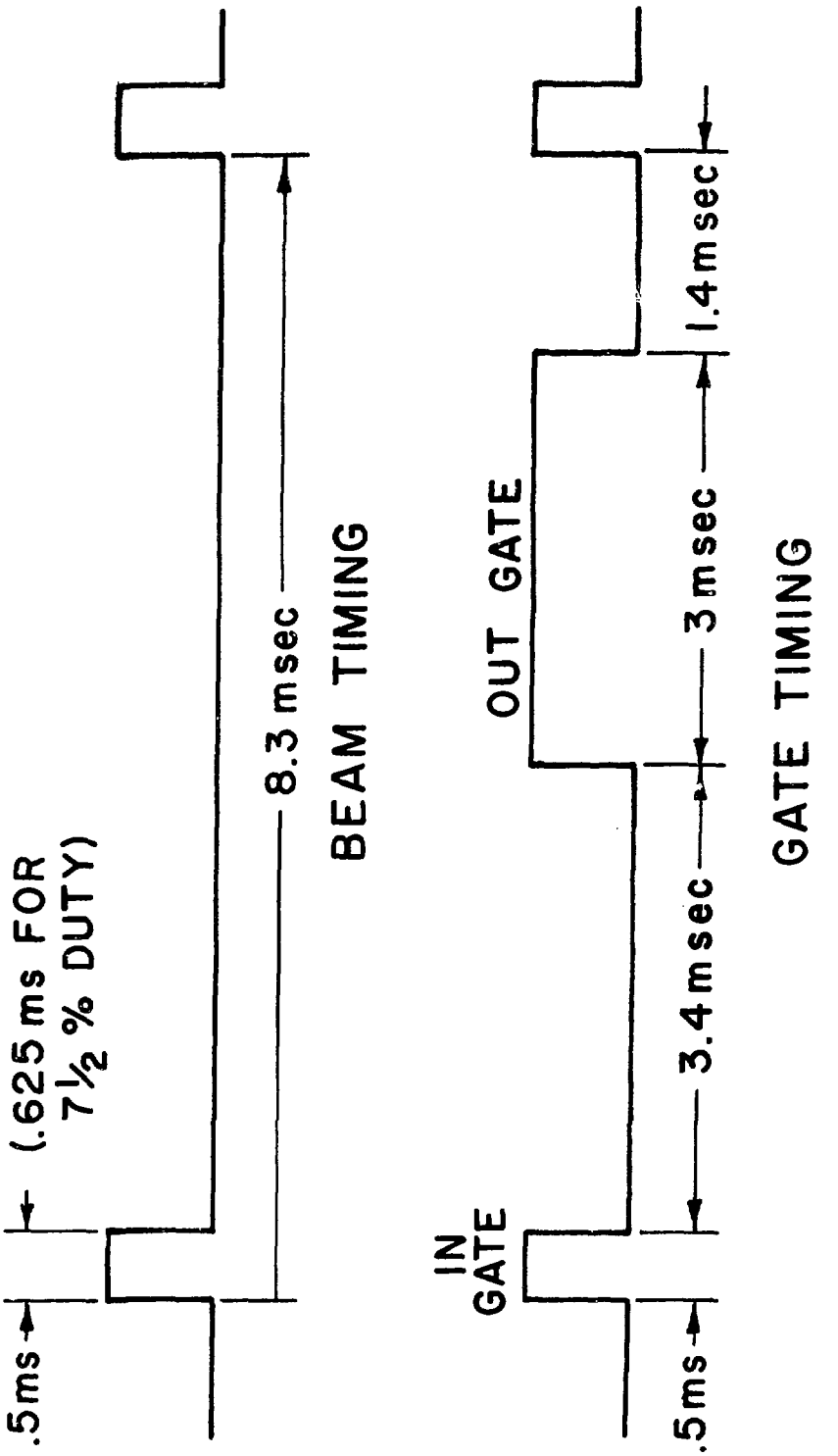

Fig. 35. Beam and gate timing.

Fig. 35, along with the time structure of the actual beam spill. These "beam in" and "beam out" gates each had a separate latch in the C212, as shown in Table VII.

In order to make a subtraction of the cosmic-ray background as measured during the out gate, it was necessary to make an accurate measurement of the live time during each gate. This was done by having a random clock "or"ed into the event logic, as described in the previous section. At the end of each run, a ratio would be made of the clocks in the in and out gates, for each biomed target condition, and this number would be the factor by which the "out" events would be renormalized. The live time for the clocks should have been the same as the live time for the events, since the clocks were random in time, had the same sources of dead time as the events, and were not prescaled. The subtraction was checked frequently whenever the beam was off for several days; the results were not statistically different from zero.

Table VIII shows a list of inputs to the five hex CAMAC scalers. Two of these units were gated "beam in", two were gated "beam out", and the fifth was ungated, as indicated in the table. "Live event" scaled the event faninout, vetoed by the live clock. "C_H" was the high-level (100-MeV) Cerenkov total rate. "Live clock" was a coincidence between the event faninout and the clock. "Clock" scaled the clock directly. "$A_6 \cdot C_H$" gave a large signal in the Cerenkov counter in coincidence with a signal in the bottom scintillator; "$A_6 \cdot C_H \cdot \bar{A}_H$" was this signal with nothing in the side or top scintillators. The ratio of these two measured the anti inefficiency. "$C_H \cdot A_7$" was a coincidence between a large signal in the Cerenkov counter and the second layer of top scintillators. "$C_H \cdot \bar{A}_L$" was a large signal in the Cerenkov counter

with nothing in any of the antis. "P_6" was an integrated pulse train from the current monitor just upstream of the beam stop; the number of pulses in each spill was proportional to the amount of beam in the spill. "$C_H \cdot DC$" was a coincidence between a large signal in the Cerenkov counter and the drift chambers. "1.1 KHz" was a regular (nonrandom) clock whose function was to measure the total elapsed time. "Drift chamber" scaled the chambers directly. "A_7" scaled the second layer of top scintillators. "Voter" scaled the output of the voter coincidence unit. "A_S" was the low-threshold scintillator output, and "A_H" the high threshold. "$C \cdot V$" was the coincidence between the 3-MeV Cerenkov discriminator and the voter. "Mu stop" was the coincidence $A_7 \cdot A_H$ used to define a stopping muon for the μ-decay event trigger. "Beam gates in" scaled the number of beam spills with beam. "T zero gates" scaled the master timer of the accelerator; this normally ran at 120 Hz.

The scalers were monitored on line by the computer, and certain ratios of the scalers were checked periodically to see if they fell within certain limits. If not, a warning containing the numbers of the scalers, the value of the ratio, and the time was printed out. Table IX is a list of these warnings. The first measured live events per second for beam in; this could have been wrong if the dead time were high, or if something were wrong with the antis. The second measured the anti inefficiency. The third measured the rate in the scintillators. The fourth measured the drift chamber rate. The fifth was the dead time, excluding dead time due to the drift chambers. The sixth, 1.1 KHz/T zero gates, would have been off if T zero were not at 120 Hz, as sometimes occurred when the accelerator was having problems. The

TABLE VIII

CAMAC SCALERS

Scaler	Definition	Gating
1	Live Event In	Gated "In Beam" Only
2	C_H	
3	Live Clock	
4	Clock	
5	$A_6 \cdot C_H$	
6	$A_6 \cdot C_H \cdot \overline{A_H}$	
7	$C_H \cdot A_7$	
8	$C_H \cdot \overline{A_L}$	
9	P6	
10	$C_H \cdot DC$	
11	1.1 KHz	
12	Drift Chamber	
13	Live Event Out	Gated "Out Beam" Only
14	A_7	
15	Voter	
16	Clock	
17	A_S	
18	-	
19	$C \cdot V$	
20	$A_6 \cdot C_H$	
21	$A_6 \cdot C_H \cdot \overline{A_H}$	
22	A_L	
23	1.1 KHz	
24	Mu Stop	
25	Beam Gates In	Ungated
26	-	
27	Ungated Clock	
28	T Zero Gates	
29	1.1 KHz	
30	-	

seventh was the C • V rate. The eighth was A_7, the second layer of top scintillators. The ninth was the event rate for beam out. The tenth measured the clock ratio, beam in/beam out; this could vary if the clock were not running at the same rate during each gate, which sometimes occurred via pickup from the line voltage.

Figure 36 is a copy of the run sheets that were filled out at the end of each run. This involved checking the rates of all the scalers, the rates of each event type, the cosmic-ray neutrals rate, and the beam-associated rates of the neutral events. This enabled us to keep close track of the condition of the entire experiment, and to fix things shortly after they went wrong. These sheets were not used for any part

TABLE IX

SCALER WARNINGS

Number	Scalers	Minimum	Maximum
1	1,11	0.002	0.02
2	21,20	0	0.0005
3	22,23	3	9
4	12,11	3	7
5	3,4	0.6	1
6	29,28	9.1	9.6
7	19,23	0.5	0.7
8	14,23	0.5	1
9	13,23	0.002	0.02
10	4,16	0.175	0.185

RUN NO.	TRIGGERS / PRESCALED BY	$A_1 \cdot A_8$	DTM	$C \cdot C_L \cdot \bar{A}_L$	$C \cdot A_L$	$C \cdot A_8$	MH DECAY	
DATE:	TAPE:	C_T ATT= dB		LINAC		$A_1 \cdot A_8$ PEAK=		HOURS=
LOG:	FILE:	1 MeV/CH ☐		CURRENT:		395 MeV? ☐		

COMMENTS:

CHECK DISPLAYS: EARLY IN RUN ☐ END OF RUN ☐

BEAM INFORMATION	BIO OUT	BIO IN
BEAM ON A_8 (CCR)	μA	μA
TOTAL TIME	SEC	SEC
ESTIMATED TOTAL BEAM	mA·SEC	mA·SEC
TOTAL BEAM (P_8 SCALER)	mA·SEC ☐	mA·SEC ☐
LIVE BEAM	mA·SEC	mA·SEC

RATE CHECKS	BEAM IN GATE: BIO OUT	BEAM IN GATE: BIO IN	BEAM OUT GATE: BIO OUT	BEAM OUT GATE: BIO IN	
SECONDS (1.1 KHz)					
% LIVE ($\frac{\text{CLOCK 2}}{\text{CLOCK}}$)					☐
LIVE SECONDS					☐
$\frac{\text{LIVE EVT}}{\text{LIVE SEC}}$ (USE CLOCK 4)					☐
$C \cdot C_L \cdot \bar{A}_L$/LIVE SEC					☐
$C \cdot \bar{A}_L$/LIVE SEC					☐
DTM/LIVE SEC					☐
$A_1 \cdot A_8$/LIVE SEC			BIO IN + OUT		☐
$C \cdot C_L \cdot \bar{A}_8$/LIVE SEC					☐
μ DECAY/LIVE SEC					☐

SCALER RATES	BIO OUT	BIO IN	SCALER RATES	BIO OUT	BIO IN	☐
A_7/SEC ☐			$C_H \cdot DC/CH$			☐
A_8/SEC ☐			RANDOM CLOCK/SEC			☐
A_L/SEC ☐			1.1 KHz/SEC			☐
DC/SEC ☐			C_H/SEC			☐
C·V/SEC ☐			μ STOP/SEC			☐
A_H INEFF ☐			$\frac{\text{CLOCK IN} \cdot \text{1.1 KHz OUT}}{\text{1.1 KHz IN} \cdot \text{CLOCK OUT}}$			☐
A_L INEFF ☐			% GATELESS EVENTS			☐
$C_H \cdot A_7/CH$ ☐			% GATELESS CLOCKS			☐

Fig. 36. Run sheet.

PAGE 2 - RUN NO. SPECTRA

COSMIC NEUTRAL: BEAM OUT ONLY.

	BIO OUT	BIO IN	ΣBIO IN+OUT	
LIVE LADAYS (BEAM OUT)				
NEUTRALS Σ(20,60)/ LIVE LADAY			±	☐
NEUTRALS Σ(30,60)/ LIVE LADAY			±	☐

BEAM ASSOCIATED RATES

		IN GATE	OUT GATE (RENORM)	Δ	Δ/OUT (%)	Δ/LIVE BEAM (mC)
BIO OUT	DTM			±	±	☐ LIVE BEAM:
	NEUT. Σ(30,60)			±	±	☐
	NEUT. Σ(10,30)			±	±	☐
	C·$\overline{AL}$ Σ(5,10)			±	±	☐
BIO IN	DTM			±	±	☐ LIVE BEAM:
	NEUT. Σ(30,60)			±	±	☐
	NEUT. Σ(10,30)			±	±	☐
	C·$\overline{AL}$ Σ(5,10)			±	±	☐

ACCUMULATED RATES: GOOD RUNS STARTING WITH NO.

		IN GATE	OUT GATE (RENORM)	Δ	Δ/OUT (%)	Δ/LIVE BEAM (mC)
BIO OUT	DTM			±	±	LIVE BEAM: ☐
	NEUT. Σ(30,60)			±	±	☐
	NEUT Σ(10,30)			±	±	☐
	C·$\overline{AL}$ Σ(5,10)			±	±	☐
BIO IN	DTM			±	±	LIVE BEAM: ☐
	NEUT. Σ(30,60)			±	±	☐
	NEUT. Σ(10,30)			±	±	☐
	C·$\overline{AL}$ Σ(5,10)			±	±	☐

Fig. 36. Run sheet (continued).

of the off-line analysis, however; that was done directly from the original data tapes by a larger computer, and will be described in another chapter.

The on-line analysis program also put events into histograms which were stored on disk files; these disk files were written onto tape periodically, and were useful for diagnostics, trouble-shooting, and some analysis. Table X shows a list of these histograms, along with the latch pattern for each histogram as read from the C212 word (see Table VII). These latch patterns were exclusive; that is, the given pattern, with no additions or deletions, must have matched the C212 word for an event to have been accepted into any given histogram.

B. CALIBRATIONS AND CHECKS

We had a number of ways in which to check the energy calibration of the counter -- the energy spectrum of decay electrons from cosmic-ray muons; throughgoing cosmic rays; and events from the $C \cdot C_L \cdot \overline{A}_S$ trigger. The μ-decay electrons were the most pertinent check, since their energy spectrum was the same as the μ-decay antineutrinos from the beam stop, and since they were the same type of particle, as opposed to muons, which did not necessarily have the same energy loss per centimeter at the same energy as electrons. This spectrum was therefore used to set the gain of the counter, by comparing it with a theoretical Monte Carlo spectrum. The overshoot from the phototubes was a particular problem for this spectrum, however, because the μ-decay electron, of energy 0 to 53 MeV, followed directly after a muon which could have an energy up to 400 MeV. A 1% overshoot on the muon signal could therefore shift the electron signal 10% or more. Our original way

TABLE X

SPECTRUM DEFINITIONS

	Spectrum	Latches
0	Neutral Beam/I Bio/O	1340,1360
1	Neutral Beam/O Bio/O	341,361
2	Neutral Beam/I Bio/I	1342,1362
3	Neutral Beam/O Bio/I	343,363
4	DCRs	7777 (dummy)
5	$A_1 \cdot A_6$ Beam Out	11,13
6	$C \cdot C_L \cdot \overline{A_S}$	201,203
7	$C \cdot \overline{A_L}$ Beam/I Bio/O	1300
8	$C \cdot \overline{A_L}$ Beam/O Bio/O	301
9	$C \cdot \overline{A_L}$ Beam/I Bio/I	1302
10	$C \cdot \overline{A_L}$ Beam/O Bio/I	303
11	Mu Decay ADC 0	401,403,601,603
12	DTM Beam/I Bio/O	1020,1030,1360
13	DTM Beam/O Bio/O	21,31,361
14	DTM Beam/I Bio/I	1022,1032,1362
15	DTM Beam/O Bio/I	23,33,363
16	Time Beam/I Bio/O	7776 (dummy)
17	Time Beam/O Bio/O	7776 "
18	Time Beam/I Bio/I	7776 "
19	Time Beam/O Bio/I	7776 "

of avoiding this problem in the μ-decay trigger was to put an upper limit of about 30 MeV on the muon signal, thus reducing by a factor of

10 or more the maximum size of the overshoot. This, unfortunately, had the effect of restricting the decay electrons to a limited portion of the counter, and they were therefore not as similar to the neutrino events as they could have been, since the neutrino events will occur uniformly throughout the counter. We therefore decided to redefine the stopping muon trigger to consist just of the antis $A_7 \cdot A_H$ (the coincidence was to reduce noise) with no constraints on the Cerenkov signal at all. We then looked for a second signal delayed by 10 μs, which was long enough to eliminate the overshoot problem. We included a 9 μs anti to ensure that the electron we were looking at came from the original muon and not from any other muon which may have stopped in the counter during the delay time. Figure 37 shows the measured μ-decay spectrum with this final definition, and the Monte Carlo calculation of the spectrum. The energy scale of the Monte Carlo spectrum was adjusted to make the peaks coincide.

The throughgoing cosmic rays were defined by a coincidence of the top and bottom antis, $A_1 \cdot A_6$. The expected position of this peak was well-defined by the size of the counter, so it could be used on line to adjust the gain of the counter, which we tried to keep at 1 MeV per channel. The intrinsic gain of the counter could change due to variations in the cloudiness of the water and to fluctuations in the gains of the phototubes. The gain indicated by this trigger could be compared to the gain indicated by the μ-decay trigger as a consistency check.

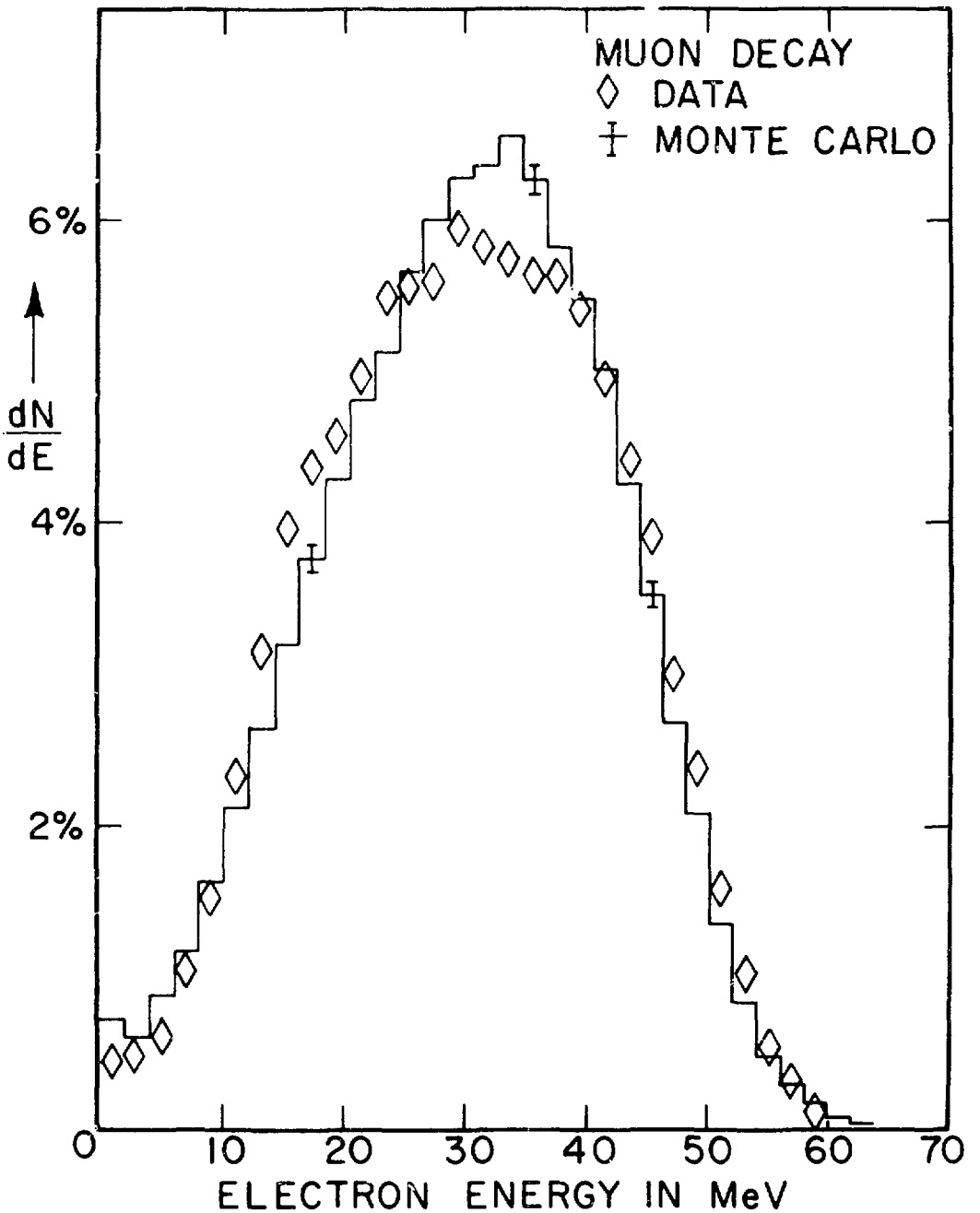

Fig. 37. Measured and calculated muon decay spectra.

The $C \cdot C_L \cdot \bar{A}_S$ trigger also consisted primarily of muon decays; it was not too useful by itself since it suffered from the overshoot problem described above, but it was useful to compare it to the muon decay trigger to see the maximum effect of the overshoot.

As mentioned above, all the phototubes on both the Cerenkov counter and the scintillators were provided with LEDs to allow testing. We had computer programs which would flash each LED in succession, read in the ADCs, and print out a table of readings for all the tubes. This allowed us to check that all the tubes were functional. These tests were run daily when we were taking data. We could also tell if the gain of a tube had changed, but we did not use these readings to set the gains, as our experience was that the gains were very stable on a day-by-day basis. What we did was to set the gains of all the tubes at once, using throughgoing cosmic rays as a light source. This was done every few months.

The subtraction was checked run by run using the DTM trigger described above. The subtraction was also checked for an entire cycle summed together, and for the total data. The results were not significantly different from zero (but see the comments on Cycle 18, in the chapter on analysis). The subtraction for all the running was $(-0.10 \pm 0.11)\%$.

C. HISTORY OF THE EXPERIMENT

The following chart gives a brief outline of the history and development of the experiment, noting general activities and important milestones and events.

1970:	Small prototype Cerenkov counter built and tested at Saclay
15 March 1971:	LAMPF proposal submitted
January 1972:	Testing of sample phototubes and prototype base at Yale
June-July 1972:	Testing of prototype Cerenkov counter at Yale, with antis
10-31 August 1972:	Measurement of beam-associated rates in prototype Cerenkov counter at Berkeley cyclotron
5 November 1972-15 February 1973:	Tests of prototype Cerenkov counter in neutrino tunnel at BNL (cosmic-ray studies)
1 April 1973:	Testing of epoxy castings at Yale
20 June 1973:	Start of testing of scintillators for antis, at LAMPF
Summer 1973:	Cerenkov counter built; SEW joins experiment
17 December 1973:	First test of Cerenkov counter with phototubes, at Yale
25 February 1974:	Radiation levels in LAMPF neutrino house measured, 2-μA beam
3 March 1974:	First look at beam-associated events at LAMPF with prototype Cerenkov counter
14 March 1974:	Cerenkov counter installed in neutrino house
5 May 1974-6 June 1974:	Beam studies with Cerenkov counter, 16 tubes, 2-μA beam
25 October 1974:	Top and bottom antis installed

8-19 December 1974:	Beam studies, all tubes mounted, 10- to 13-μA beam, shielding plug raised on 16 December
19 December 1974:	Start of Great Shutdown of LAMPF accelerator
July-December 1975:	Scintillator stands set up, scintillators mounted, tubes put on and tested, stands moved in place
5 April 1976:	End of Great Shutdown; Cycle 1, 10-μA beam
April-June 1976:	Measurements of beam associated background at 3.25 m and 4 m of shielding
18-20 June 1976:	Fifth meter of shielding added
June-November 1976:	Measurements of beam associated background at 5 m of shielding
July-October 1976:	Measurements of effect of varying amounts of lead on cosmic rays
November 1976-March 1977:	Installation of last 1.3 m of shielding; experiment disassembled, moved back, and reassembled
1 June 1977:	A_7, second layer of top antis, installed
13 June 1977:	Drift chambers installed; system complete
13 July 1977:	Cycle 16, 225-μA beam, start of data-taking

Details of beam-associated running conditions are in the final chapter, with the results.

October-November 1977:	Setup disassembled, counter repaired, reassembled

April-May 1978:	Setup disassembled, counter repaired, made ready for D_2O fill; filled and reassembled
June-September 1978:	D_2O running
8 November 1978:	Resume water running
7 May 1979:	End water running

CHAPTER 7

ANALYSIS

The analysis of this experiment consisted primarily of sorting events into histograms based on event type, biomedical target condition, and beam condition; renormalizing the "outside beam" spectrum to correspond to the same amount of live time as the "inside beam" spectrum; subtracting to find a beam associated spectrum; and fitting this spectrum to a calculated neutrino spectrum to find a value for the branching ratio. A few cuts were made on the data before putting them into histograms; these will be described below.

The format of each event as written on tape is shown in Table XI. Events were written on tape in sets of 200; each contained 200 events with 8 words per event, followed by clocks and clock sums, and scalers, accumulated since the last tape dump. When rereading these original tapes, a run sheet (see Fig. 36) was calculated. This allowed us to check rates and subtractions, just as the on-line hand calculated ones did. There were also options for up to 5 scatter plots and 20 histograms to be generated. Variables could be defined from the information on the tape; these variables could then be plotted. Cuts could be defined by placing limits on the variables; a maximum of 20 cuts could be defined at any one time. Each histogram or scatter plot could have up to 10 cuts applied to it. The program would also

TABLE XI

TAPE FORMAT

Word	Contents
1	TDC reading
2	C212 word (see Table VII), bits 0-15
3-4	24 bits, discriminators on supertubes (DCRs)
5-8	8 ADC readings, two per word ADC 1,2: summed signal, 1 and 5 MeV/channel ADC 3-8: 6 side signals

calculate subtracted spectra for the neutral events, separated according to whether the biomed target was in or out.

As mentioned above, we took a mixture of events while running, in order to be able to check gains and subtractions on line. This was necessary but resulted in a large number of events on tape which were extraneous as far as calculating a branching ratio was concerned. The neutral events ($C \cdot C_L \cdot \bar{A}_L$) were only about 4% of the total. We decided, therefore, to edit the original tapes onto a smaller set of tapes. These edited tapes contained all the $C \cdot C_L \cdot \bar{A}_L$ events with energies above 15 MeV, and one in five of the $C \cdot C_L \cdot \bar{A}_S$ and muon decay events, for a total of about 5% of the original events. Scalers and clocks were written as sums over entire runs. We separated the edited tapes into run cycles (so each tape contained data from only one cycle); this gave us just 8 tapes to deal with instead of the original 61.

When replaying the edited tapes, it was possible to make histograms and scatter plots as before. The run sheet was also calculated, using the data on the entire tape. A subtracted spectrum was calculated, with the normalization of the "outside beam" spectrum being done run by run. Information needed to calculate a branching ratio was written to disk file for use by another program. This information included the following: a title; subtracted spectra, with errors; raw (unrenormalized) spectra; live beam; binning information; average renormalization factors. Except for the binning information, everything was divided according to the biomed target condition.

We made several cuts on the data before calculating a branching ratio. As has been mentioned frequently, the data were separated according to whether the biomedical target was in or out. Because of the background problems with that target, we used only data taken when it was out in our calculation of a branching ratio. This had the effect of cutting out about half our total data. Another cut we made was to require at least 3 of the 24 DCR channels to have fired. The purpose of this was to reduce contributions to the neutrals from tube noise. The threshold of the DCRs was set so that approximately half of them would fire for a typical muon-decay event. Scatter plots of DCRs vs energy for neutrals showed a tail of events with 0 or 1 DCR firing which extended above 50 MeV. No such tail was observed in the muon-decay events. Figure 38 shows contours from typical scatter plots. The effect of this DCR cut was checked on the muon decay events and found to be negligible above 20 MeV. It reduced the neutrals rate for the run illustrated in Fig. 38 from 475/LAday to 365/LAday. The last cut we made was on the live time. This was not known for each event, but could

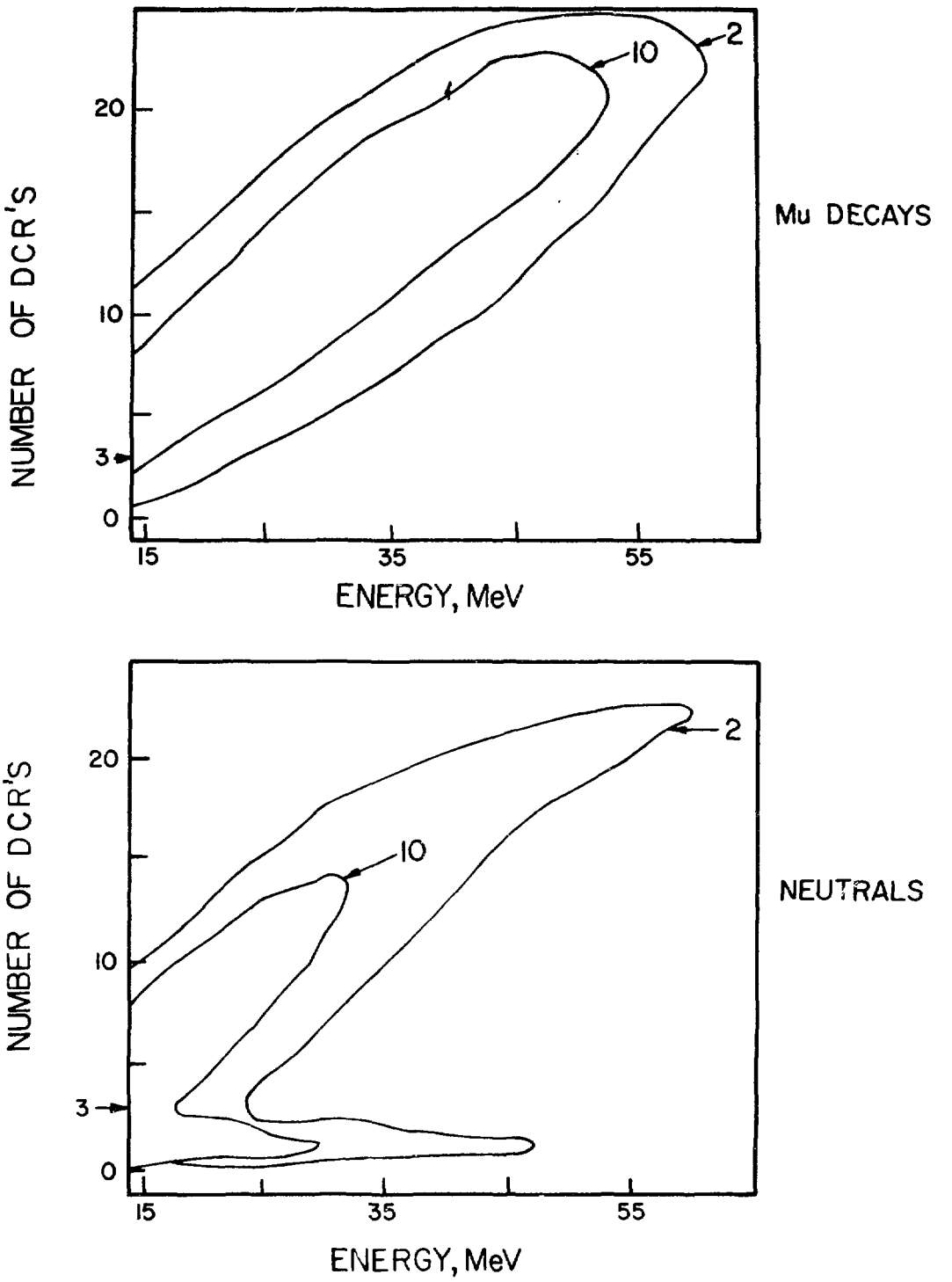

Fig. 38. Contour plots, DCRs vs energy for muon decays and neutrals.

be calculated for each 200-event record from the scalers and clocks. Normally, the live time was about 75%. The radioactive gas, described in the sections on the drift chambers and the neutrino house, reduced it on occasion to as low as 20%. We worried that our subtraction scheme might not work at that level, and decided to make a cut at 60%. Since we could only make this cut at the end of a record, it was made during the editing process. Records where the live time was less than the cutoff were simply ignored. This cut removed less than 10% of our data. There was a problem during Cycle 18 (November - December 1977) which was solved by making a cut on the data. The dead-time monitor subtraction was not zero for that cycle; it was (1.85 ± 0.27)%. This was investigated and found to be due to events coming between the beam gates. These events were called "beam in" because there was no "in" latch in the CAMAC gated coincidence register at that time; events were defined as being "in" if the "out" latch was not set. We added an "in" latch for subsequent running. A cut was made on the time of these events during the beam -- they appeared to be abnormally early, making such a cut unambiguous. With this cut, the subtraction was (-0.44 ± 0.30)%, consistent with zero.

The program which calculated the branching ratio had an expected spectrum per unit of beam, in bins which corresponded to one ADC channel each. The spectrum shape was that generated by the Monte Carlo program mentioned in the chapter on data acquisition, and was different for H_2O and D_2O, as shown in Fig. 39. This spectrum was then normalized to the actual amount of beam. The data, and the expected spectrum, were then added into bins several channels wide, to increase the statistics in each bin. Five channels per bin was a typical number, although it was

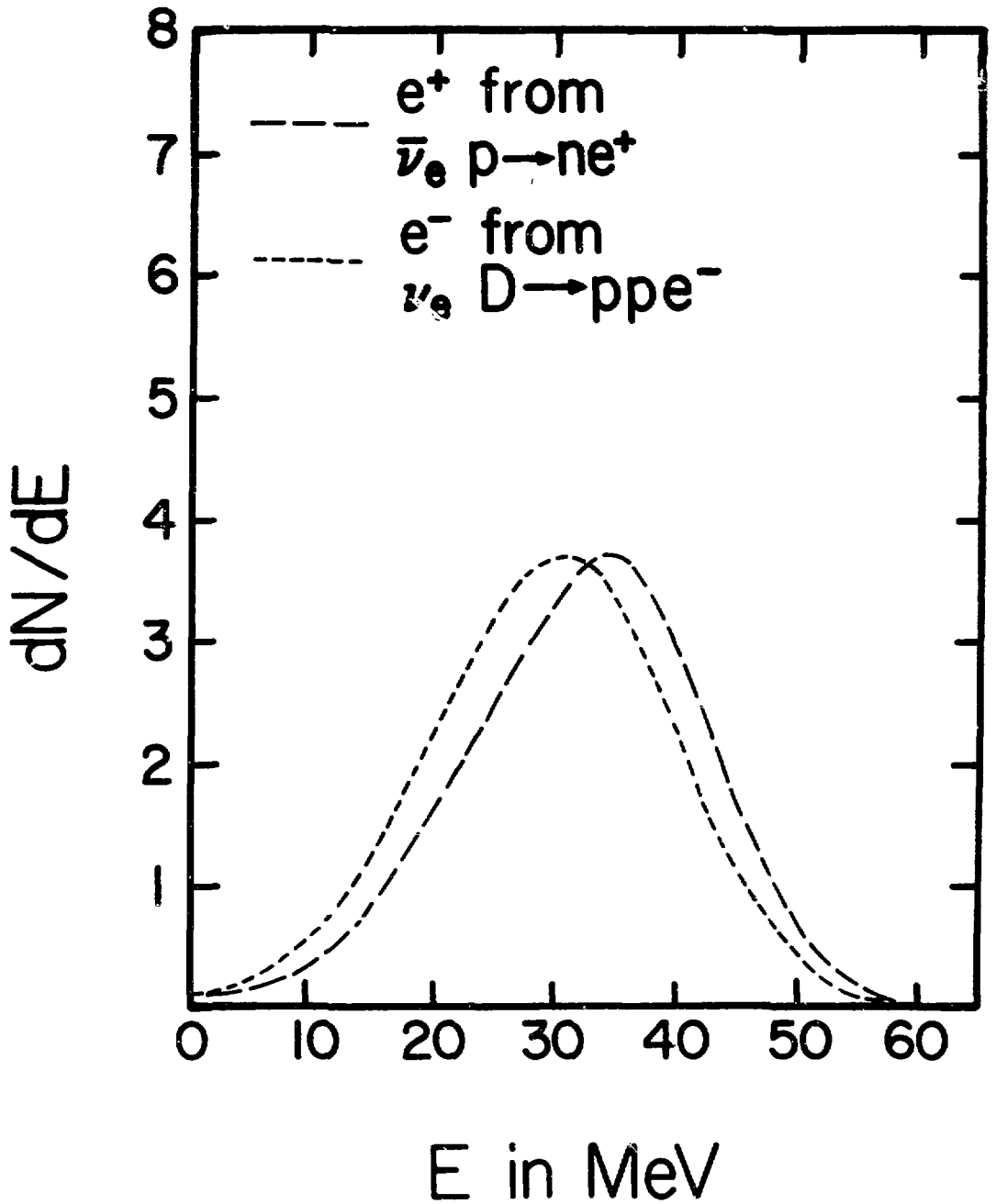

Fig. 39. Calculated spectra, e^+ from $\bar{\nu}_e p \rightarrow ne^+$, e^- from $\nu_e d \rightarrow ppe^-$.

possible to choose others. A ratio was then made, bin by bin, of the observed signal to the expected signal (S_i) with its error (σ_i). A weighted average was then performed over several bins, to find a value for the branching ratio:

$$R_{AV} = \frac{\Sigma(S_i/\sigma_i^2)}{\Sigma(1/\sigma_i^2)} \quad ,$$

with the error

$$\sigma_R = \frac{1}{\sqrt{\Sigma(1/\sigma_i^2)}} \quad .$$

The bins were selected to cover the range of substantial expected rate without getting into known low energy beam associated backgrounds. This was done for both the water and the heavy water data. The water number, R_H, was then the branching ratio for μ^+ decay to $\bar{\nu}_e$, normalized to the calculated flux. The heavy water number, R_D, was the ratio of the observed neutrino event rate to the calculated event rate. We then normalized R_H by R_D to cancel out any errors which may have been made in the calculation of flux or acceptance. Therefore,

$$R = \frac{R_H}{R_D} \quad ,$$

with the error on R calculated in quadrature from the errors on R_H and R_D.

The number of neutrino events per coulomb is given by the following expression:

$$\frac{N_\nu}{q_p}\frac{\ell^2}{4\pi d^2} n_p \sigma_\nu \ell \quad ,$$

where N_ν is the number of neutrinos per incident proton; q_p is the charge on the proton, in coulombs; ℓ is the length of a side of the detector; d is the average distance from the detector to the beam stop; n_p is the number of protons or deuterons per cubic centimeter in the detector (not counting the oxygen); and σ_ν is the neutrino interaction cross section on the proton or deuteron, as given in the theoretical section. N_ν has been measured by Chen et al.[66] to be 0.0571 ± 0.0035 at 720 MeV. A cascade calculation gave 0.078 at 700 MeV and 0.106 at 800 MeV; interpolating to 720 MeV yielded 0.083. The energy of protons arriving at the beam stop was 780 MeV with the Biomed target out and 732 MeV with the Biomed in. To find N_ν at these energies, we normalized to the Chen result and used the cascade calculation to give the slope. Substituting in the above equation, using ℓ^3 = 180 cm × 180 cm × 175 cm and d = 9.03 m, then gives the following results for the number of events per coulomb, assuming R = 1:

H_2O, bio out:	2.70
H_2O, bio in:	2.35
D_2O, bio out:	0.77
D_2O, bio in:	0.67

66. H. Chen et al., Nucl. Instrum. Meth. 160, 393 (1979).

CHAPTER 8

RESULTS AND CONCLUSIONS

A. HISTORY OF DATA TAKING

We begin with a history of the data taking, with dates, run numbers, average beam intensity, duty factor, water type, and live beam received. The live beam is computed after all cuts have been made, and is separated into biomed target out and target in. The data are divided into run cycles, determined by the operation of the accelerator. During a run cycle, the machine ran continuously except for short (12- to 24-hour) maintenance and development periods, and the average current and duty cycle remained fixed. Run cycles were separated by periods of one week to several months. The length of a cycle started at two weeks at the beginning of our running, and increased to two months by the end.

A subtracted spectrum was accumulated for an entire run cycle in the manner described in the chapter on analysis. Run cycles were combined as a weighted sum, to accomodate the different signal to noise conditions. All running was at 800-MeV beam energy.

Run Cycle 16: July 13, 1977 to August 4, 1977. Runs 573 to 594. 225 μA average, 6% duty factor. H_2O. 68.6 coulombs bio out, 48.7 coulombs bio in.

Run Cycle 17: August 14, 1977 to August 31, 1977. Runs 595 to 612.

225 μA average, 6% duty factor. H_2O. 78.8 coulombs bio out, 40.6 coulombs bio in.

Run Cycle 18: November 27, 1977 to December 20, 1977. Runs 654 to 711. 300 μA average, 7.5% duty factor. H_2O. 70.8 coulombs bio out, 44.4 coulombs bio in.

Run Cycle 19: February 4, 1978 to March 27, 1978. Runs 766 to 800. 300 μA average, 6% duty factor. H_2O. 220.7 coulombs bio out, 55.1 coulombs bio in. Biomed target broke February 22, during run 778. A target 1% of the thickness of the normal target was installed March 14, and used until the end of the cycle (runs 788 to 800). These data were combined with the target out data, as they did not show enhanced background levels at low energies. There were 62.1 coulombs of beam while this target was in.

Run Cycle 20: June 15, 1978 to July 23, 1978. Runs 821 to 857. 360 μA average, 7.5% duty factor. D_2O. 159.5 coulombs bio out, 102.1 coulombs bio in.

Run Cycle 21: August 4, 1978 to September 24, 1978. Runs 865 to 913. 360 μA average, 6% duty factor. D_2O. 240.0 coulombs bio out, 209.9 coulombs bio in.

Run Cycle 22: November 12, 1978 to January 2, 1979. Runs 935 to 977. 500 μA average, 7.5% duty factor. H_2O. 322.9 coulombs bio out, 183.7 coulombs bio in. Problems with targets, especially A2, at this beam intensity caused much down time, and forced some running at reduced intensity (as low as 270 μA average). The

data taken at intensities less than 400 μA average were not included.

Run Cycle 23: March 10, 1979 to May 7, 1979. Runs 992 to 1053. 450 μA average, 7.5% duty factor. H_2O. 447.1 coulombs bio out, 224.5 coulombs bio in. Problems with heat dissipation in biomed target forced two weeks of running at 360 μA average (March 28 to April 12, runs 1009 to 1022). These data were analyzed separately.

B. HEAVY-WATER RESULTS

The heavy-water running occurred during Cycles 20 and 21. The results will be described in terms of R_D = observed rate/calculated rate. Results are shown as a function of run cycle, bin size, and analysis region before known systematic backgrounds have been subtracted. These subtractions were small compared to the calculated neutrino signal for both light and heavy water, making this a valid procedure. Table XII shows the results cycle by cycle, using 5-MeV binning and analyzing from 25 to 55 MeV. The errors are purely

TABLE XII

D_2O RESULTS, CYCLE BY CYCLE

Run Cycle	R_D, Bio Out
20	1.75 ± 0.59
21	0.99 ± 0.43

statistical. No subtraction of beam-associated backgrounds has been made. The two cycles are consistent with each other, with a χ^2 of 1.1 for one degree of freedom.

Table XIII shows the value of R_D for the total D_2O running, for different bin sizes and analysis regions. It can be seen that the data are not sensitive to these variations. Other systematic effects are discussed below.

Figure 40 is the total subtracted D_2O spectrum for biomed target out, with the expected spectrum plotted on it.

TABLE XIII

D_2O RESULTS AS A FUNCTION OF BIN SIZE

AND ANALYSIS REGION

Bin Size	Limits	R_D, Bio Out
5	25-55	1.25 ± 0.34
5	20-55	1.31 ± 0.33
5	30-55	1.34 ± 0.38
5	25-60	1.25 ± 0.34
4	26-54	1.20 ± 0.35
4	30-54	1.22 ± 0.34
8	24-56	1.11 ± 0.34

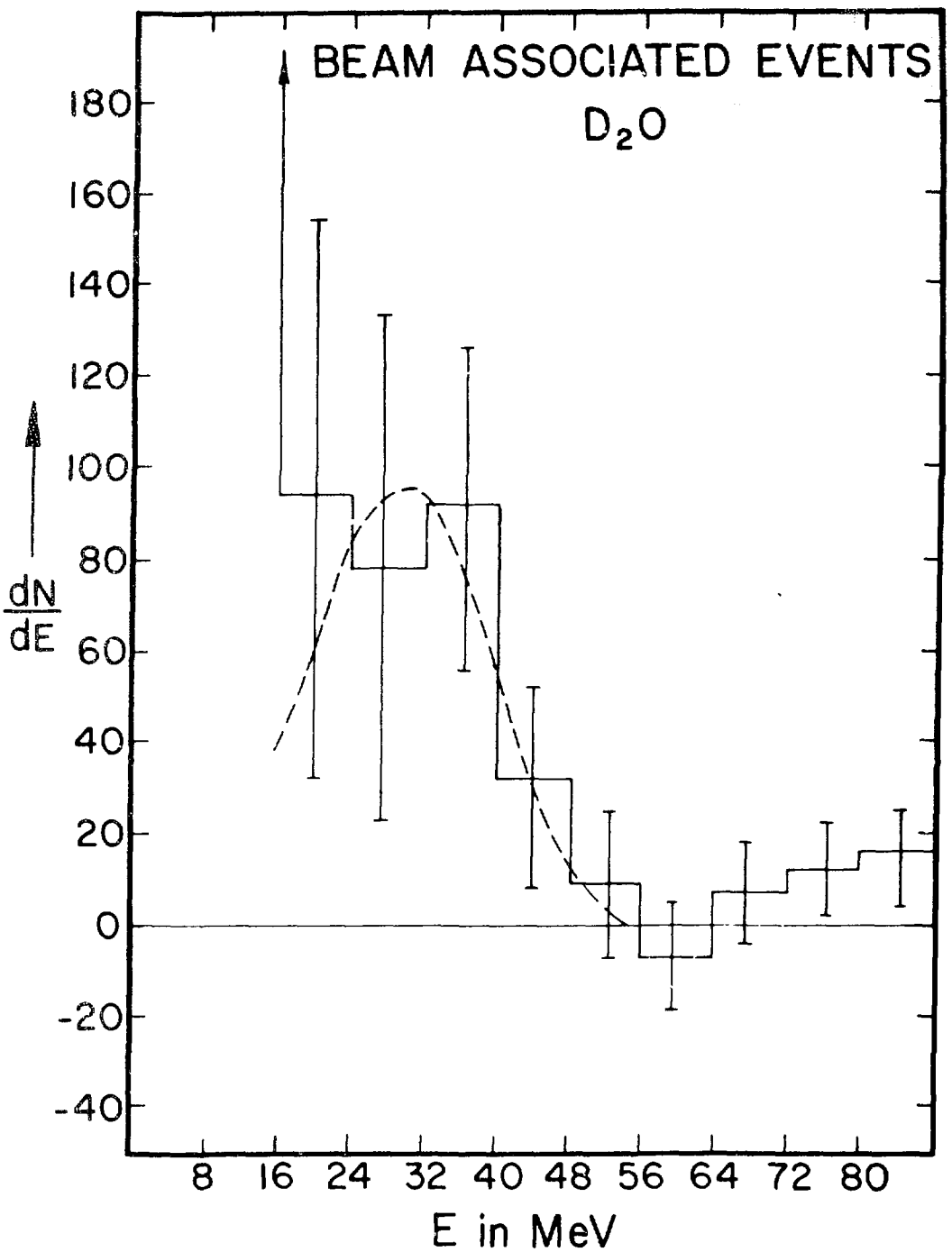

Fig. 40. D_2O subtracted spectrum with calculated spectrum.

C. WATER RESULTS

The water running occurred during Cycles 16-19 and 22-23. The results will be described in terms of R_H, defined as observed rate/calculated rate (for R = 1). Table XIV shows the data cycle by cycle, using 5-MeV binning and analyzing from 25 to 55 MeV. As in the D_2O data, the errors are purely statistical and no subtraction of beam-associated backgrounds has been made. The data from the separate run cycles are consistent with each other, with a χ^2 of 11.2 for six degrees of freedom.

TABLE XIV

H_2O RESULTS CYCLE BY CYCLE

Run Cycle	R_H, Bio Out
16	0.61 ± 0.22
17	0.27 ± 0.20
18	-0.26 ± 0.20
19	-0.01 ± 0.11
19 1% Biomed target	-0.17 ± 0.20
22	0.04 ± 0.09
23	0.01 ± 0.06

Table XV shows the value of R_H for the total H_2O running for different analysis regions and bin sizes. The data are not sensitive to these variations. Figure 41 shows the subtracted H_2O spectrum, biomed target out, and the expected spectrum for R = 1.

D. SYSTEMATIC EFFECTS

As discussed in the chapter on backgrounds, there were some known contributions to a beam-associated signal which did not come from neutrino interactions on protons or deuterons. Two of these will be subtracted, the residual neutron backgrounds and the contribution from neutrino-nucleus interactions. All results, unless otherwise stated, will be for 25 to 55 MeV and 5-MeV bins.

TABLE XV

H_2O RESULTS AS A FUNCTION OF BIN SIZE

AND ANALYSIS REGION

Bin Size	Limits	R_H, Bio Out
5	25-55	0.028 ± 0.043
5	20-55	0.045 ± 0.043
5	30-55	0.045 ± 0.045
5	25-60	0.028 ± 0.043
4	26-54	0.015 ± 0.043
4	22-54	0.027 ± 0.043
3	24-54	0.019 ± 0.043

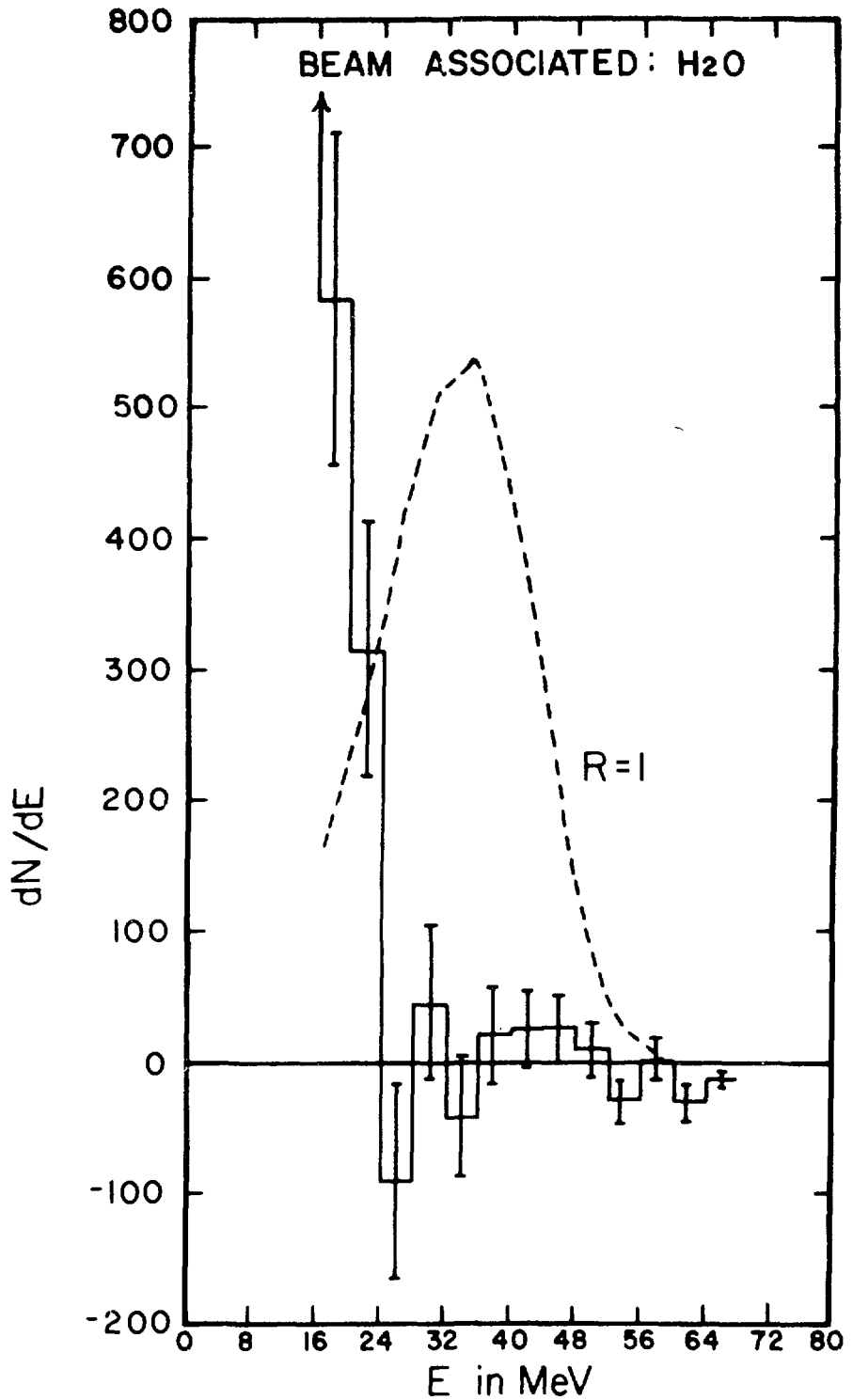

Fig. 41. H_2O subtracted spectrum with calculated spectrum.

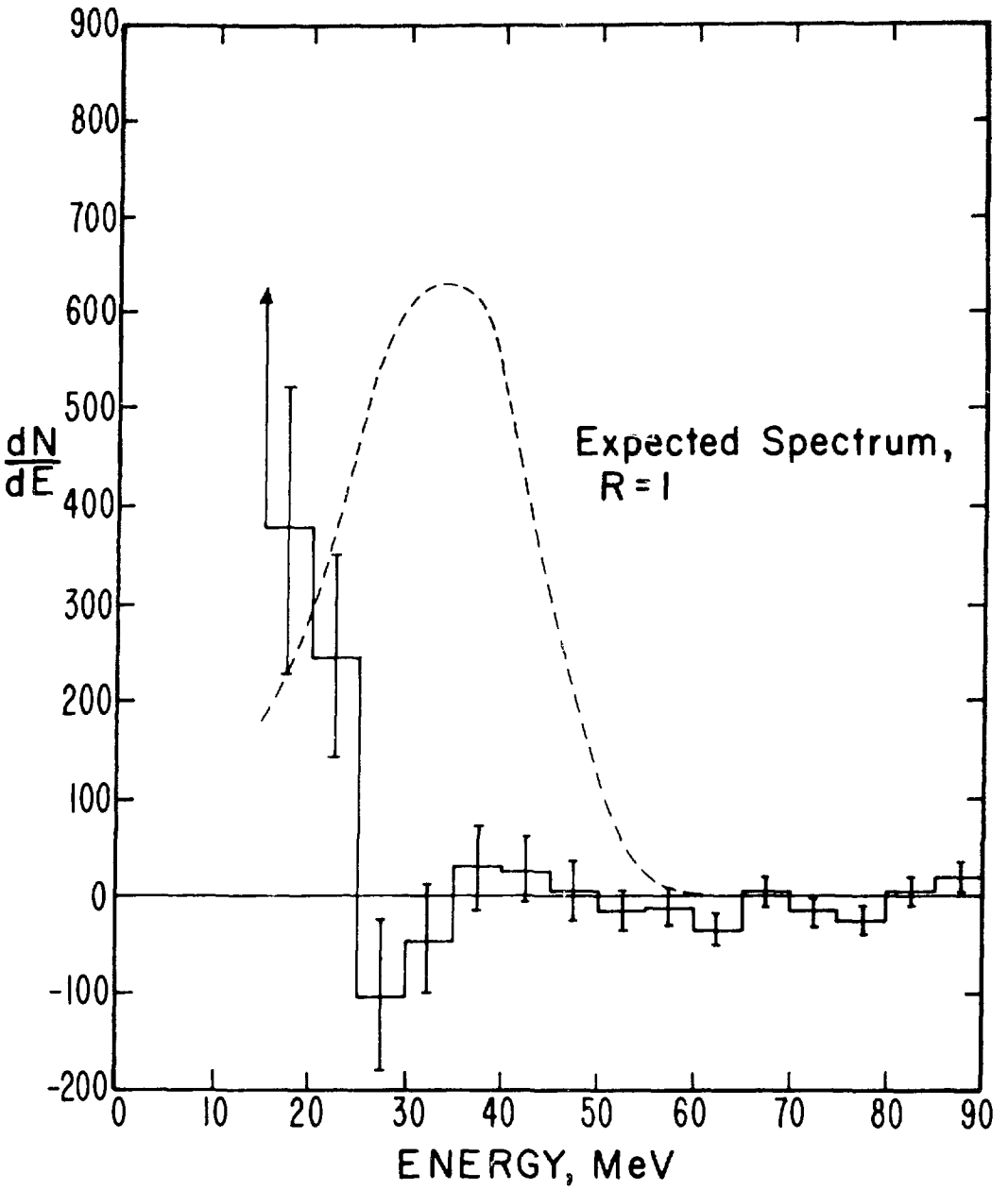

Fig. 42. H_2O spectrum with neutrino-nucleus and neutron backgrounds subtracted, with calculated spectrum.

The neutron background is shown in Figs. 28 and 29. The spectrum shape shown in Fig. 29 was normalized to the rate shown in Fig. 28, and then subtracted from both the water and the heavy water data. This gives

$$R_D = 1.11 \pm 0.34$$

$$R_H = 0.003 \pm 0.043 \quad .$$

The neutrino-nucleus cross sections are given in the theoretical section, and the relative amounts of ^{12}C, ^{16}O, and ^{27}Al are given in the section on backgrounds. The spectrum shapes are shown in Fig. 30. Subtracting those spectra with the appropriate weights gives

$$R_D = 1.09 \pm 0.34$$

$$R_H = -0.001 \pm 0.043 \quad .$$

Figure 42 shows the H_2O data after these subtractions have been made, with the calculated spectrum for R = 1. Figure 43 is the same for D_2O.

The effects of other possible systematic errors on R_D and R_H have also been investigated. These include a normalization error on the cosmic ray subtraction, an error in the energy scale, and a shift of the zero point in the spectrum. These checks have all been made on R_D and R_H before the above subtractions were done. A 0.2% error in the normalization, consistent with the overall DTM subtraction given with the calibrations and checks, increased R_D from 1.25 to 1.29, or 3%, and increased R_H from 0.028 to 0.036, or 29%. A change in the zero position of 1 channel, which is similar to a change in gain of 3%, changed R_D

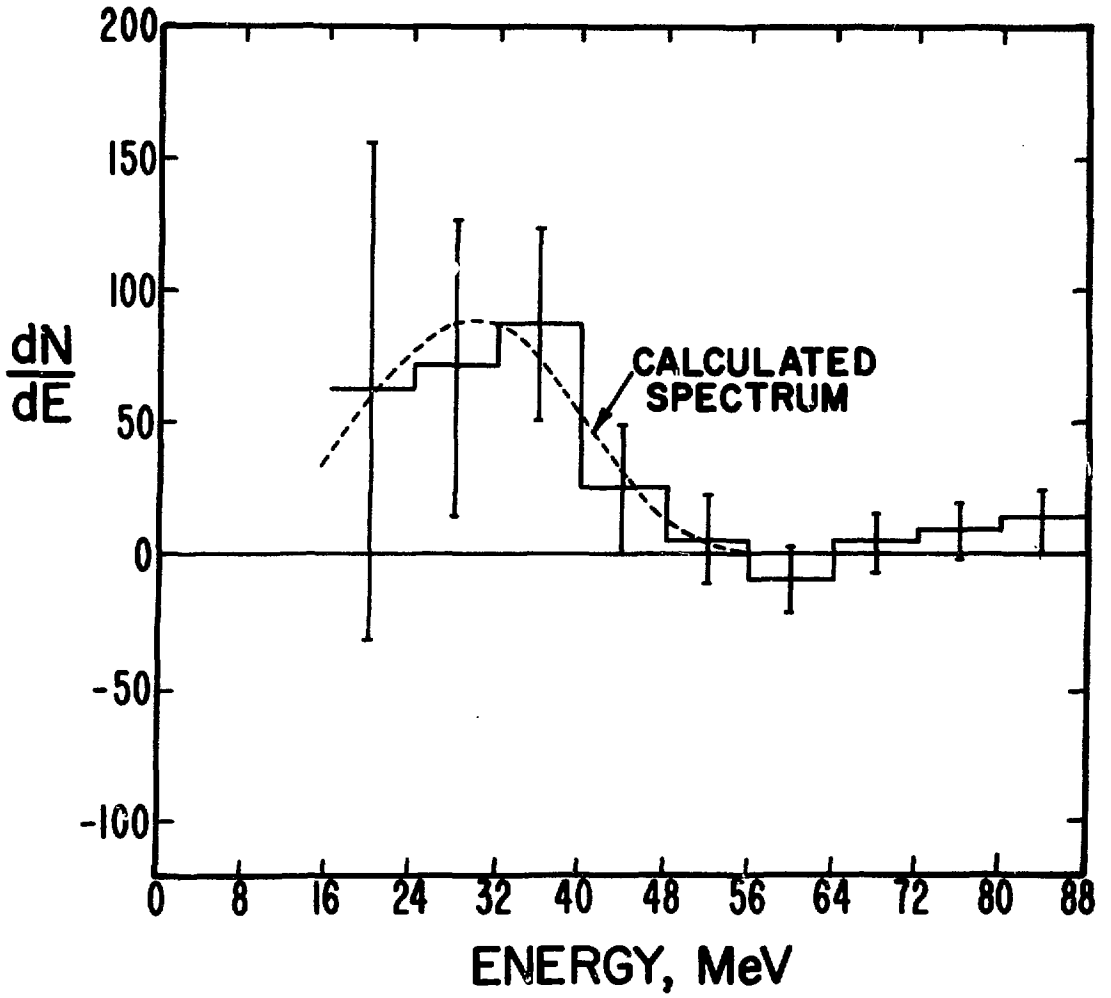

Fig. 43. D_2O spectrum with neutrino-nucleus and neutron backgrounds subtracted, with calculated spectrum.

from 1.25 to 1.29, or 3%, and increased R_H from 0.028 to 0.036, or 29%. A change in the zero position of 1 channel, which is similar to a change in gain of 3%, changed R_D from 1.25 to 1.31, or 5%, and changed R_H from 0.028 to 0.027, or 4%. We therefore increase the errors on R_D an R_H in quadrature by these amounts; the error on R_D increases to 0.35 and the error on R_H to 0.044. We now have

$$R_D = 1.09 \pm 0.35$$
$$R_H = -0.001 \pm 0.044$$

uncertainties in the flux normalization will cancel when R_H is renormalized by R_D. We would like to use R_D to determine a cross section for the reaction $\nu_e d \rightarrow ppe^-$, however, so for that purpose its error needs to be increased to include uncertainties in the flux. Assuming a 10% uncertainty in the flux gives

$$R_D = 1.09 \pm 0.37 \ .$$

The data taken when the biomedical target was in had a substantially increased neutron background; they may therefore be indicative of problems in the rest of the data. Analyzing these data in terms of R_D and R_H, without making any of the corrections described above, yields

$$R_D = 3.07 \pm 0.50$$
$$R_H = 0.235 \pm 0.089$$

for the region 25 to 55 MeV and 5-MeV bins. These numbers are consistent with the assumption that they contain the same neutron

consistent with the assumption that they contain the same neutron contribution, even though the apparent effect on the D_2O number is much larger, since the neutrino cross section on deuterium is smaller than an hydrogen. Subtracting R_D, bin by bin, as measured with bio out gives a neutron contribution to bio in of 1.99 ± 0.51. Analyzing this neutron spectrum in terms of R_d yields 0.42 ± 0.10, in good agreement with the observed value.

The following is a crude calculation of the $\bar{\nu}_e$ contribution to the subtracted spectrum from μ^- decay. We begin with the fraction of pions produced in various energy intervals by 740 MeV protons.[67] The energy scale is compressed by a factor of 2 to take into account energy loss in the isotope production stringers upstream of the beam stop. These fractions are in the second column of Table XVI, labeled F(T). The third column in this table is the fraction of pions which decay during the slowing-down time in copper, labeled f. The product of F(T) and f is shown in the fourth column, labeled ΔN. Summing this column gives the fraction of pions which decay. We assume here that π^- which do not decay while slowing down are captured, as the lifetime after capture is about 10^{-13} sec.[68] This sum is 0.0032; 0.32% of the π^- will decay. The fraction of μ^- which will decay instead of being captured is 0.074.[69] Multiplying this by 0.0032 gives 0.00024 as the fraction of π^- which will eventually give a μ^- decay. We divide this by 4 because the π^-/π^+ production ratio is 1/4,[70] giving a ratio of μ^- decays to μ^+ decays of 0.0001, or 1×10^{-4}.

---

67. D.R.F. Cochran et al., Phys. Rev. D 6, 3085 (1972).

68. R. Marshak, Meson Physics, McGraw-Hill, 1952, p. 170.

69. M. Eckhause et al., Nucl. Phys. 81, 575 (1966).

70. Cochran et al., Op. Cit.

Table XVI

T_π, MeV	F(T)	f	ΔN
0-10	0.10	0.0007	0.00007
10-50	0.42	0.0014	0.00059
50-100	0.28	0.0030	0.00084
100-200	0.20	0.0085	0.00170

This, then, is negligible compared to our level of sensitivity, and we therefore do not correct the subtracted number for it.

E. CONCLUSIONS

Using the number for R_D of 1.09 ± 0.37, we can derive a cross section for the reaction $\nu_e d \rightarrow ppe^-$. This is

$$\sigma(\nu_e d \rightarrow ppe^-) = (0.52 \pm 0.18) \times 10^{-40} cm^2 \quad .$$

This reaction is the inverse of the reaction $ppe^- \rightarrow d\nu_e$, which is a secondary source of energy in the sun, and is closely related to the reaction $pp \rightarrow de^+ \nu_e$, which is the primary source. Neither of these reactions has been seen in the laboratory.[71] Ours is the first measurement of the neutrino-deuteron reaction, and is in good agrement with the calculated value of $0.48 \rightarrow 10^{-40} cm^2$ given in the theoretical section.

71. J. S. O'Connell, op. cit.

Using the data from 25 to 55 MeV, we have

$$R_D = 1.09 \pm 0.35, \; R_H = -0.001 \pm 0.044 \; .$$

Renormalizing R_H by R_D as discussed above, we find

$$R = -0.001 \pm 0.040 \; .$$

Forming a 90% confidence level upper limit gives

$$R < 0.065 (90\% \text{ C.L.}) \; .$$

We therefore see no evidence for a multiplicative law. The theory of Derman discussed above is not ruled out; the data may be used to put a lower limit of the mass of the $\pi = -1$ Higgs boson of

$$M_H > 3.5 \text{ GeV}$$

(using $m_\tau = 1782 \text{ MeV}/c^2$)[72] .

In order to place an upper limit on neutrino oscillations, it is necessary to integrate the expression for W_{ν_ℓ, ν_ℓ}, found in the theoretical section over the finite detector size and the neutrino energy spectrum. This cannot be done analytically, so it was done with a Monte Carlo. The results of the Monte Carlo are shown in Fig. 44.

72. W. Bacino et al., SLAC Report No. SLAC-PUB-2113 (1978).

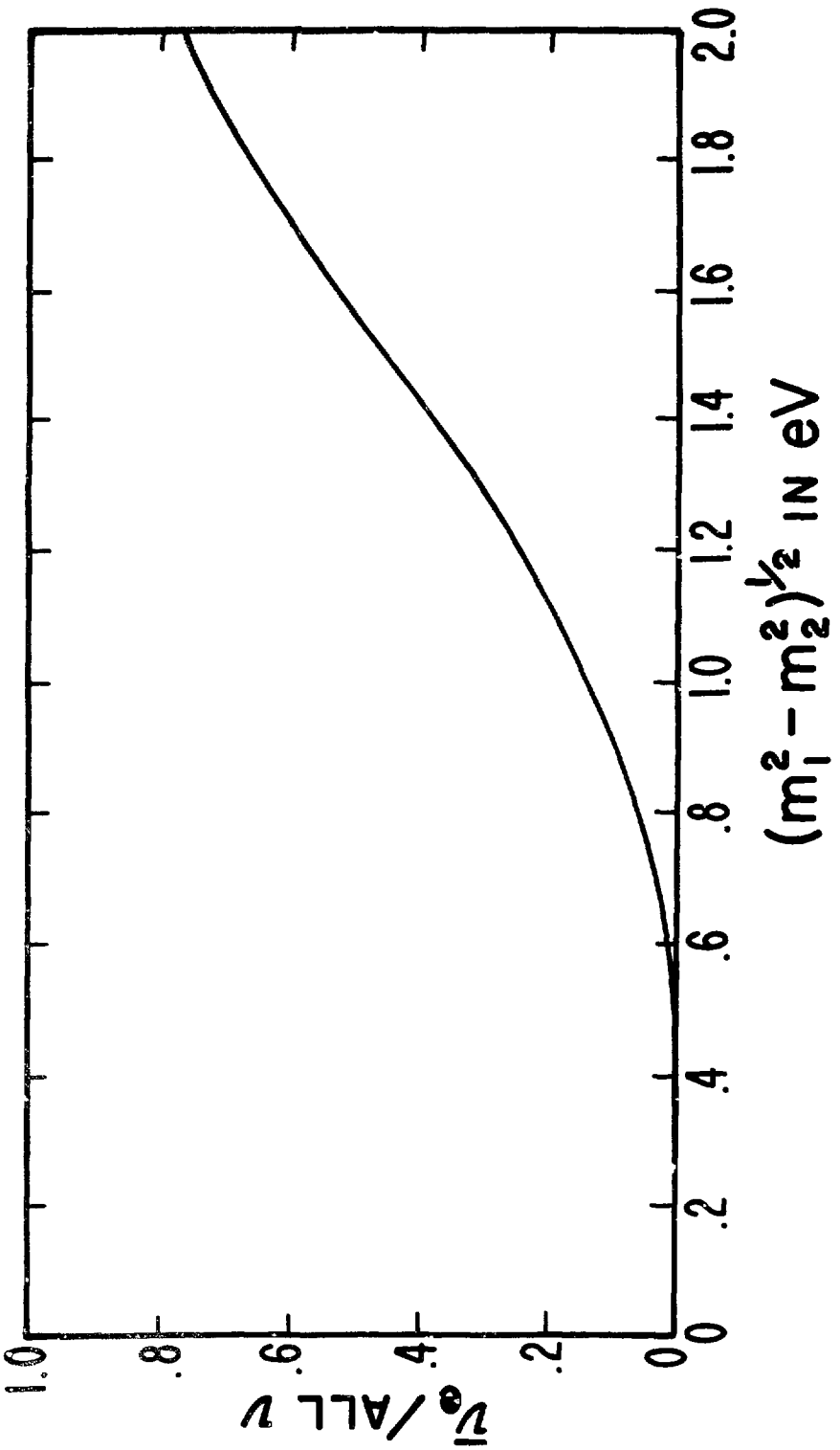

Fig. 44. Probability of observing $\bar{\nu}_e$ as a function of M_1.

Assuming $m_2=0$, the present result of $R \leq 0.065$ corresponds to a limit on the neutrino mass of

$$m_1 \leq 0.8 \text{ eV}.$$

Present upper limits on this come from the Gargamelle collaboration; they report a limit of $m_1 \lesssim 1\text{eV}$.[73]

---

73. E. Bellotti et al., Nuov. Cim. Lett. 17, 553 (1976).

ACKNOWLEDGEMENTS

An experiment of this length and complexity necessarily involved the contributions of many people.

I would like to thank my collaborators; they were Drs. R. L. Burman, D. R. F. Cochran, J. Duclos, J. Frank, C. K. Hargrove, V. W. Hughes, H. Kaspar, U. Moser, P. Nemethy, and R. P. Redwine. I am particularly indebted to Peter Nemethy, the spokesman for the experiment, whose help, guidance, and patience were essential.

Special thanks go to the LAMPF accelerator operators, and their Chief, Dr. D. C. Hagerman, who provided us with two years of beamtime. Also, the support of the LAMPF administration, particularly Dr. Louis Rosen, was invaluable.

The staffs of both LAMPF and Yale provided valuable technical support for this experiment. I am particularly grateful to the people at the LAMPF Area-A Manager's Office for their help.

My thesis advisor for this experiment was Dr. Vernon W. Hughes.